FINAL REPORT

KU-BAND SYSTEM DESIGN STUDY AND TDRSS INTERFACE ANALYSIS

(EXHIBIT C)

(NASA-CR-171701) Ku-BAND SYSTEM DESIGN STUDY AND TDRSS INTERFACE ANALYSIS Final Report (LinCom Corp., Los Angeles, Calif.) 185 p HC A09/MF A01 CSCL 17B
N83-35202
Unclas
G3/32 42180

PREPARED FOR

NATIONAL AERONAUTICS AND SPACE ADMINISTRATION
LYNDON B. JOHNSON SPACE CENTER
HOUSTON, TX 77058

TECHNICAL MONITOR: WILLIAM TEASDALE

CONTRACT NO. NAS9-16097

LinCom Corporation

P.O BOX 15897, LOS ANGELES, CALIFORNIA 90015

FINAL REPORT

KU-BAND SYSTEM DESIGN STUDY AND TDRSS INTERFACE ANALYSIS

(EXHIBIT C)

PREPARED FOR

NATIONAL AERONAUTICS AND SPACE ADMINISTRATION
LYNDON B. JOHNSON SPACE CENTER
HOUSTON, TX 77058

TECHNICAL MONITOR: WILLIAM TEASDALE

CONTRACT NO. NAS9-16097

PREPARED BY

W. C. LINDSEY
T. M. MCKENZIE
H. J. CHOI
C. S. TSANG
S. H. AN

LINCOM CORPORATION
P.O. BOX 15897
LOS ANGELES, CA 90015-0897

AUGUST 1, 1983

TABLE OF CONTENTS

TABLE OF CONTENTS (continued)

LIST OF FIGURES

Page

Section 1

Section 2

Section 2.3

Section 2.4

LIST OF FIGURES (continued)

Page

Section 2.4 (continued)

Section 2.6

Section 3.1

Section 3.3

LIST OF FIGURES (continued)

Page

Section 4.2

Section 4.3

Section 5

LIST OF FIGURES (continued)

Section 6.2

LIST OF TABLES

Page

Section 2.4

Section 2.5

Section 2.6

Section 3.2

Section 3.3

Section 4.3

Section 5.

0. SUMMARY

0.1. INTRODUCTION

This document represents the final report for the Ku-Band System Design Study and TDRSS Interface Analysis performed under Contract NAS9-16097 (Exhibit C) and directed by William Teasdale. It represents a portion of the work accomplished during the reporting period April 14, 1980, through March 19, 1983.

The objectives of this contract were to expand the capabilities of the Shuttle/TDRSS link simulation program (LinCsim) to account for radio frequency interference (RFI) effects on the Shuttle S-band links, to update the channel models to reflect the RFI related hardware changes, to review and evaluate the ESTL hardware modeling of the TDRS communication payload, to model in LinCsim the Shuttle/TDRSS signal acquisition, to upgrade LinCsim, and to evaluate possible Shuttle on-orbit navigation techniques.

In this chapter of the report an overall description of the accomplishments is given. The remaining chapters and the attachments provide a more detailed description of the analysis and modeling performed under this contract during the period June 1, 1981, through March 19, 1983.

0.2. SUMMARY OF WORK ACCOMPLISHED

This report documents the analysis and modeling performed by LinCom under the six tasks contained in the Statement of Work. The effort for the period April 14, 1980, through May 31, 1981, was fully documented in [1], so the remainder of this report deals only with the work for the period June 1, 1981, through March 19, 1983.

Task 1: Refinement of Shuttle/TDRSS Link Simulation Models

This task required the refinement of the Shuttle/TDRSS S-band and Ku-band link simulation models for specific Shuttle signal designs and revised Shuttle and TDRS parameters. The simulation capability refined and upgraded under this task allows the prediction of communications link margins, the analysis of performance sensitivity to various link parameters, user constraints, and the study of performance tradeoffs between different hardware implementations.

The major accomplishments under this task are fully described in Chapter 1 of this report. Briefly, they were as follows:

(1) Update of the Shuttle and TDRSS link power budget values used in LinCsim to reflect the latest available information from the hardware vendors.

(2) Analysis and performance predictions for the digital data transition tracking loop in the Shuttle S-band Demodulator/Bit Synchronizer. Two implementations of the loop were treated.

Task 2: S-band and Ku-band Communication Link Performance Analysis

The performance of the Shuttle/TDRSS S-band and Ku-band communications uplink and downlink channels was evaluated using the latest Shuttle Ku-band and TDRSS parameters available from the hardware vendors and the upgraded simulation models. Link budgets and critical parameter effects were determined.

The major accomplishments under this task are fully described in Chapter 2 of this report and Attachments 1 and 2. Briefly, they were as follows:

(1) The Shuttle's contribution to the phase noise performance of the TDRSS Ku-band autotrack system was assessed.

(2) The false-lock problem at high SNR in the Shuttle/TDRSS S-band PN-code tracking loop was analyzed and solutions were proposed.

(3) The CNR degradation to bit error rate due to RFI on the Shuttle/TDRSS S-band return link was predicted.

(4) The RFI effect on the acquisition performance of the Shuttle S-band Demodulator/Bit Synchronizer was analyzed and predictions of its impact were made.

(5) The false-lock problem of the Shuttle's Payload Signal Processor was assessed and solutions proposed.

(6) Possibilities were raised for the mitigation of the RFI effect on the Shuttle/TDRSS links.

Task 3: Evaluation of ESTL Simulator and TDRSS Flight Hardware Characteristics

Under this task the basic differences between ESTL simulation hardware and TDRSS system design were assessed and NASA was provided with a summary report identifying the basic differences and recommending the required ESTL TDRSS simulator modifications to provide greater fidelity. The recommended TDRSS simulator modifications are designed to model the TDRS hardware changes implemented to combat RFI effects. The ESTL test channel conditions and repeater parameter settings were reviewed for fidelity to TDRSS operational modes and performance predictions were provided for ESTL communication system tests.

The major accomplishments under this task are discussed in Chapter 3 and Attachment 3 of this report. Briefly, they were as follows:

(1) A method was given by which RFI environments may be approximated by ESTL's RFI Test Generator.

(2) Several sets of predictions of the RFI degradation to bit error rate for the ESTL tests were made.

(3) An attempt was made to explain the discrepancy between prediction and observation of the RFI degradation.

Task 4: TDRSS RFI Model and Simulation

Under this task the analytical link models were modified to describe the effects of the TDRSS RFI environment on Shuttle communications links based on RFI models provided by Goddard Space Flight Center. The LinCsim analytical simulation package was modified to include the updated RFI models.

The major accomplishments under this task are fully documented in Chapter 4. Briefly, they were as follows:

(1) The analytical simulation model of the effect of RFI on bit error rate was considerably refined.

(2) A Monte Carlo-type simulation that modeled the effect of RFI on bit error rate has been developed.

(3) An analytical simulation model of the effect of RFI on the performance of the synchronization systems and Doppler tracking system was developed.

Task 5: Shuttle/TDRSS Acquisition

Analytical models for the processes of PN/carrier/clock acquisition were derived. An analytical simulation package was produced capable of predicting the acquisition time distribution for individual subsystems as well as for the complete system. These simulation models include the effects of RFI on acquisition.

The major accomplishment under this task is described fully in Chapter 5 of this report. Briefly, it is as follows:

(1) An analytical simulation package that is capable of predicting the acquisition performance of the entire Shuttle/TDRSS link (including Ku-band autotrack) was developed. It models both forward and return links. The RFI effect modeling is mostly complete.

Task 6: LinCsim Upgrading and Maintenance

The LinCsim analytical simulation model was refined as the hardware evolved subject to RFI model updates and the sensitivity analysis and user constraint parameter modeling was extended to new parameters on request by JSC. Performance and user constraint parameter sensitivity data were generated by LinCsim for various parameters and channel conditions selected by JSC as the Ku-band and S-band system implementation evolved.

The major accomplishments under this task are fully documented in Chapter 6 of this report. Briefly, they were as follows:

(1) The effect on bit error rate of the user constraint parameter spurious phase modulation was modeled in LinCsim.

(2) The effect on bit error rate of the user constraint parameter incidental amplitude modulation was modeled in LinCsim.

Reference

1. W.R. Braun, W.C. Lindsey, T.M. McKenzie, T. Tai, and C. Wang, "Final Report, Ku-Band System Design Study and TDRSS Interface Analysis," Contract No. NAS 9-16097, Exhibit C,LinCom Corp., Los Angeles, CA, June 1, 1981.

1. REFINEMENT OF SHUTTLE/TDRSS LINK SIMULATION MODELS

1.1 INTRODUCTION

This chapter documents the work accomplished under Task #1, which calls for the refinement of the Shuttle/TDRSS link simulation models. Section 1.1 describes the update of the Shuttle and TDRSS link power budget values used in LinCsim. Section 1.2 presents analysis and performance predictions for the digital data transition tracking loop in the S-band Shuttle Demodulator/Bit Synchronizer. Analysis is presented for two possible implementations of the loop since it is not clear which is actually used, and performance predictions are made for the more likely candidate.

1.2 UPDATE OF THE SHUTTLE AND TDRSS LINK POWER BUDGET VALUES

The Shuttle and TDRSS link power budget values have been updated to those values given in "Tracking and Data Relay Satellite System Telecommunication Performance and Interface Document SE-09 (TPID)," TRW DSSG, Redondo Beach, CA, 12 September 1981, and "Space Shuttle Communications and Tracking RF Link Circuit Margin Data Book," EE8-6/81-069, by S. W. Novosad and Y. S. Kuo, Tracking and Communications Development Division, NASA/JSC, Houston, Texas, August 1981. The values are part of the data base stored in LinCsim which supplies default values for program execution.

1.3 PERFORMANCE OF SYMBOL SYNCHRONIZER IN S-BAND SHUTTLE DEMODULATOR/BIT SYNCHRONIZER

1. INTRODUCTION

The digital data-transition tracking loop for biphase symbols implemented in the S-Band Shuttle Demodulator/Bit Synchronizer (SSDBS) [1] is analyzed in detail below. The loop S-curve and the equivalent noise spectral density required for performance analysis are derived. Typical performance parameters, clock jitter and symbol slip rate, are provided for evaluation purposes.

2. SYSTEM MODEL

The SSDBS symbol synchronizer is modeled in Fig. 1 [1]. The integrator I_1 is used to estimate the symbol polarity over each symbol interval T. The input to I_1 is multiplied by the Manchester pulse and is thus matched to input signal modulation. Integrator I_2 integrates across the midsymbol transition and integrator I_3 integrates the transitions between adjacent symbols. The output signals, properly delayed, are combined to form an error signal e_k. We are not sure of the signs with which the outputs of I_2 and I_3 are combined. We first analyze the case where the signs are as shown in Fig. 1, which we believe is preferable, and then the case where both signs are positive.

The equivalent phase-locked loop model for the symbol synchronizer is given in Fig. 2. The main task is to find the loop cross-correlation function (loop S-curve) $g(\lambda)$ and the equivalent noise $n_\lambda(t)$ power spectral density $S(\omega,\lambda)$. During the steady state operation of the symbol sync, $S(\omega,\lambda)$ is closely approximated with $S(0,0)$. Assuming a first order loop, $F(s) = K_p$, the probability density function of the normalized timing error λ is given by [2]

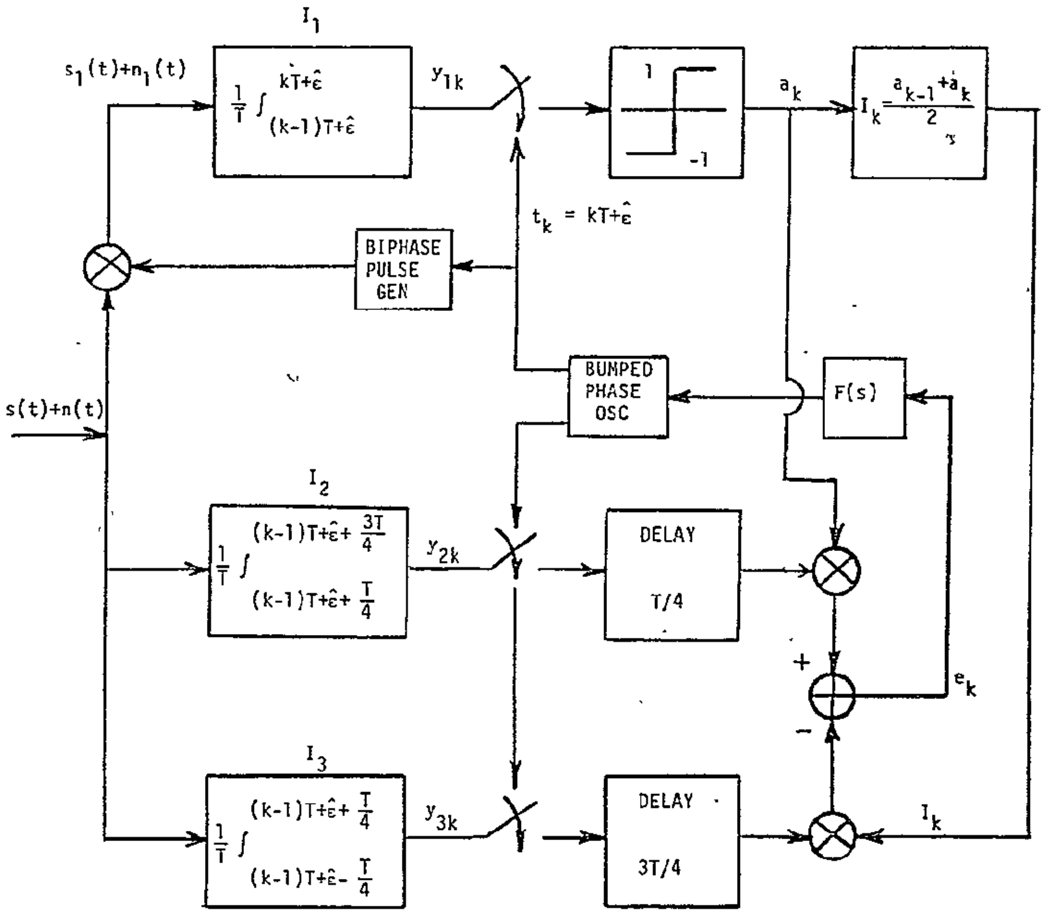

Figure 1. DTTL Model for Biphase Signal.

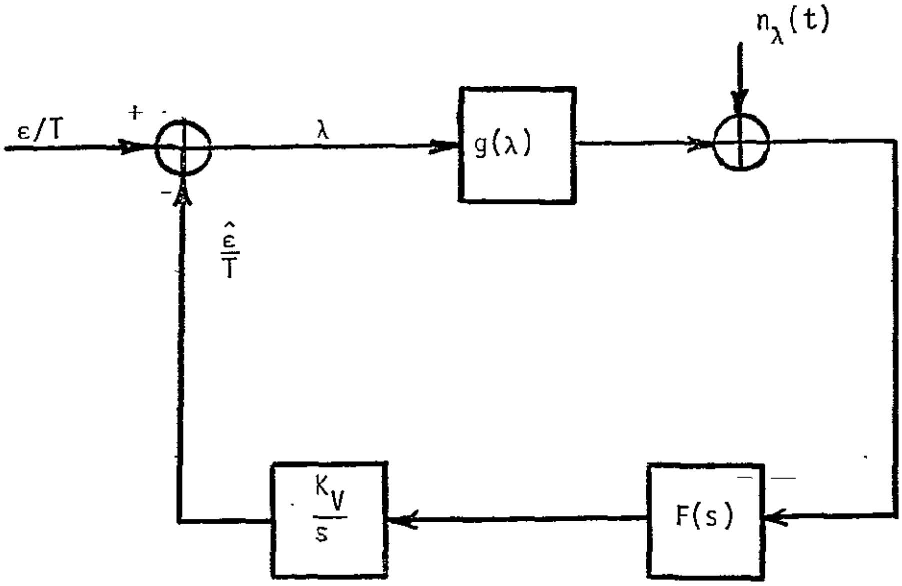

Figure 2. Equivalent Phase-Locked Loop Model.

$$p(\lambda) = C \exp\left[\frac{-2}{KS(0,0)} \int_0^\lambda g(x)dx\right] \quad (1)$$

where C is a normalization constant and $K = K_V K_p$.

3. LOOP S-CURVE

The loop S-curve $g(\lambda)$ is defined to be

$$g(\lambda) \overset{\Delta}{=} E_{n,s}[e_k | \lambda] \quad (2)$$

where the expectation is averaged over both additive noise and signal pattern. Decompose the integrator I_1 output y_{1k} into the signal c_k and noise ν_k components.

$$y_{1k} = c_k + \nu_k \quad (3)$$

where

$$c_k = \frac{1}{T} \int_{(k-1)T}^{kT} s_1(t)dt \quad (4)$$

$$\nu_k = \frac{1}{T} \int_{(k-1)T}^{kT} n_1(t)dt \quad (5)$$

$$s_1(t) = s(t)p(t-(k-1)T) \quad (6)$$

$$n_1(t) = n(t)p(t-(k-1)T) \quad (7)$$

$$p(t) = \begin{cases} 1 ; & 0 < t < T/2 \\ -1 ; & T/2 < t < T \\ 0 ; & \text{otherwise} \end{cases} \quad (8)$$

$$s(t) = \sum_k d_k q(t-kT-\varepsilon) \tag{9}$$

$$q(t) = \begin{cases} A ; & 0 < t < T \\ 0 ; & \text{otherwise} \end{cases} \tag{10}$$

The data $d_k = \pm 1$ is assumed to be equally probable. ε is the random timing epoch. Similarly the integrator outputs y_{2k} and y_{3k} are decomposed to

$$y_{2k} = b_{1k} + \mu_{1k} \tag{11}$$

where

$$b_{1k} = \frac{1}{T} \int_{(k-1)T+\frac{T}{4}}^{(k-1)T+\frac{3T}{4}} s(t)dt \tag{12}$$

$$\mu_{1k} = \frac{1}{T} \int_{(k-1)T+\frac{T}{4}}^{(k-1)T+\frac{3T}{4}} n(t)dt \tag{13}$$

and

$$y_{3k} = b_{2k} + \mu_{2k} \tag{14}$$

$$b_{2k} = \frac{1}{T} \int_{(k-1)T-\frac{T}{4}}^{(k-1)T+\frac{T}{4}} s(t)dt \tag{15}$$

$$\mu_{2k} = \frac{1}{T} \int_{(k-1)T-\frac{T}{4}}^{(k-1)T+\frac{T}{4}} n(t)dt \tag{16}$$

The timing estimate $\hat{\varepsilon}$ is arbitrarily set to be zero. For convenience, the following quantities are defined

$$M_{1k} = \frac{1}{T}\int_{(k-1)T}^{(k-1)T+\frac{T}{4}} n_1(t)dt, \qquad N_{1k} = \frac{1}{T}\int_{(k-1)T}^{(k-1)T+\frac{T}{4}} n(t)dt$$

$$M_{2k} = \frac{1}{T}\int_{(k-1)T+\frac{T}{4}}^{(k-1)T+\frac{3T}{4}} n_1(t)dt, \qquad N_{2k} = \frac{1}{T}\int_{(k-1)T+\frac{T}{4}}^{(k-1)T+\frac{3T}{4}} n(t)dt$$

$$M_{3k} = \frac{1}{T}\int_{(k-1)T+\frac{3T}{4}}^{kT} n_1(t)dt, \qquad N_{3k} = \frac{1}{T}\int_{(k-1)T+\frac{3T}{4}}^{kT} n(t)dt \tag{17}$$

$$N_{4k} = \frac{1}{T}\int_{(k-1)T+\frac{T}{4}}^{(k-1)T+\frac{T}{2}} n(t)dt, \qquad N_{5K} = \frac{1}{T}\int_{(k-1)T+\frac{T}{2}}^{(k-1)T+\frac{3T}{4}} n(t)dt$$

The additive noise n(t) is assumed to be zero-mean white Gaussian noise with two-sided power spectral density $N_0/2$ watt/Hz. The variances of the quantities in (17) are given by

$$\sigma^2_{M_{1k}} = \sigma^2_{N_{1k}} = \sigma^2_{M_{3k}} = \sigma^2_{N_{3k}} = \sigma^2_{N_{4k}} = \sigma^2_{N_{5k}} = \frac{N_0}{8T} \triangleq \sigma^2$$

$$\sigma^2_{M_{2k}} = \sigma^2_{N_{2k}} = 2\sigma^2 \tag{18}$$

If the symbol time-loop bandwidth product is small, i.e., $W_LT \ll 1$, the time delays in y_{2k} and y_{3k} signal paths can be neglected in analysis.

Therefore,

$$e_k = y_{2k}a_k - y_{3k}I_k \tag{19}$$

We first average e_k over the noise for a fixed λ.

$$\begin{aligned}
&E_n[e_k|\lambda] \\
&\quad = E_n[b_{1k}\ \mathrm{sgn}(c_k+M_{1k}+M_{2k}+M_{3k}) + N_{2k}\ \mathrm{sgn}(c_k+M_{1k}+M_{2k}+M_{3k})|\lambda] \\
&\qquad - \frac{1}{2} b_{2k}E_n[\mathrm{sgn}(c_{k-1}+M_{1(k-1)}+M_{2(k-1)}+M_{3(k-1)})+\mathrm{sgn}(c_k+M_{1k}+M_{2k}+M_{3k})|\lambda] \\
&\qquad - \frac{1}{2} E_n[N_{3(k-1)}\mathrm{sgn}(c_{k-1}+M_{1(k-1)}+M_{2(k-1)}+M_{3(k-1)}) \\
&\qquad\qquad\qquad + N_{3(k-1)}\mathrm{sgn}(c_k+M_{1k}+M_{2k}+M_{3k})|\lambda] \\
&\qquad - \frac{1}{2} E_n[N_{1k}\ \mathrm{sgn}(c_{k-1}+M_{1(k-1)}+M_{2(k-1)}+M_{3(k-1)}) \\
&\qquad\qquad\qquad + N_{1k}\ \mathrm{sgn}(c_k+M_{1k}+M_{2k}+M_{3k})|\lambda]
\end{aligned} \tag{20}$$

Evaluating term by term, (18) is simplified to

$$\begin{aligned}
&E_n[e_k|\lambda]\frac{1}{\sigma\sqrt{8}} \\
&\quad = \sqrt{R_s}\{b_{n1k}\ \mathrm{erf}[\sqrt{R_s}\ c_{nk}] - \frac{1}{2} b_{n2k}[\mathrm{erf}(\sqrt{R_s}\ c_{n(k-1)})+\mathrm{erf}(\sqrt{R_s}c_{nk})]\} \\
&\qquad + \frac{1}{8\sqrt{\pi}}\{\exp[-R_s c^2_{n(k-1)}] - \exp[-R_s c^2_{nk}]\}
\end{aligned} \tag{21}$$

where

$$R_s = \frac{A^2T}{N_0} = \frac{E_b}{N_0} \tag{22}$$

$$b_{n1k} = b_{1k}/A$$

$$= \begin{cases} 2\lambda d_k & 0 < \lambda < \frac{1}{4} \\ \frac{1}{4}\,(d_{k-1}+3d_k)-\lambda(d_{k-1}+d_k)\ ; & \frac{1}{4} < \lambda < \frac{1}{2} \end{cases} \tag{23}$$

$$b_{n2k} = b_{2k}/A$$

$$= \begin{cases} \frac{1}{4}\,(d_k-d_{k-1})-\lambda(d_k+d_{k-1})\ ; & 0 < \lambda < \frac{1}{4} \\ d_{k-1}(2\lambda-1)\ ; & \frac{1}{4} < \lambda < \frac{1}{2} \end{cases} \tag{24}$$

$$c_{nk} = c_k/A$$

$$= d_k-\lambda(d_{k-1}+3d_k)\ ; \qquad 0 < \lambda < \frac{1}{2} \tag{25}$$

Averaging over the signal pattern, $g(\lambda)$ is given by

$$g(\lambda) = E_{s,n}[e_k|\lambda]$$

$$= \begin{cases} \frac{A}{8}[(10\lambda-\frac{1}{2})\mathrm{erf}(\sqrt{R_s}(1-2\lambda))+(14\lambda+\frac{1}{2})\mathrm{erf}(\sqrt{R_s}\ (1-4\lambda))]; & 0<\lambda<\frac{1}{4} \\ \frac{A}{4}\{\mathrm{erf}[\sqrt{R_s}(1-2\lambda)]+4(1-2\lambda)\mathrm{erf}[\sqrt{R_s}(1-4\lambda)]\} & ;\ \frac{1}{4}<\lambda<\frac{1}{2} \end{cases} \tag{26}$$

We note that $g(\lambda)$ has period 1. The normalized loop S-curve is defined by

$$g_n(\lambda) = \frac{g(\lambda)}{g'(0)\big|_{R_s\to\infty}} = \frac{g(\lambda)}{3A} \tag{27}$$

Its slope at $\lambda=0$ is given by

$$g_n'(0) = \mathrm{erf}(\sqrt{R_s}) - \frac{1}{12}\sqrt{R_s/\pi}\ e^{-R_s} \tag{28}$$

We now analyze the case where the outputs of the I_2 and I_3 integrators are combined with positive signs, as the loop is drawn in [1]. The S-curve is then given by

$$G(\lambda) = \begin{cases} \frac{A}{8}\left[(6\lambda+\frac{1}{2})\mathrm{erf}(\sqrt{R_s}(1-2\lambda))+(2\lambda-\frac{1}{2})\mathrm{erf}(\sqrt{R_s}(1-4\lambda))\right]; & 0<\lambda<1/4 \\ \frac{A}{4}\,\mathrm{erf}(\sqrt{R_s}(1-2\lambda)) ; & 1/4<\lambda<1/2 \end{cases} \quad (29)$$

Fig. 3 plots the S-curves (divided by A) for the two cases. The S-curve for the implementation with opposite sign has a higher peak and a slope which is 3 times larger at $\lambda=0$, which in turn will yield a better performance. However, it also possesses an undesirable stable lock point at $\lambda=0.5$. It is not clear which implementation (same sign or opposite sign) is used in the SSDBS.

4. NOISE SPECTRAL DENSITY

For both loop implementations, the equivalent additive noise spectral density $S(\omega,\lambda)$ at zero frequency is given by

$$S(0,\lambda) = T\left[R_0(0,\lambda) + 2\sum_{m=1}^{\infty} R_0(m,\lambda)\right] \quad (30)$$

where

$$R_0(m,\lambda) = E_{n,s}[e_k e_{k+m}|\lambda] - g^2(\lambda) \quad (31)$$

After some tedious evaluation, we obtain

ORIGINAL PAGE IS
OF POOR QUALITY

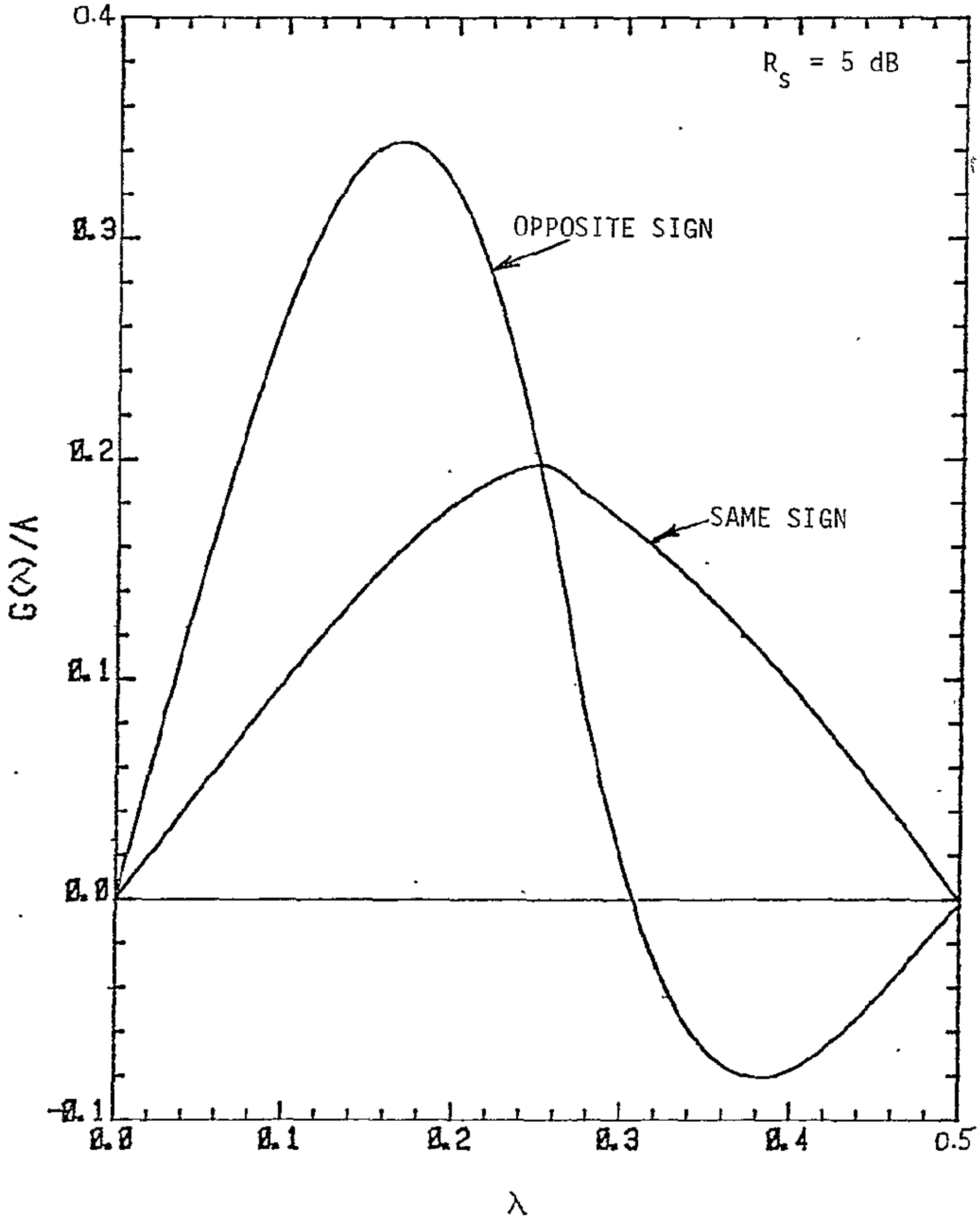

Fig. 3. Phase Detector Characteristic for Two Possible Implementations of DTTL.

$R_0(0,0)$

$$= \sigma^2\{3 + \frac{1}{2} R_s[1 - \mathrm{erf}^2(\sqrt{R_s})] - \sqrt{\frac{R_s}{\pi}}\,\mathrm{erf}(\sqrt{R_s})e^{-R_s} - \frac{1}{2\pi} e^{-2R_s}\} \tag{32}$$

$R_0(1,0)$

$$= \frac{\sigma^2}{16}\{\frac{2}{\pi} e^{-2R_s} + 4\sqrt{\frac{R_s}{\pi}}\,\mathrm{erf}(\sqrt{R_s})e^{-R_s} - 2R_s[1-\mathrm{erf}^2(\sqrt{R_s})]\} \tag{33}$$

It can be shown that $R_0(m,0)=0$ for all $m > 1$. Therefore,

$$S(0,0) = 3\sigma^2T\{1 + \frac{1}{12} R_s[1-\mathrm{erf}^2(\sqrt{R_s})] - \frac{1}{6}\sqrt{\frac{R_s}{\pi}}\,\mathrm{erf}(\sqrt{R_s})e^{-R_s} - \frac{1}{12\pi} e^{-2R_s}\} \tag{34}$$

Define the normalized noise spectrum $h(0)$ to be

$$h(0) = \frac{S(0,0)}{S(0,0)\big|_{R_s\to\infty}} = \frac{S(0,0)}{3\sigma^2T} \tag{35}$$

5. CLOCK JITTER

In the steady state, $\lambda \approx 0$, so $g(\lambda)$ can be approximated by the first two compnents of its Taylor expansion

$$\begin{aligned} g(\lambda) &\approx g(0) + g'(0)\lambda \\ &= g'(0)\lambda \end{aligned} \tag{36}$$

Substitute (36) into (1), we have

$$p(\lambda) \approx C\exp[\frac{-g'(0)\lambda^2}{KS(0,0)}] \tag{37}$$

The variance of λ is given by

$$\sigma_\lambda^2 = \frac{KS(0,0)}{2g'(0)} = \frac{W_{L0}Th(0)}{8R_s g_n'(0)} = \frac{B_L Th(0)}{12R_s[g_n'(0)]^2} \tag{38}$$

where

$$W_{L0} = \frac{1}{2}KA, \qquad B_L = \frac{1}{4}Kg'(0) \tag{39}$$

The clock jitter σ_λ is readily obtained from (38). Fig. 4 plots the normalized clock jitter (in % of symbol) as a function of E_b/N_0 (in dB). The loop implementation which gives the S-curve with the greater slope at the origin is assumed. The standard DTTL [2] performance for NRZ format (ξ_0= 1.0, 0.5, 1/6) are also shown as a comparison.

6. SYMBOL SLIP RATE

We make the approximation that the rate of symbol slipping events for a second-order loop is the same as the symbol-slip rate for a first-order loop. Then the expected time between two slipping events is given by [3]

$$\bar{T} = \frac{2}{\gamma}\int_0^{\lambda_p/2}\left[\int_\lambda^{\lambda_p/2} \exp\left(\alpha\int_\lambda^x g(y)dy\right)dx + \int_\lambda^{\lambda_p/2} \exp\left(-\alpha\int_\lambda^x g(y)dy\right)dx\right]d\lambda \tag{40}$$

where

$$\lambda_p = \text{period of } g(\lambda) = 1$$

$$\alpha = \frac{2}{KS(0,0)}$$

$$\gamma = \frac{S(0,0)K^2}{2}$$

Let $\alpha' g_n(\lambda) = \alpha g(\lambda)$, then Eq. (40) becomes

ORIGINAL PAGE IS
OF POOR QUALITY

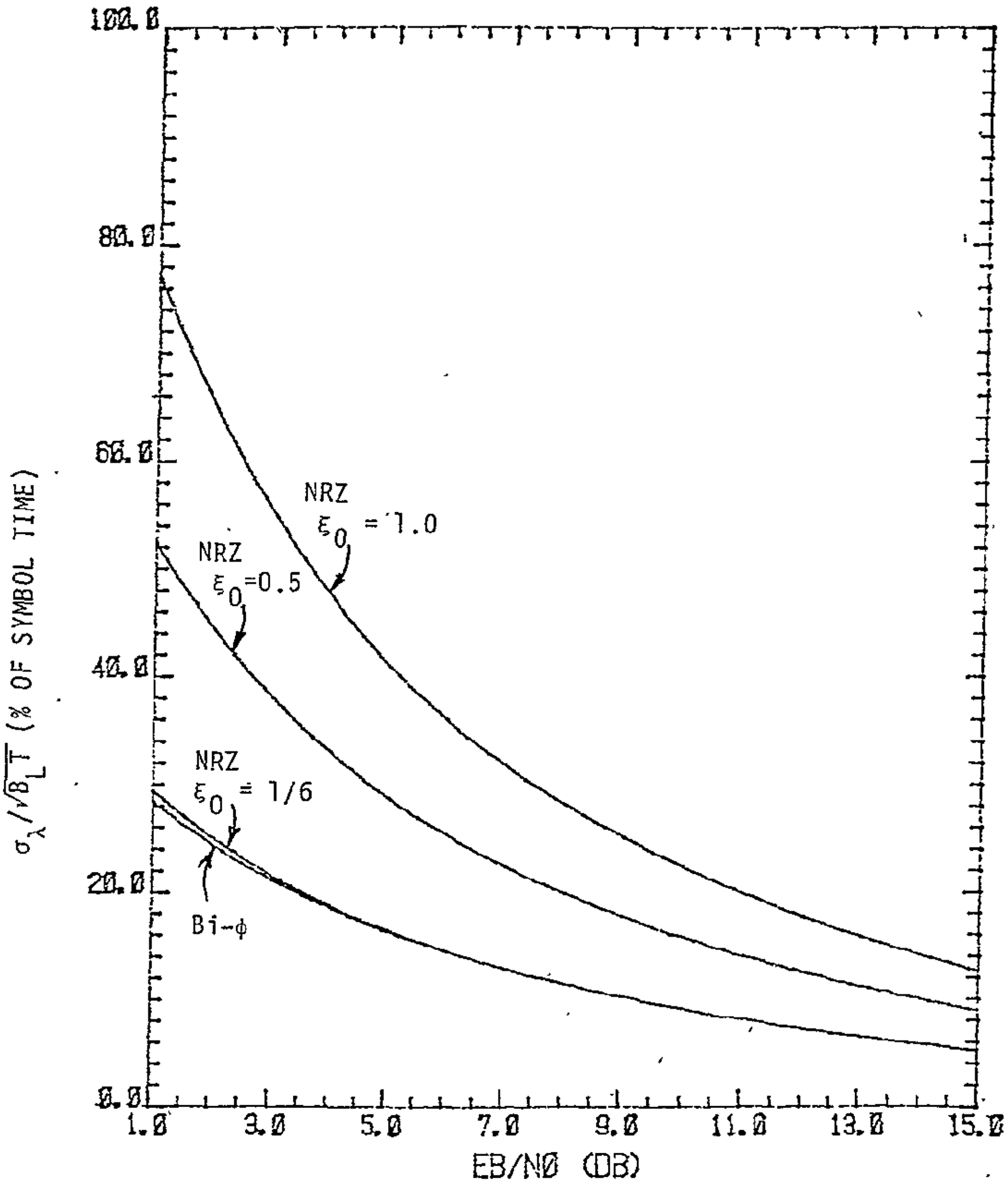

Figure 4. Data Transition Tracking Loop Performance.

$$\tilde{T} = \frac{2}{\gamma}\int_0^{1/2} \Big[\int_\lambda^{1/2} \exp\Big(\alpha'\int_\lambda^x g_n(y)dy\Big)dx + \int_\lambda^{1/2} \exp\Big(-\alpha'\int_\lambda^x g(y)dy\Big)dx\Big]d\lambda \qquad (41)$$

The symbol slip rate is defined as

$$P_{bs} = T/\tilde{T} \qquad (42)$$

where T = 1/symbol rate.

REFERENCES

1. Motorola Technical Proposal 2502-500, June 30, 1978. Prepared for Harris Electronic Systems Division.

2. Lindsey, W. C., and Simon, M. K., Telecommunication Systems Engineering, Prentice-Hall, Inc., Englewood Cliffs, NJ, 1973.

3. Braun, W. R., Lindsey, W. C., McKenzie, T. M., Tai, T., Wang, C., "Second Interim Report, TDRSS/RFI Communication Analysis, Modeling and Simulation Study," Contract No. NAS 5-25681, LinCom Corp., Pasadena, CA, April, 1981.

2. S-BAND AND KU-BAND COMMUNICATION LINK PERFORMANCE ANALYSES

2.1 INTRODUCTION

This chapter is a report on the work done under Task #2, which requires the evaluation of the performance of the Shuttle/TDRSS S-band and Ku-band communications links. Such evaluations were performed on several aspects of the links. They are reported on in the following sections and in Attachments 1 and 2 of this final report.

The sections to follow in this chapter are these. Section 2.2 is an assessment of the Shuttle's contribution to the phase noise performance of the TDRSS Ku-Band autotrack system. Section 2.3 presents a first study of the false lock phenomenon in the Shuttle/TDRSS S-band PN-code tracking loop. The phenomenon is observed at high SNR. Several fixes are proposed in the section. In Section 2.4 further analysis of the same problem is given. One particular false-lock mechanism is identified and the loop behavior is quantified. LinCsim's predictions of the CNR degradation to bit error rate due to radio frequency interference (RFI) on the Shuttle/TDRSS S-band return link are given in Section 2.5. (The model used in LinCsim is described in Section 4.2 of this final report.) Finally, in Section 2.6 a prediction of the RFI effect on acquisition of the Shuttle S-Band Demodulator/Bit Synchronizer is made, with supporting analysis presented.

Some other evaluations of the Shuttle/TDRSS communications links performance are documented in Attachments 1 and 2. Attachment 1 is a memo written on June 10, 1982, about the false-lock problem of the Shuttle's Payload Signal Processor. It gave LinCom's understanding of the problem, possible sources of the problem, and potential solutions. Attachment 2 is a memo written on October 14, 1982, which addressed

addressed two areas, the measurement and mitigation of the RFI on the Shuttle/TDRSS S-band return link and the maximum user spacecraft dynamics which can be handled by the Wide Dynamics Demodulator.

2.2 SHUTTLE CONTRIBUTION TO PHASE NOISE PERFORMANCE OF KU-BAND AUTOTRACK SYSTEM

1. Introduction

The Shuttle uses TDRSS to relay data to the ground via a Ku-band unbalanced QPSK (UQPSK) signal format signaling scheme (e.g., mode 1 transmission in the return link). In order to point the KSA antenna properly at the Shuttle source, the TDRSS uses a single channel monopulse autotrack system. The Shuttle VCO used for the generation of the signal introduces noise into the phase of the signals.

Although analyses for TDRSS autotrack noise performance have been made in the past, they have not explicitly included the phase noise in the user received signal. Figure 1 shows the phase noise profile of the Shuttle VCO at 1.875 GHz. 1.875 GHz is the frequency used for UQPSK signals. As the figure shows, most of the phase noise power, i.e. from 0 dB to -50 dB, lies in the low frequency offset (0 Hz to 10 Hz) from the carrier. Since the performance of the TDRS autotrack system degrades in the presence of various noises such as the thermal noise, incidental AM, etc., it is desirable to obtain the effects of the phase noise in the region of low frequency offset from the carrier on the performance of the autotrack system, if any.

2. Summary

The performance of KSA single channel monopulse system is analyzed against the phase noise added by the Shuttle VCO. After the analysis it becomes clear that the low frequency phase noise added by the Shuttle VCO will not affect the autotrack system mainly because the autotrack

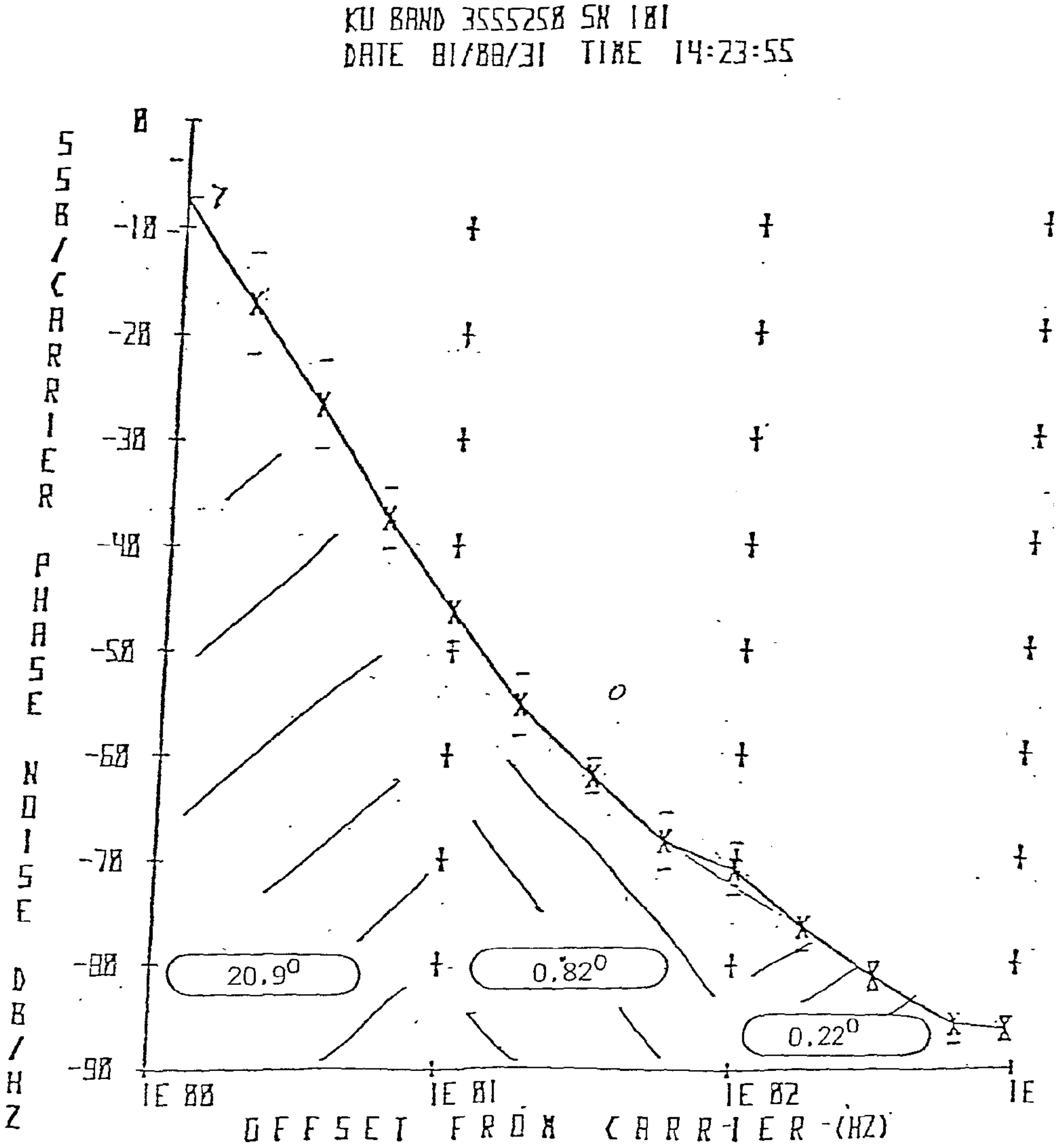

Figure 1. Phase Noise Profile of Shuttle VCO at 1.895 GHz.

error signals are in the amplitude of the signal while the phase noise added is in the phase of the signal. The phase noise, the thermal noise and the signal, after passing through the square law amplitude detector produce respective components of signal and noise. The slowly varying component of phase noise appears as a constant as compared to the accompanying fast varying thermal noise component because the bandwidths of the filters following the square law device is much larger than bandwidth of the slowly varying phase noise. Since the phase noise is in the phase of the signal which multiplies the thermal noise components, the correlation and consequently the power spectrum of the noise output of the square law detector is independent of the slow varying phase noise. This does not hold for fast varying phase noise and an expression is derived for the power spectrum of noise.

3. TDRS Single Channel Monopulse Signal Generation

Figure 2 shows the single channel monopulse signal generating system. As shown in the figure, the autotrack system uses a five horn feed. Energy collected by four of these horns is compared to form two autotrack error signals. The azimuth channel producing azimuth error and the elevation channel yielding the elevation error. These errors are in the amplitudes of the respective signals.

The phase noise riding on the phase of the received UQPSK signal stays in the phase of the signals whose amplitudes carry the azimuth and elevation error signals. These error signals are time multiplexed or biphase modulated by the orthogonal switching signals $S_\alpha(t)$ and $S_\beta(t)$. This operation is indicated by a switch in Figure 2. Figure 3 shows the $S_\alpha(t)$ and $S_\beta(t)$ pulse trains and their respective line spectra.

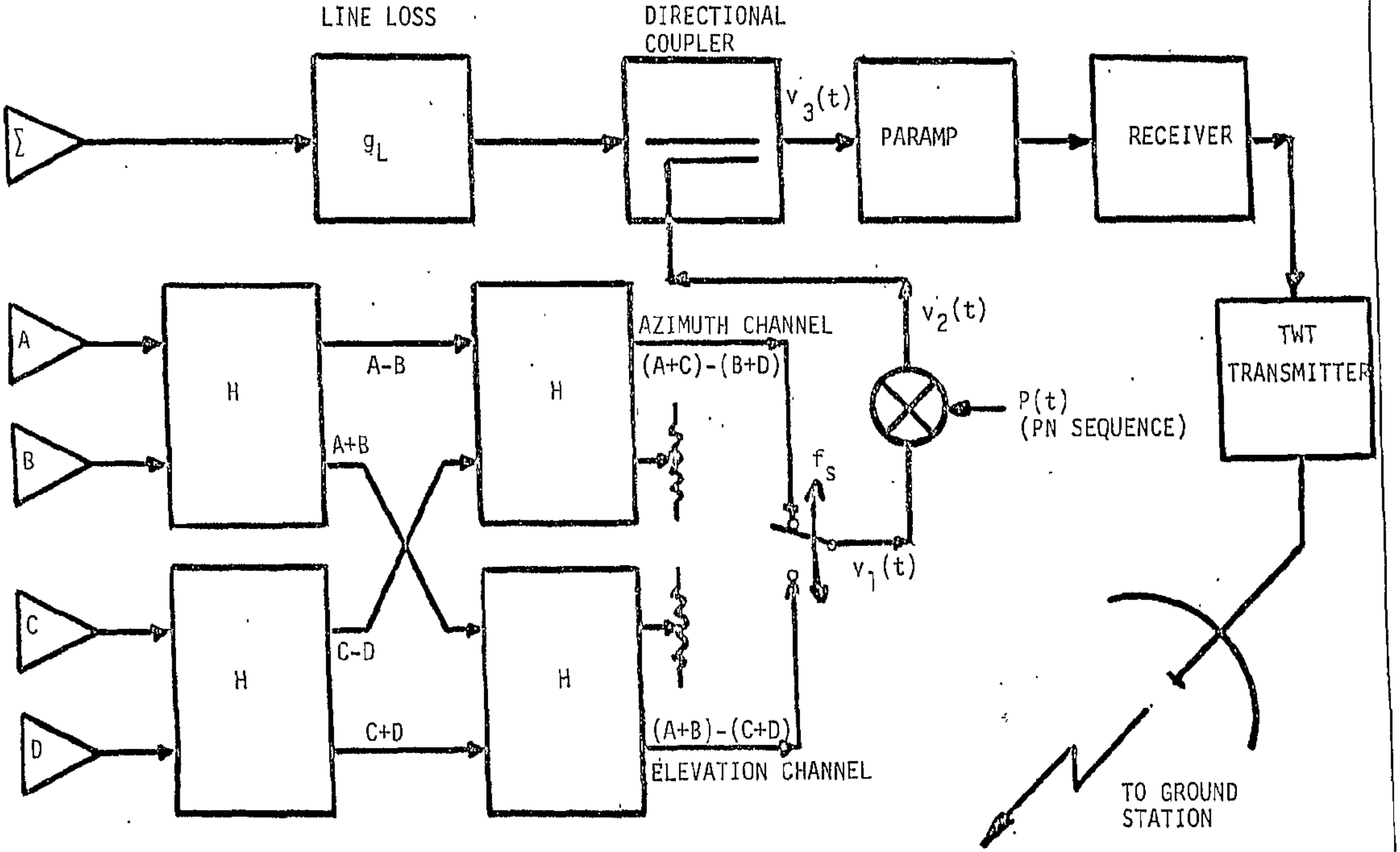

Figure 2. Single Channel Monopulse Signal Generation on TDRSS.

Received signal

$$v_r(t) = \sqrt{2}\, AD_2(t)\cos(\omega_0 t+\theta_2(t)) - \sqrt{2}\, aD_1(t)\sin(\omega_0 t+\theta_1(t))$$

$$= \sqrt{2}\, AR(t)\cos[\omega_0 t+\theta_2(t)+\psi(t)]$$

where

$$R(t) = \sqrt{1+ (\tfrac{a}{A})^2 - 2(\tfrac{a}{A})D_1(t)D_2(t)\sin\,\delta(t)}$$

$$\psi(t) = \tan^{-1}\left[\frac{\frac{aD_1(t)}{AD_2(t)}\cos\,\delta(t)}{1-\frac{aD_1(t)}{aD_2(t)}\sin\,\delta(t)}\right]$$

$$\delta(t) = \theta_2(t) - \theta_1(t)$$

$\theta_1(t)$ and $\theta_2(t)$ are the phase noise added by Shuttle to the two data train carrier. In order to use this signal for an AM monopulse signal we rely on constant envelope property of this signal which implies that $\theta_1(t) \cong \theta_2(t)$ giving $\delta(t) \cong 0$.

The elevation and azimuth errors M(t) are in the amplitude of signal $v_1(t)$ in Figure 2. The amplitude and the spectrum associated with it is shown in Figure 3. This composite single channel signal $v_1(t)$ is amplitude modulated by the PN waveform P(t) at a rate somewhat higher than f_s, the swtiching rate of the switch. The code used is a Manchester code and the spectrum of the code is shown in the Figure 3. The basic purpose of the code is to spread the spectrum of $v_1(t)$. Figure 3 shows the spectrum of M(t)P(t).

The single channel monopulse signal is obtained here, as an AM modulation system by adding, in phase, (coupling) a small fraction of

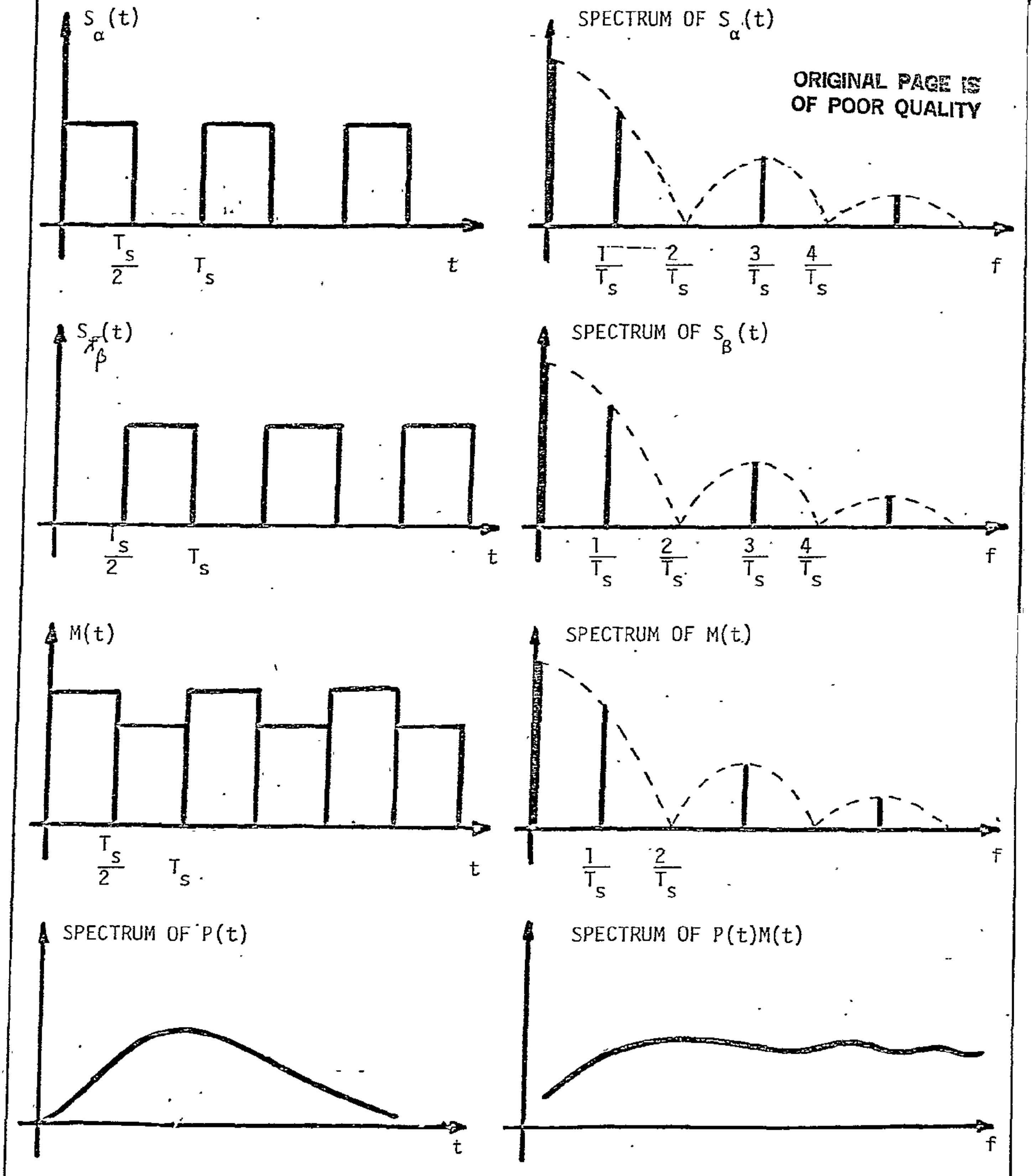

Figure 3. Signals and Their Respective Spectra of the Monopulse Signal Generating System.

the single channel difference signal to the sum channel signal to produce the output of the directional coupled. This signal, shown in Figure 3 as $v_2(t)$ and has the form

$$v_3(t) = \underbrace{\sqrt{2}\,A_cR(t)}_{\substack{\text{system}\\ \text{constants}}}\ \underbrace{(1+K_LP(t)M(t))}_{\substack{\text{angle error}\\ \text{term}}}\underbrace{\cos(\omega_0t + \theta_2(t) + \psi(t))}_{\text{phase noise term}}$$

This signal is amplified and radiated to ground for processing.

4. Ground Processing of Monopulse Signals

The single channel monopulse signal as AM modulation on the wideband data signal is transmitted to the ground station. The ground station receiver tracks the signal, provides AGC and demodulates the data. At a convenient IF frequency the signal is taken for square law detection. The bandwidth of this signal, B_{IF}, is 4 MHz $\leq B_{IF} \leq$ 150 MHz. Actually it is a bank of bandpass filters and the selection is made depending on user signal dynamics. Figure 4 depicts the ground processing of the autotrack signals. Output $v_{g_1}(t)$ of the IF amplifier, is a wideband signal with $B_{IF} \geq 4$ MHz.

This wideband signal with the autotrack error signals in the amplitude is passed through an amplitude detector which is functionally a square law device with AGC. This AGC does not track the faster moving components of the amplitude with frequency f_s. Hence the output of the square law device has the form.

$$v_{g_2}(t) = v_{g_1}^2(t) = \text{signal x signal + signal x noise + noise x noise}$$

$$= \underbrace{2A_d^2K_LP(t)M(t)}_{\substack{\text{desired}\\ \text{signal}}} + \sqrt{\frac{c}{2(1+r^2)}}\ \underbrace{(1+K_LM(t))\ n_{sn}(t)}_{\substack{\text{noise containing}\\ \text{phase noise } \theta(t)}} + n_{nn}(t)$$

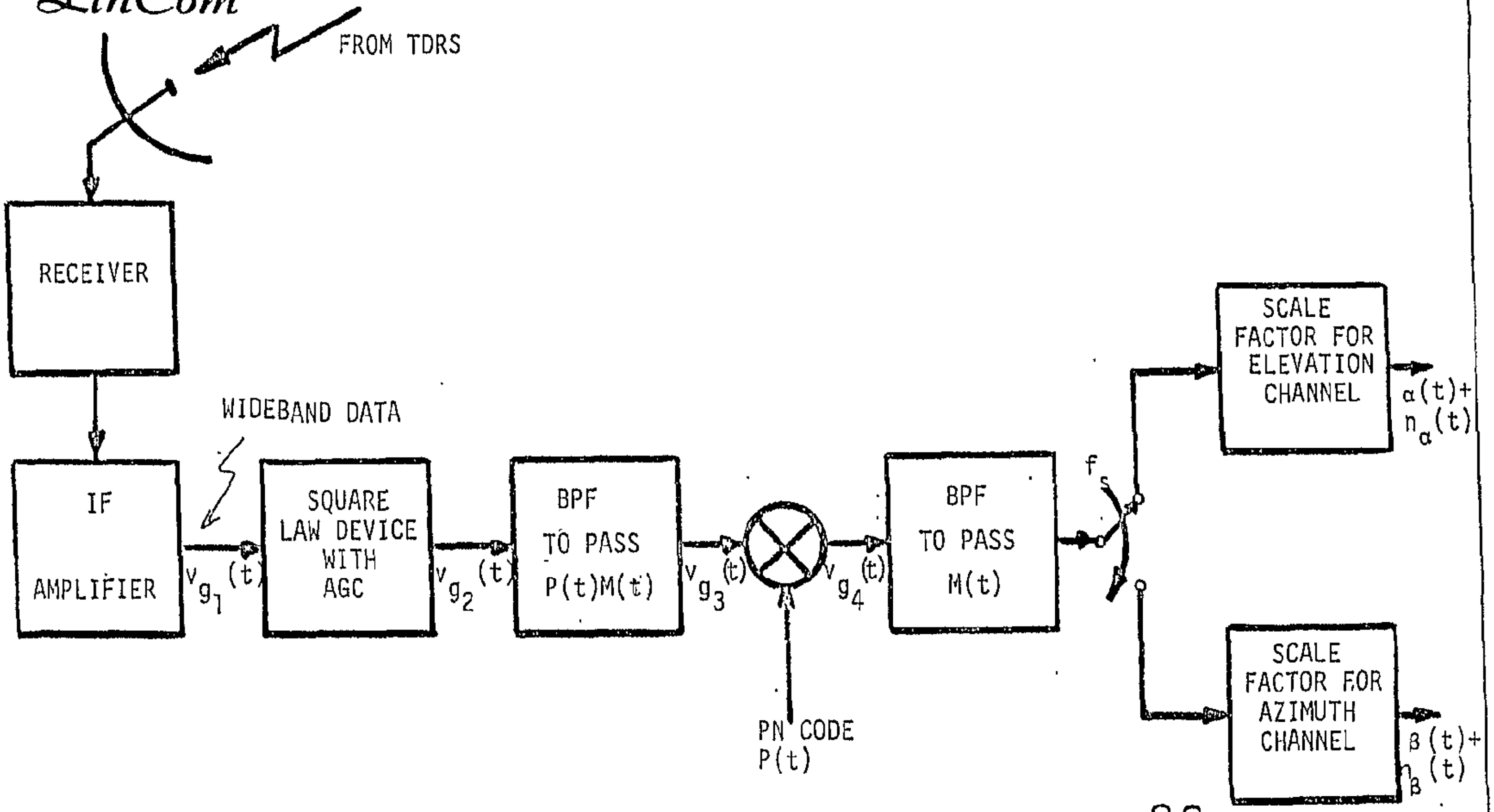

Figure 4. Ground Processing of the Monopulse Signals.

where

$$n_{sn}(t) = D_2(t)[n_c(t)\cos\theta(t) + n_s(t)\sin\theta(t)] + rD_1(t)[n_s(t)\cos\theta(t) - n_c(t)\sin\theta(t)]$$

where $n_c(t)$ and $n_s(t)$ are the usual narrowband representation of the noise. This noise has various components such as the thermal noise, antenna noise, equipment noise, etc.

The bandpass filter after the square law device is made wide enough to pass P(t)M(t), which is a wideband process. The noise passes through the filter hence the bandwidth of the noise processes become equal to the bandwidth of P(t)M(t). As shown in Figure 4, the PN code is now removed by forming the multplication $v_{g_3}(t)P(t)$ to obtain the monopulse modulation term M(t). This multiplication produces two new noise processes, $n'_{sn}(t)$ and $n'_{nm}(t)$ which are the result of switching relatively wideband noise processes by a relatively narrowband periodic waveform P(t). This implies that the spectrum of $n'_{rs}(t)$ will be the spectrum of $n_{ns}(t)$ reproduced at every line of P(t) and similarly spectrum of $n'_{nn}(t)$ is the spectrum of $n_{nn}(t)$ reproduced at every line of P(t). The resulting noise spectral densities of $n'_{ns}(t)$ and $n'_{nm}(t)$ are of interest only near f=0 because these densities will be seen by the demodulated azimuth and elevation error signals.

The elevation and azimuth channel signals are obtained by switching $v_{g_4}(t)$. The switching for α as well as β channels is done at a rate which is much less than the bandwidth of noise with similar results as in the case of despreading operation described above

$$\text{demodulated elevation channel output} = \alpha(t) + n'_{ns}(t) + n'_{nm}(t)$$

$$n'_{ns}(t) = D_2(t)[n_c(t)\cos\theta(t)+n_s(t)\sin\theta(t)]$$

$$+ rD_1(t)[n_s(t)\cos\theta(t) - n_c(t)\sin\theta(t)]$$

The bandwidth of $n'_{ns}(t)$ is now equal to the bandwidth of the lowpass filter, designed to pass M(t) hence it is about 1 KHz. The Shuttle phase noise $\theta(t)$ appears in the cross noise term only. This phase noise is a very slowly varying term as compared to the $n_c(t)$ and $n_s(t)$ because most of the power of $\theta(t)$ is in low offset from the carrier (see Fig. 1). Let us say $\theta(t) = \theta_s(t) + \theta_f(t)$ where $\theta_s(t)$ is the slowly varying component of $\theta(t)$ and $\theta_f(t)$ is fast varying component of $\theta(t)$. $S_{\theta_s}(f) + S_{\theta_f}(f)$ gives us the power spectrum of Fig. 1. The fastness and slowness is as compared to the $n_c(t)$ and $n_s(t)$ noises. Computation of the correlation function of $n'_{ns}(t)$ gives us

$$R_{n_s}(\tau) = R_n(\tau)[R_{D_2}(\tau)+r^2R_{D_1}(\tau)][1- \sigma^2_{\theta_f}(1+\tfrac{1}{4}\sigma^2_{\theta_f}) + \tfrac{1}{2}R^2{}_{\theta_f}(t)+R_{\theta_f}(\tau)]$$

Note that there exists no slow frequency term at all. Since Most of the phase noise power is concentrated in the region at low frequency offset from the carrier,

$$R_{n_s} = R_n(\tau)[R_{D_2}(\tau) + r^2R_{D_1}(\tau)]$$

spectral density near f=0 is given by

$$S_{n_s}(\omega) = S_n(\omega)[S_{D_2}(\omega) + r^2 S_{D_1}(\omega)]$$

5. Conclusion

The slow frequency component $(|f| < 1$ KH) of the Shuttle phase noise does not affect the performance of the KSA amplitude monopulse autotrack system. The fast frequency component θ_f of the phase noise does affect the modulation of the monopulse signal but the effect is small because very little power of the phase noise is present at these frequencies.

REFERENCES

1. "Thermal Noise and User Incidental AM Performance of KSA Autotrack System," TDRSS technical fact finding responses for the ground segment prepared by Western Union, Harris Electronic Systems Division and TRW Defense Systems Group, October 1976.
2. "Telecommunication Services via a Tracking and Data Relay Satellite System," System Design report prepared by Western Union, Harris Electronic Systems Division and TRW Defense Systems Group, March 1977.
3. "TDRSS Angle Tracking System," prepared by TRW Defense Systems Group, Sept. 1981.
4. "TDRSS Ground Segment Final Design Review Data Package," Volume IV, Book 1, prepared by TRW Defense System Group, Sept. 1981.

2.3 A FIRST STUDY OF FALSE LOCK PHENOMENON IN SHUTTLE/TDRSS S-BAND PN CODE TRACKING LOOP

Abstract

The purpose of this report is to present and verify the conjecture that the PN code tracking loop in the Shuttle S-band receiver can exhibit false code lock phenomenon (stable false lock points) at high signal-to-noise ratios due to precorrelation and postcorrelation RF/IF filtering. At low SNR's these stable points would seem to have little effect. Another possible ill effect at high SNR's is crossing of the low threshold setting in the "on-time" acquisition channel. Further analysis, computer programming and numerical work for the specific filters implemented is required before the actual phenomenon exhibited by pre- and post-correlation filtering in the Shuttle S-band PN despreader (forward link) can be fully quantified. Finally, in this report several approaches to fixing this problem are presented.

1.0 INTRODUCTION

Code acquisition on the Shuttle's forward link involves performing search for the correct code phase position with the locally generated code until sufficient correlation exists to announce code acquisition with a high degree of confidence. This correlation concept is depicted in Figure 1 where the RF/IF output is despread by the locally generated PN code and further processed in a bandpass filter. At the output of this filter an energy measurement is made to determine the degree of correlation for the particularly chosen code phase position. When this correlation, say $C(\tau-\hat{\tau})$ exceeds a certain value, code acquisition is announced and handover to the PN code tracking loop is made. The actual code used is a maximal length shift register sequence of length $L = 1023$ chips and the integration time, T_I, is greater than one code period. Therefore, it would appear that false acquisitions due to partical correlations would not be a problem.

In the handover mode the PN code tracking loop, a τ-dither mechanization, is designed to complete the fine acquisition process (pull-in) and maintain track of the input code phase relative to the locally generated code epoch. (See Figure 2 for a conceptual functional model of despreading process.) Here the received spread spectrum signal is down converted and effectively filtered by the cascade of bandpass RF and IF filters before application to the PN code tracking loop. The output of the code tracking loop serves as the "on-time" reference PN signal for despreading the input signal. This despread signal is then applied to the carrier synchronization system (CSS) for demodulation and symbol detection and decoding for message recovery.

The effectiveness of the frequency spreading is limited by the

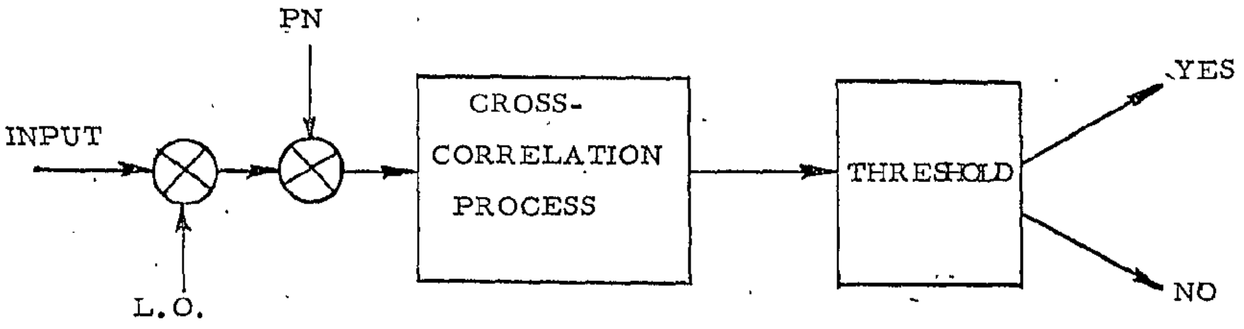

Figure 1. Techniques for Generating Decisions to Drive Code Sync Algorithm.

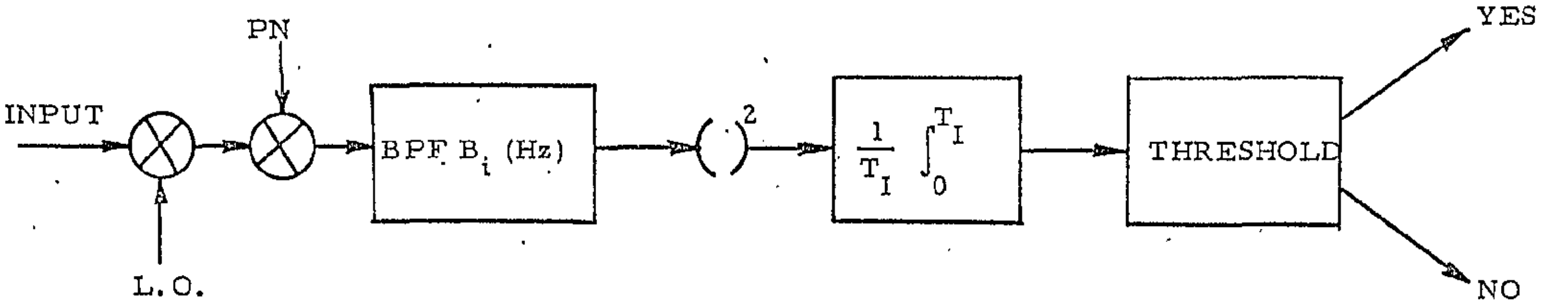

Figure 2. Noncoherent Correlation Process.

frequency response of the RF/IF filtering and more generally the overall frequency response of the channel. This end-to-end frequency response of the channel may be limited by the bandwidth attainable in these filters as well as their amplitude and phase response.

The purpose of this report is to investigate the conjecture that filtering of transmitted and received signal (pre- and post-correlation) followed by noncoherent detection of the correlation process to form an error signal in the code tracking loop can lead to partial correlations in the code loop S-curve. These partial correlations can then serve as stable lock points at high signal-to-noise ratios. Such lock points constitute false code phase lock points.

The functional diagram of the time-shared (τ-dither) delay locked loop (DLL) is illustrated in Figure 3. The loop generates the S-curve or error signal $E(\tau-\hat{\tau})$ for purposes of maintaining code track. It is desired to have the design work such that this error signal $E(\tau-\hat{\tau})$ will be non-zero on the average for small synchronization errors. During initial acquisition the hypothesized code epoch $\hat{\tau}$ is varied and the on-time correlation $C(\tau-\hat{\tau})$, illustrated in Figure 2, is observed to determine coarse correct synchronization.

The effect of the pre- and post-filtering on the correlation $C(\tau-\hat{\tau})$ and the loop error signal $E(\tau-\hat{\tau})$ is largely determined by the impulse response of the RF/IF filtering. For a noncoherent delay-locked loop a computer program must be written to determine the exact effects; however, considerable insight into the zero crossings of the loop S-curve can be found by studying the zero crossings of the S-curve in a coherent τ-dither loop. In what follows results of this work are presented.

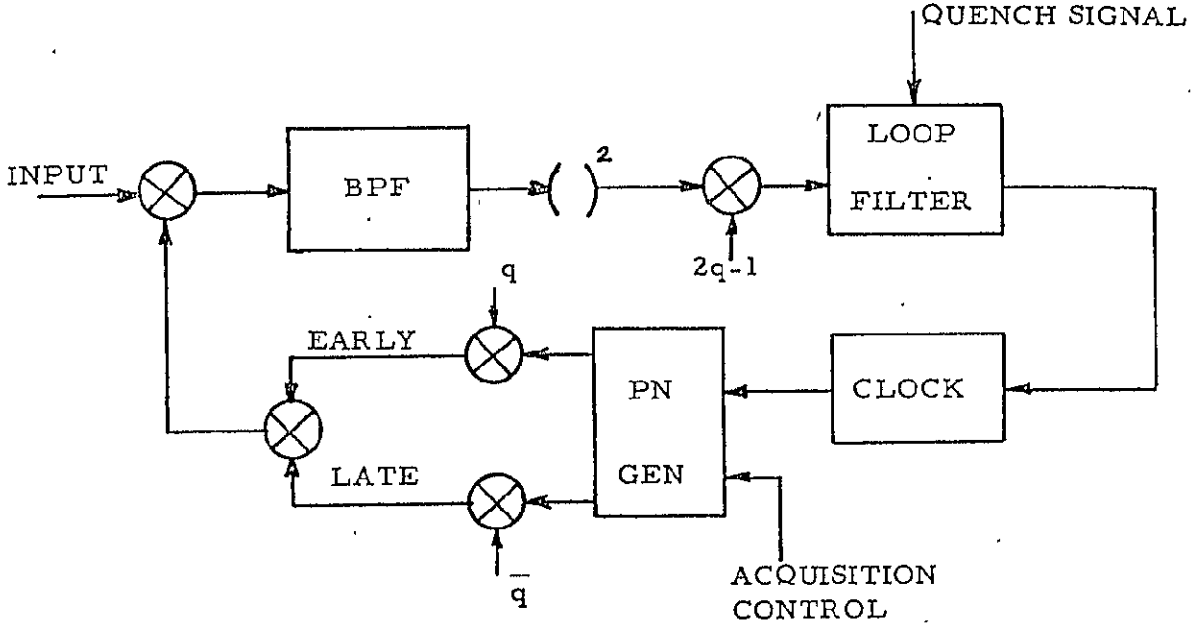

Figure 3. Time-Shared Delay Locked Loop.

2.0 MODEL AND NUMERICAL RESULTS

The functional diagram of the problem under consideration is provided in Figure 4. The analysis assumes that the PN-sequence has a two-level autocorrelation function with negligible out-of-phase correlation prior to filtering. Maximal length linear shift register sequences have these properties. The receiver recovers the carrier and generates the observables $C(\tau-\hat{\tau})$ and $E(\tau-\hat{\tau})$. The effect of the prefilter H(s) on the correlation and error signals can be determined using the computer to generate numerical data and graphs.

Figure 5 illustrates the amplitude response of Butterworth and Tchebycheff bandpass filter which have a 10 MHz center frequency a 2 MHz 3 dB bandwidth. Figure 6 shows the "on-time" correlation function as seen by the data channel, for the two filter responses illustrated in Figure 5. For comparison purposes the case of zero filtering (no distortion) is also illustrated. Figure 7 illustrates the error channel response for the filter responses shown in Figure 4 and for comparison purposes the case of no filtering is also shown.

3.0 ANALYSIS OF RESULTS

There are four significant features caused by channel filtering of the spread spectrum signal. Two of these are illustrated in Figure 6. First, there is a reduction in peak correlation available for carrier loop lock-up and data detection (processing loss). Second, there is partial correlation outside of the desired region which allows for carrier lock up at high signal-to-noise ratios.

The remaining two effects due to channel fitering have to do with the error signal shown in Figure 7. First the partial correlation also shows up in the error signal which drives the τ-dither delay-locked

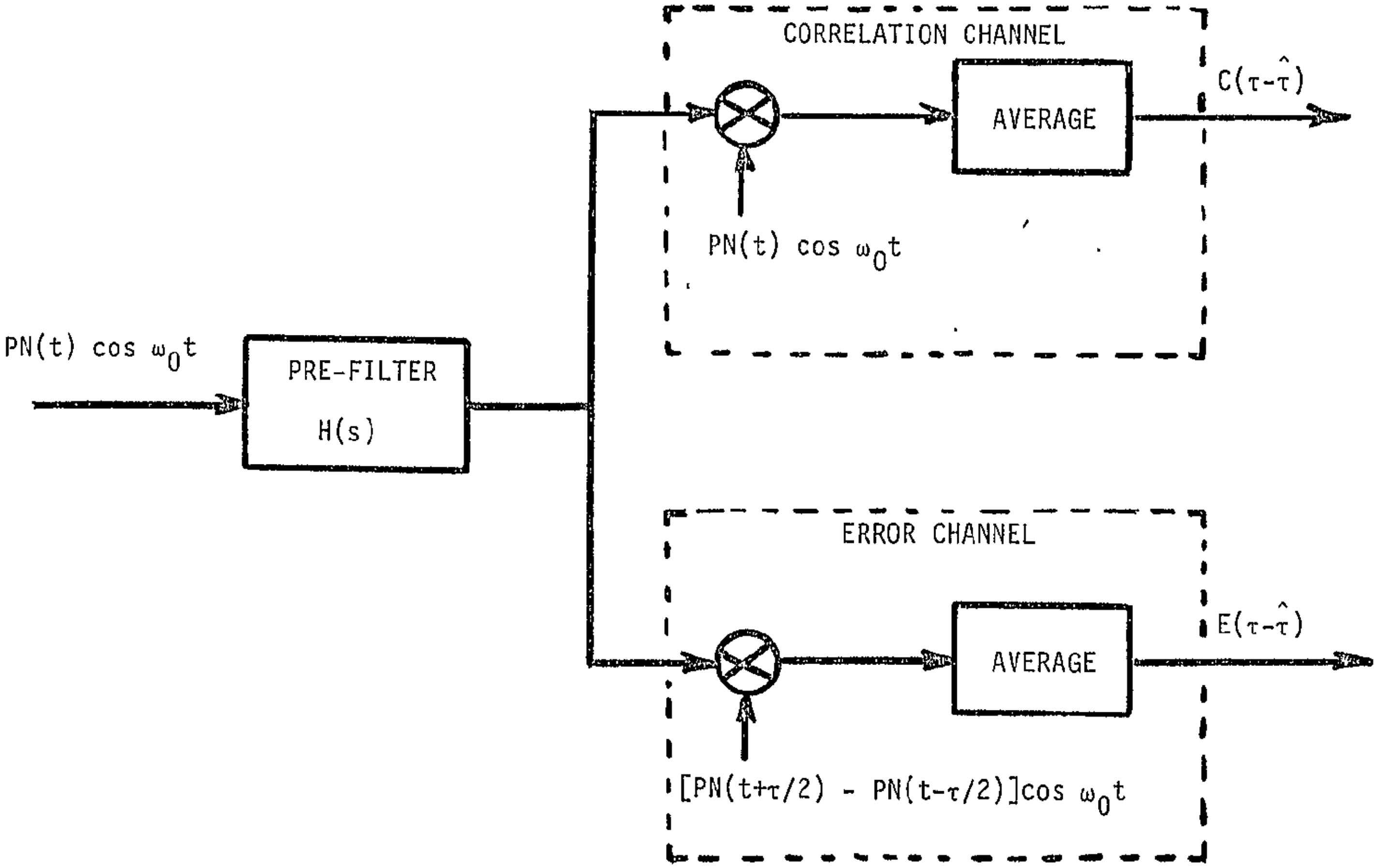

Figure 4. Simplified Functional Diagram of Receivers, Correlation and Error Channels.

ORIGINAL PAGE IS
OF POOR QUALITY

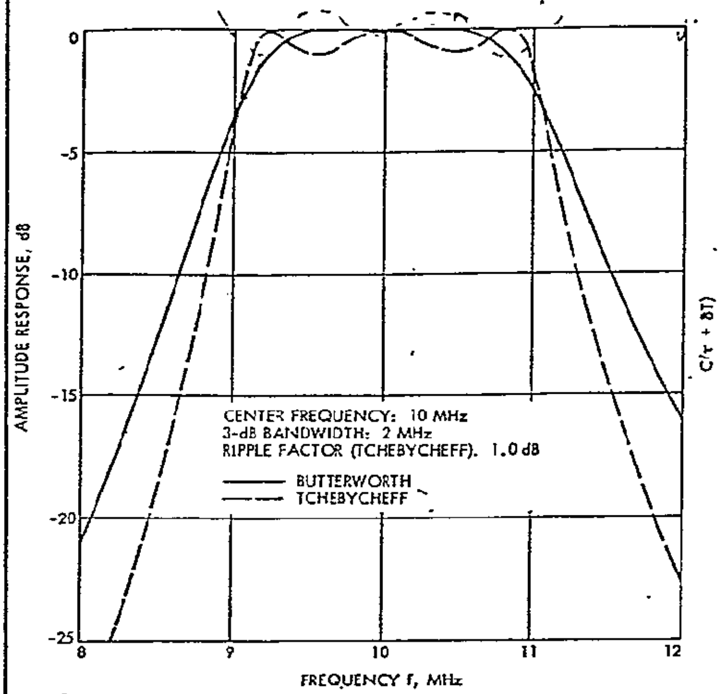

Figure 5. Amplitude Response of 6-Pole Butterworth and Tchebycheff Band-pass Filters.

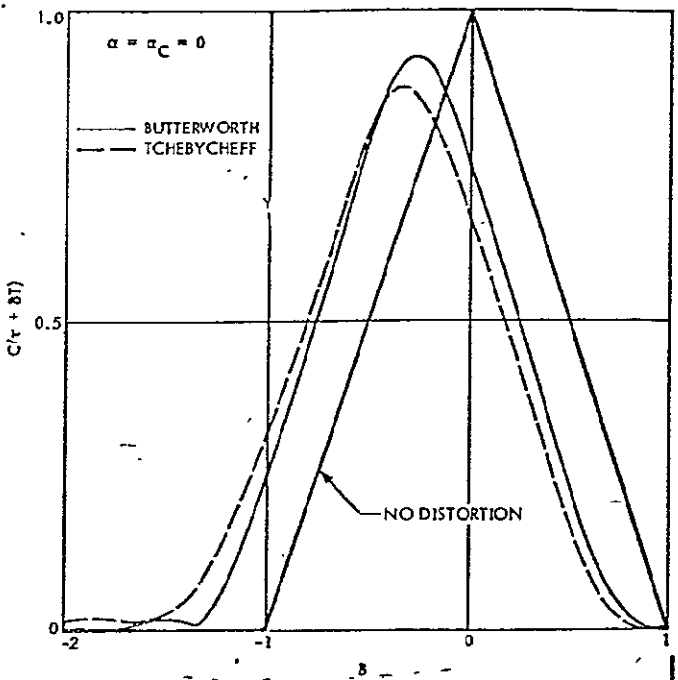

Figure 6. Effect of Butterworth and Tchebycheff Band-pass Filters on Correlation $C(\tau+\delta T)$.

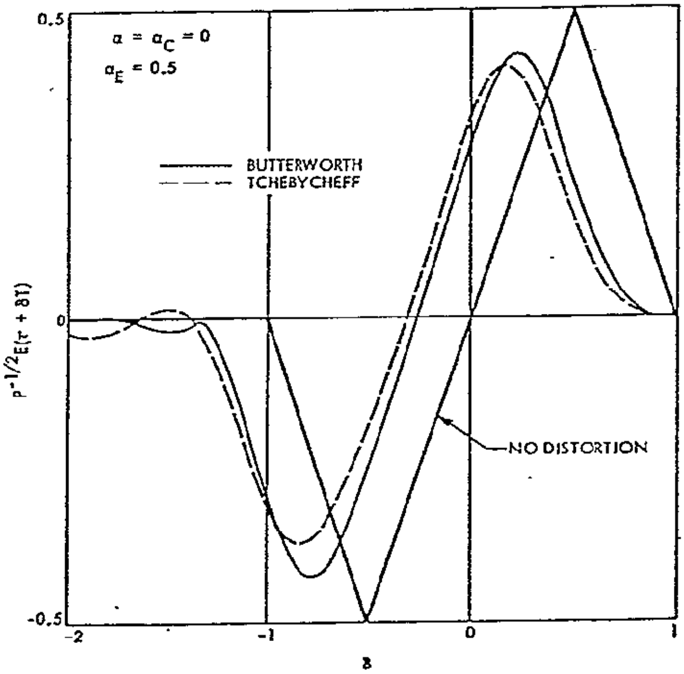

Figure 7. Effect of Butterworth and Tchebycheff Band-pass Filters on Error Signal $E(\tau+\delta T)$.

loop. In particular, the Tchebycheff filter causes zero crossings of the loop S-cruve in such a position as to give rise to the undesirable stable false lock points. These are seen by the loop at high signal-to-noise ratios. Finally, the desired phase lock point has been shifted causing a delay which will manifest itself as a bias or systematic range error in ranging measurements.

Further work is required in order to quantify the effects which would be seen at high SNR in the actual Shuttle S-Band despreader mechanization.

4.0 Fixes of the Problem

There are several fixes to the problem and, as usual, some simple and others more complex. I will briefly discuss these in what follows.

Fix One: At the expense of system threshold performance (perhaps 50 to 51 dB-Hz) the simplest fix which might work would be to raise the threshold setting in the "on-time" energy detection channel so that the probability of detection of the partial "off-time" correlation is extremely small at high SNR. With this fix the penalty will be the inability to detect code correlation at low signal-to-noise ratios. Hopefully, the "on-time" channel would always force the code loop to lock at the correct lock point.

Fix Two: Use a "two threshold" acquisition detector; one for high SNRs and one for low SNRs. This switching decision might be driven from the noncoherent AGC in the Costas loop. This fix might avoid giving up acquisition threshold performance at low SNRs.

Fix Three: If Fix One does not avoid false code lock, one may be forced to redesign the pre- and post-correlation filters in the "on-time/early-late" channels and reoptimize the threshold setting. The penalty will be code acquisition threshold performance.

Fix Four: Leave system filters as designed and re-design search strategy so as to continue to search over false-code lock regions after initial acquisition and detect the peak correlation, i.e., decide partial (false) correlation vs peak (true) correlation. It would seem that no penalty in system acquisition threshold performance would be paid.

Fix Five: Redesign pre- and/or post-correlation filters, use two code acquisition threshold settings driven by the Costas loop's noncoherent AGC. It would appear that no acquisition threshold performance has to be given up.

The system (carrier/code loop combined) acquisition performance at ESTL in late 1979 had the generic characteristic illustrated in the figure below.

Combined PN/Carrier Loop Acquisition Performance

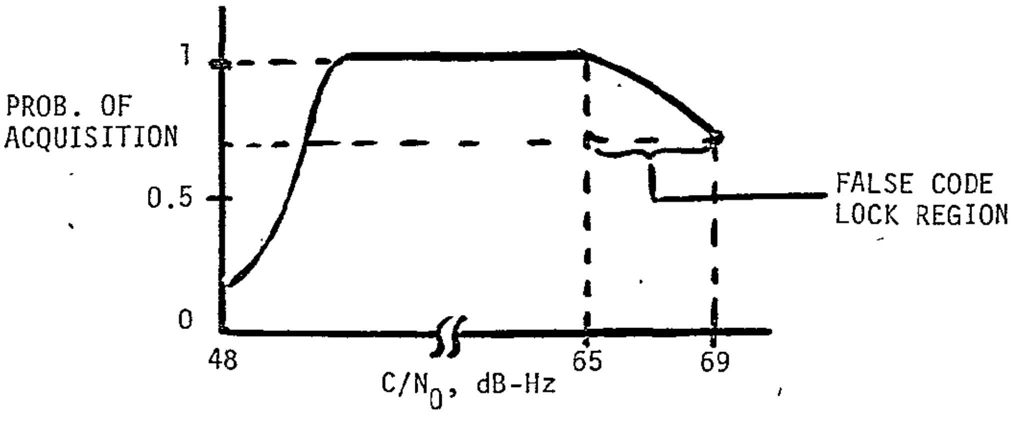

ORIGINAL PAGE IS
OF POOR QUALITY

2.4 FURTHER ANALYSIS OF FALSE LOCK PHENOMENON IN SHUTTLE/TDRSS S-BAND PN CODE TRACKING LOOP

This study of the false lock problem in the Noncoherent Delay Lock Loop (NDLL) is motivated by the false lock phenomenon manifested in the S-Band PM direct up/down link (MILA-SLSS Mode*). There is a possibility of false lock in the PN code loop during launch and ascent when MILA is in the TDRS Mode. According to the assessment report, the strong signal from MILA produces false lock. This report identifies one particular false lock mechanism, quantifies the behavior as well as the degradation in signal processing gain degradation due to differential path delays and IF filtering.

Computer simulations of loop S-curve and on-time correlation function are performed to quantify the loop S-curve lock points and the degradations in signal processing gain. Finite bandwidth prefiltering causes timing offsets in the NDLL loop S-curve and on-time correlation function. It appears that this offset is mainly due to the group delay present in the IF filter.

Undesired stable false lock points are shown to exist in the loop S-curve after prefiltering. These lock points cause loop "hangup" during acquisition at high signal-to-noise ratios if the on-time correlation function falls below the lock detection threshold when the timing error lies in the vicinity of these lock points.

The degradation in magnitude of the on-time correlation function gives rise to a signal processing gain loss, i.e., signal power degradation. This degradation, which is modulation dependent, is shown

---

*Refer to the Problem Assessment Report Line Item 30, July 17, 1980.

in Table 2. The S-curve and on-time correlation function are provided by two separate subsystems. Any timing offset between the desired lock point and the peak of the on-time correlation function developed in two different multipliers could exist due to differential delay mismatched between channels. This degradation, shown in Table 3, is significant even for an offset of a fraction of a chip time. Therefore, calibration and maintenance of this differential path delay must be maintained.

1. INTRODUCTION

This study of the false lock problem in noncoherent Delay Lock Loop (NDLL) is motivated by the false lock phenomenon in the S-Band PM direct up/down link (MILA-SLSS Mode). There is a possibility of false lock during launch and ascent when MILA is in the TDRS Mode. The strong signal from MILA produces false lock.

It is known that finite bandwidth filtering on signals will cause an offset of NDLL loop stable lock point. It also degrades the NDLL S-curve and signal processing gain. It is the purpose of this study to quantify this effect of finite filtering on false lock and data power degradation. Since analysis of these effects seems to be formidable, computer simulation of loop S-curve and on-time cross correlation function are simulated for this purpose.

2. SYSTEM MODEL

The loop structure of NDLL is shown in Fig. 1. For the purpose of this study noise is not considered here. The input signal s(t) is modeled as

$$s(t) = \sqrt{2S}\, s_{PN}(t-\tau)m(t-\tau)\cos(\omega_0 t+\theta) \qquad (1)$$

where

S = average signal power

$s_{PN}(t-\tau)$ = received PN sequence with transmission delay τ

$m(t-\tau)$ = data modulation with delay τ

ω_0 = carrier radian frequency

θ = random carirer phase

ORIGINAL PAGE IS
OF POOR QUALITY

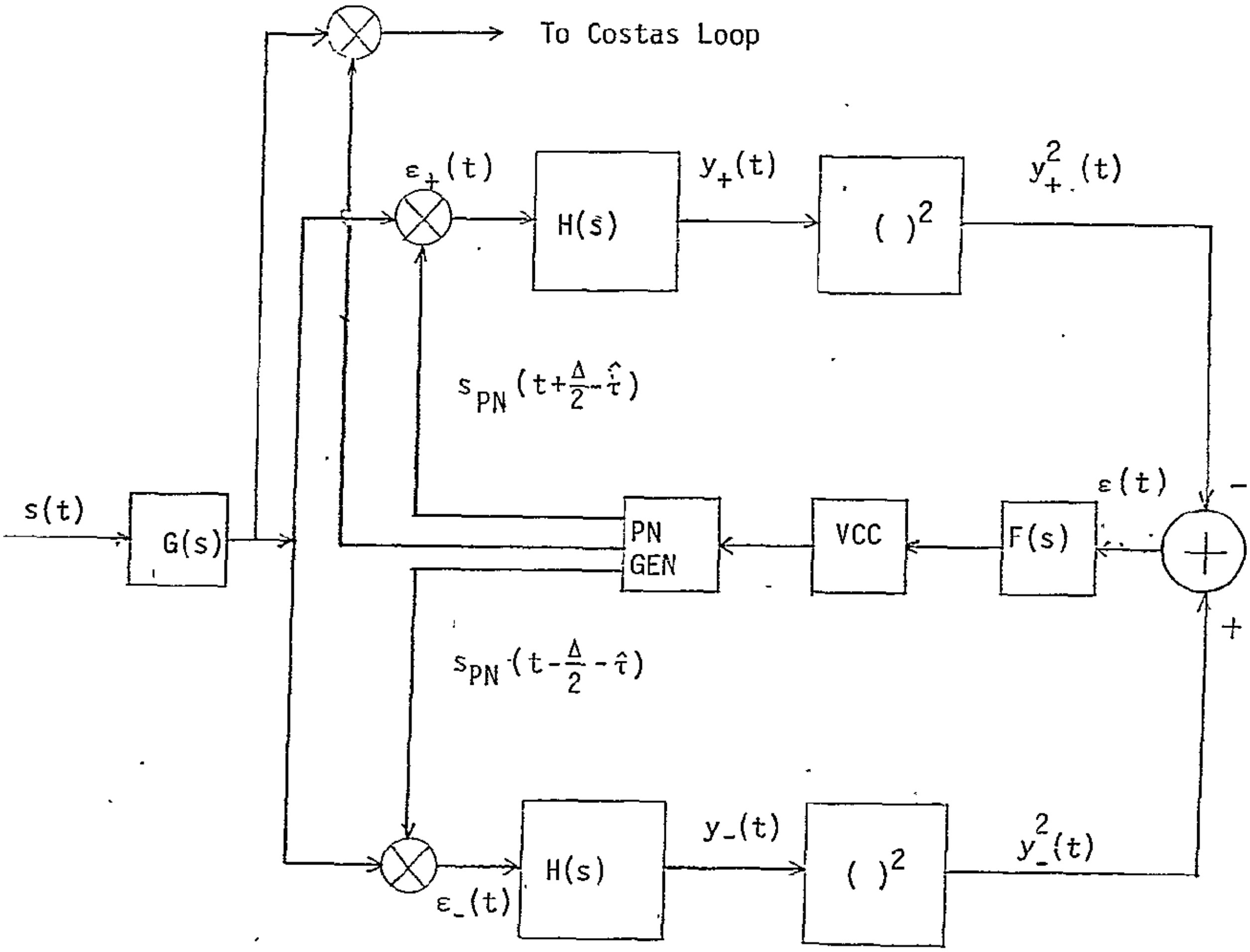

Figure 1 Noncoherent Delay Lock Loop

The prefilter G(s) is a bandpass filter centered at ω_0 with one-sided half-power bandwidth $f_G = 1/\Delta$, where Δ is the PN chip time. The arm-filter H(s) is a bandpass filter centered at ω_0 with one-sided half-power bandwidth $f_H \ll f_G$. The error signal $\varepsilon(t)$ contains the loop S-curve (discriminator characteristic) used to drive the clock. $\hat{\tau}$ is the delay estimate generated by the local PN code generator. In simulation the baseband equivalence of the signal and filters are used. Obviously, s(t) is modulation dependent, and so is the loop S-curve and the on-time correlation function $c(\tau_\ell)$ defined as

$$c(\tau_\ell) = \frac{1}{p\Delta}\int_0^{p\Delta} s_{PN}(t-\tau)m(t-\tau)s_{PN}(t-\hat{\tau})dt \qquad (2)$$

where

$$\tau_\ell = \tau - \hat{\tau} \qquad (3)$$

3. SIMULATION

The PN code in s(t) is of length 1023. The code with feedback taps 2011 (Shuttle Code Assignment 4) is picked arbitrarily. However, in simulation, a code of length 1024, formed by the above 1023 code padded with a zero, is used for the purpose of programming simplicity and computer time saving. It has been verified that both cases yield close results.

Sixteen samples per chip are taken in simulation. The baseband equivalence $G_\ell(s)$ of prefilter G(s) are Chebyshev filters of orders 2 and 4, with 1 dB ripple. The baseband arm-filters are Butterworth filters of order 2. Therefore, the equivalent bandpass filters are of order 4, 8, and 4 respectively. The S-curves are simulated for false lock analysis while the corresponding PN code correlation functions

$c(\tau_\ell)$ are simulated for performance study. The on-time correlation function $c(\tau_\ell)$ is obtained as in Fig. 2 in simulation. In Shuttle S-band modulation, the arm filters have 520 KHz IF two-sided bandwidth. Chip rate is 11.232 Mbps. Therefore

$$f_H\Delta = \frac{1}{2}\ \frac{520\text{x}10^3\ \text{Hz}}{11.232\text{x}10^6\ \text{Hz}} = 0.0231 \qquad (4)$$

Table 1 summarizes the baseband filter parameters used in simulation. The simulations are run with and without modulation. Without modulation $m(t)$ is set to 1. Alternating data, $m(t) = \pm 1$, is used in the case of modulation is present. The data rate in Shuttle S-band is 432 Kbps, so there are 26 chips per bit of data. The data is set to be a square wave sequence. The whole (modulated) PN sequence is assumed periodic of length 1024Δ.

4. NUMERICAL RESULTS

Fig. 3 shows the ideal S-curve and correlation function without the prefilter $G_\ell(s)$. The arm filter bandwidth is assumed to be small ($f_H\Delta$ = 0.0001). These curves are plotted as a comparison for those with prefilter. Figs. 4 and 5 are plotted for $G_\ell(s)$ to be a second order Chebyshev filter with and without modulation. Figs. 6 and 7 are plotted for $G_\ell(s)$ to be a fourth order Chebyshev filter with and without modulation. It can be seen from the S-curves that the lock points experience offsets from $\tau_\ell = 0$. However, the peak of the correlation functions experience approximately similar offset. Therefore, the performance degradation is mainly due to the decrease in the magnitude of the on-time correlation function $c(\tau_\ell)$.

The power degradation for each case is shown in Table 2. It is

ORIGINAL PAGE IS
OF POOR QUALITY

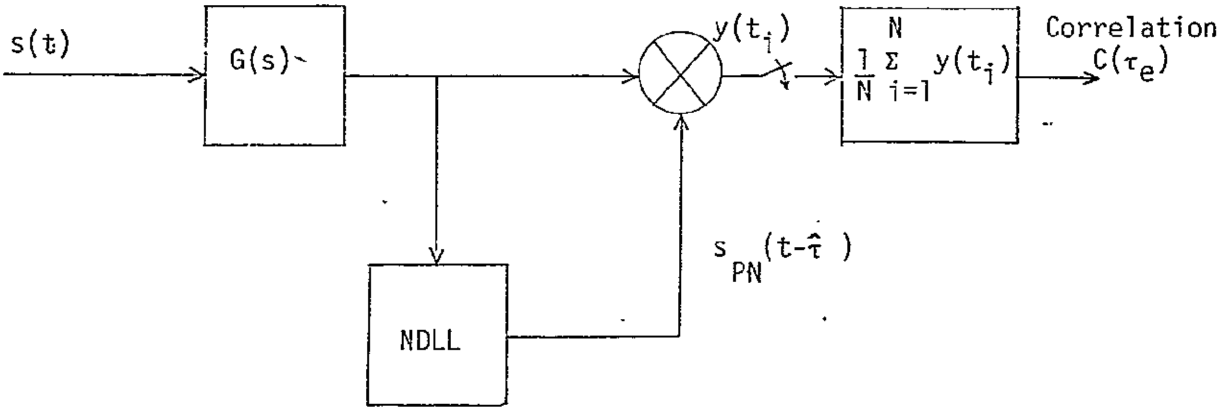

Figure 2. On-Time Correlator in PN Tracking.

Prefilter $G_1(s)$	Arm Filter $H_1(s)$
Chebyshev order 2, 4 $f_G \Delta = 1.0$ 1 dB Ripple	Butterworth order 2 $f_H \Delta = 0.0231$

Table 1 Filter Parameters

ORIGINAL PAGE IS
OF POOR QUALITY

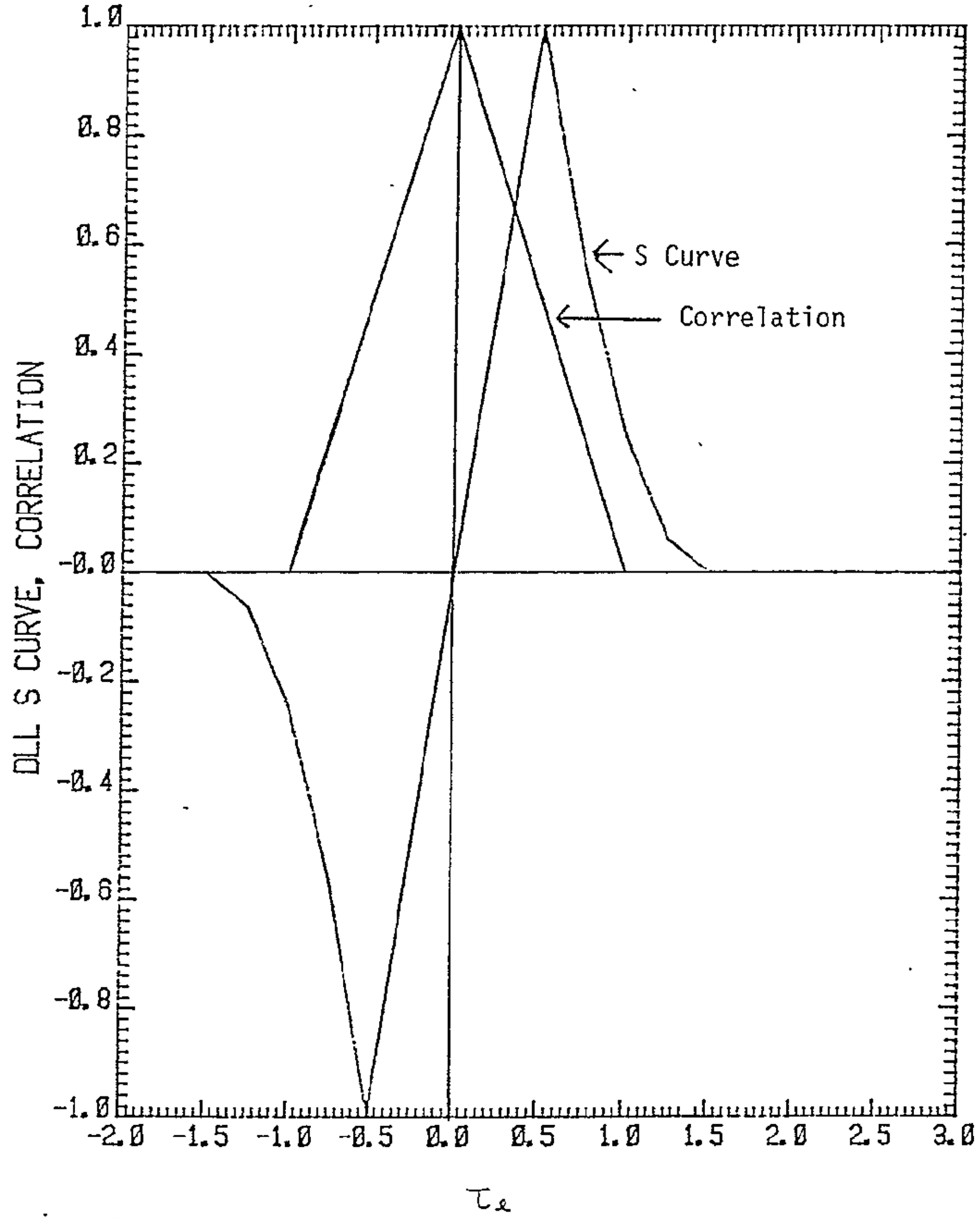

Fig. 3 DLL S-Curve, correlation function without prefilter, $f_H \Delta \ll 1$.

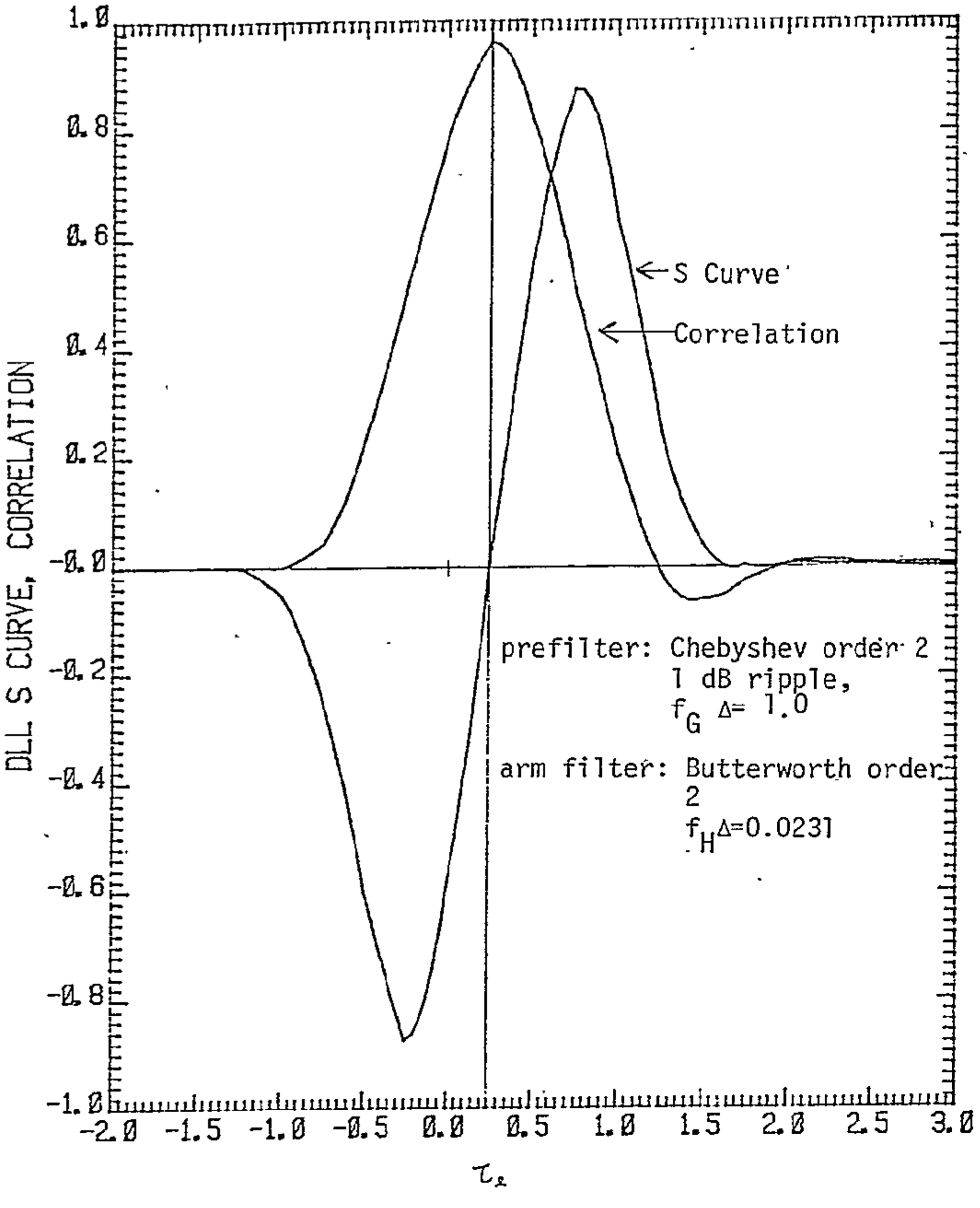

Fig. 4 DLL S-curve, correlation function with no modulation

ORIGINAL PAGE IS
OF POOR QUALITY

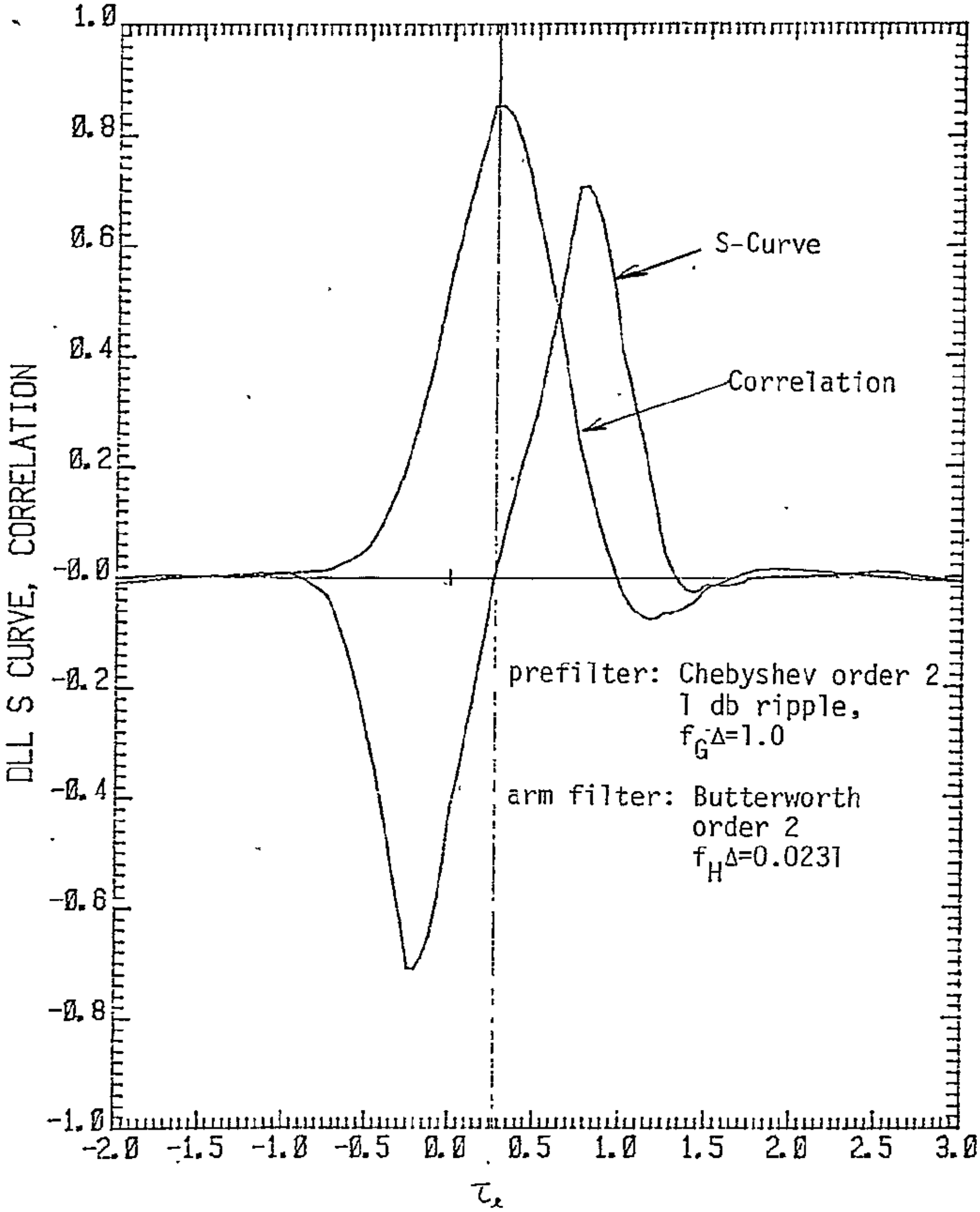

Fig. 5 DLL S-curve, correlation function with modulation

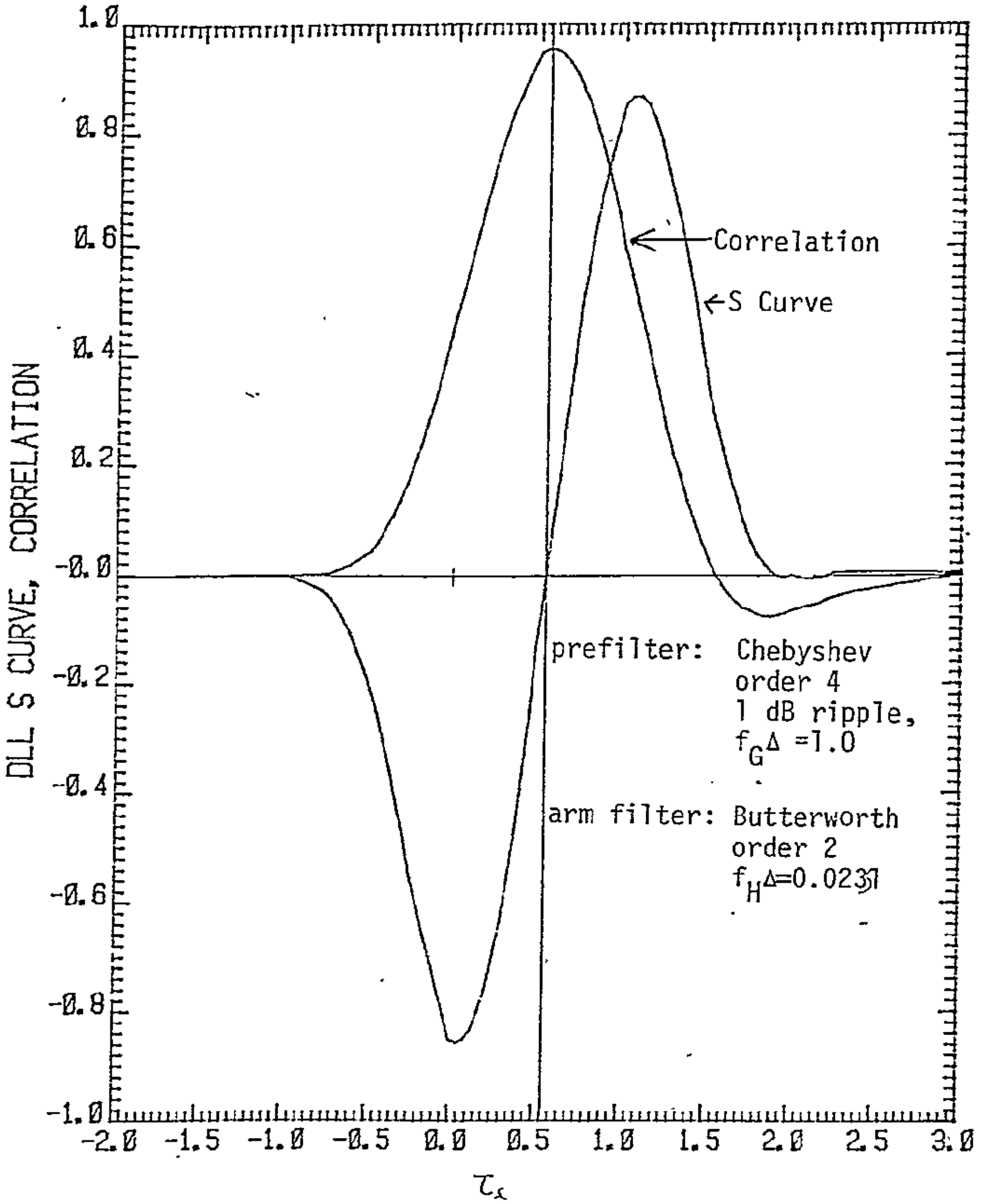

Fig. 6 DLL S-curve, correlation function with no modulation

ORIGINAL PAGE IS
OF POOR QUALITY

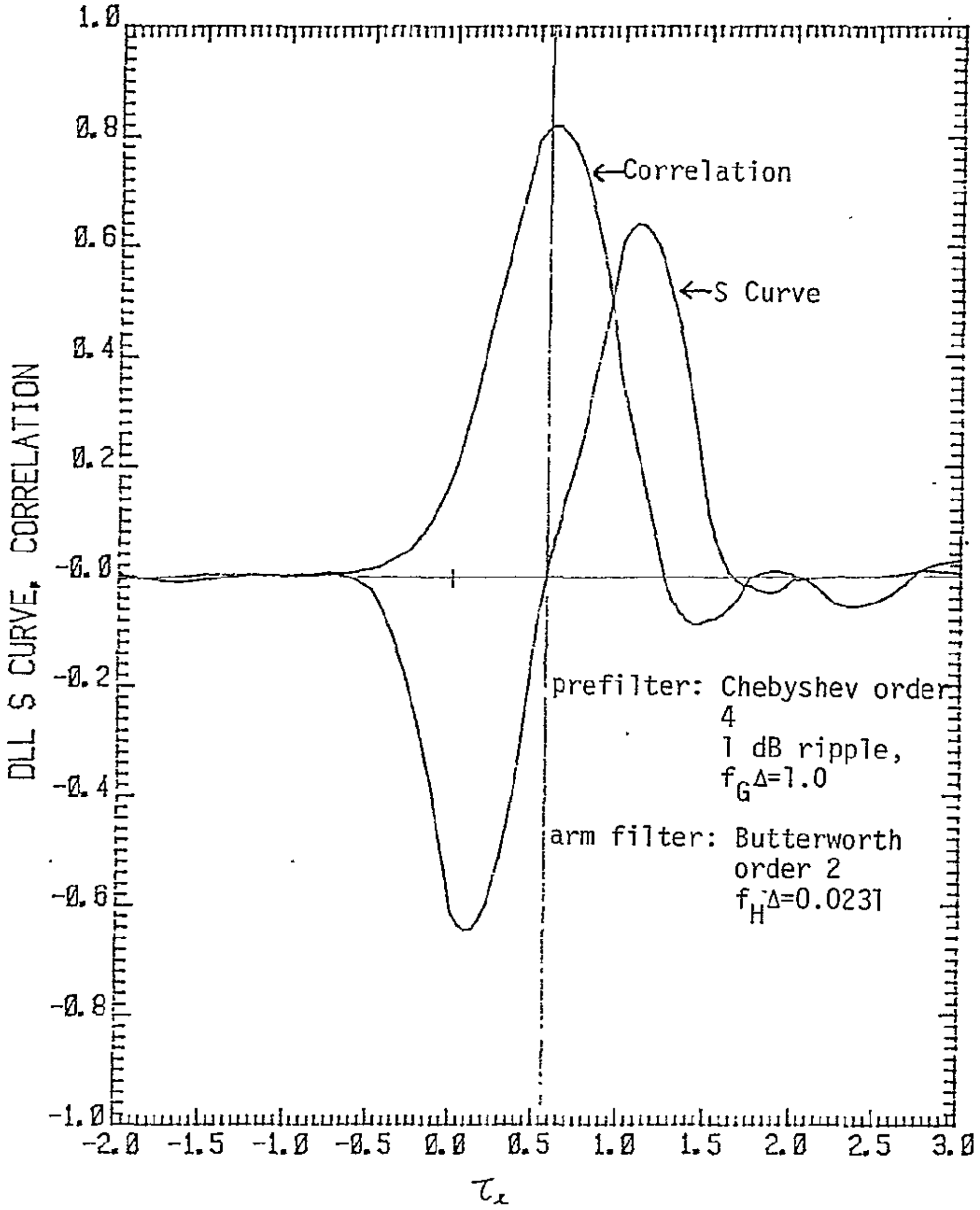

Fig. 7 DLL S-curve, correlation function with modulation

Table 2. Power Degradation with Prefilter Distortion.

CASE	$H_\ell(s)$ BUTTERWORTH $f_H\Delta = 0.0231$	$H_G(s)$ CHEBYSHEV, 1 dB RIPPLE $f_G\Delta = 1.0$	MODULATION	POWER DEGRADATION (dB)
1	2nd ORDER	2nd ORDER	NO	0.036
2			ALTERNATING	1.3
3		4th ORDER	NO	0.36
4			ALTERNATING	1.7

obvious that the major degradation is due to the modulation. The power degradation will depend on specific modulation and therefore time varying.

With the parameters considered here, the power degradation is below 2 dB. Further degradation can be expected if $f_G\Delta$ is less than 1. In the presence of noise and quantization error the loop will operate around the stable lock point. This further offset will cause additional power degradation.

Undesired stable false lock points are shown to exist in the loop S-curve after prefiltering. These lock points cause loop "hangup" during acquisition at high signal-to-noise ratios if the on-time correlation function falls below the lock detection threshold when the timing error lies in the vicinity of these lock points.

The degradation in magnitude of the on-time correlation function gives rise to a signal processing gain loss, i.e., signal power degradation. This degradation, which is modulation dependent, is shown in Table 2. The S-curve and on-time correlation function are provided by two separate subsystems. Any timing offset between the desired lock point and the peak of the on-time correlation function developed in two different multipliers could exist due to differential delay mismatched between channels. This degradation, shown in Table 3, is significant even for an offset of a fraction of a chip time. Therefore, calibration and maintenance of this differential path delay must be maintained.

Table 3. Power Degradation Due to Timing Offset Between S-Curve and Correlation Function.

OFFSET (Δ)	POWER DEGRADATION (dB)			
	CASE 1	CASE 2	CASE 3	CASE 4
0	0.36	1.3	0.36	1.7
1/8	0.72	1.9	0.72	1.9
1/4	1.7	4.0	1.4	3.1
3/8	3.3	6.9	3.1	6.2
1/2	5.7	13.2	5.5	11.1

Note: Parameters in each case correspond to the same case in Table 2.

2.5 PREDICTED CRN DEGRADATION TO BER ON SHUTTLE/TDRSS S-BAND RETURN LINK

Table 1 gives LinCsim's predictions of the CNR degradation to BER due to RFI for both modes of the Shuttle/TDRSS S-band return link. The RFI environments treated are Models C, D, E, and F of [1]. The LinCsim program computes results assuming an interleaver. Shuttle will not have an interleaver. The increased degradation due to that fact is estimated from the results with interleaver and from Harris Corporation hardware results, the references for which are given in Table 1. Mode 2 is much more affected by the interleaver absence thatn mode 1 is.

REFERENCE

1. John J. Schwartz, "Simplified Radio Frequency Interference (RFI) for the TDRSS S-band Return Link Evaluation," GSFC, MD, 5 November 1981.

Table 1. Predicted CNR Degradation for Shuttle/TDRSS S-Band Return Link.

	With Interleaver		Without Interleaver*	
	Mode 1	Mode 2	Mode 1	Mode 2
Model C - 0°	1.72 dB	1.95 dB	2.6	4.0-7.0
1.5°	.59	.71	1.0	1.4-2.5
4°	.16	.20	.2	.3-.7
Model D - 0°	1.62	1.72	2.4	3.5
1.5°	.45	.47	.8	1.0
4°	.10	.11	.1	.2
Model E - 0°	.41	.45	.8	.9-1.6
1.5°	.10	.13	.1	.2-.4
4°	0	0	0	.1-.2
Model F - 0°	.51	.54	.9	1.4
1.5°	.07	.08	.1	.2
4°	0	0	0	.1

---

*Effect of interleaver absence is estimated from results given in "RFI Test Study Final Report " by Harris Corp., Government Systems Group Communications Systems, Melbourne, FL, 29 April 1980.

Where a range of degradation values is shown, the minimum is estimated from the report just cited and the maximum is estimated from "RFI Test Study Second Interim Report" by Harris Corporation, Government Systems Group Communications Systems, Melbourne, FL, 26 February 1980.

2.6 RFI EFFECT ON ACQUISITION OF SHUTTLE/TDRSS S-BAND RETURN LINK

1. Introduction

We would like to be able to say how much longer or shorter acquisition of the Shuttle/TDRSS S-Band return link takes in the presence of RFI. Unfortunately, the theory of noisy acquisition of loops is almost nonexistent. Fortunately, even in the presence of RFI the SNR at input to the S-band Shuttle Demodulator/Bit Synchronizer is greater than the minimum required for normal acquisition, as will be shown through numerical results in Section 3. We proceed in Section 2 to obtain an expression for SNR.

2. SNR in the Carrier Loop Bandwidth

The overall link diagram is shown in Fig. 1. We derive expressions for the signal at input to the demodulator and then calculate SNR in the carrier loop bandwidth.

The signal + noise + RFI before the nonlinearity is

$$\begin{aligned} y_2(t) &= \sqrt{2}[\sqrt{P}\, d_1(t) + n_{u_1}(t) + w_1(t)]\cos(\omega t+\psi_1) \\ &\quad - \sqrt{2}\,[n_{u_2}(t)+w_2(t)]\sin(\omega t+\psi_1) \end{aligned} \tag{1}$$

where the signal is BPSK and $n_{u_i}(t)$ and $w_i(t)$ are quadrature components of the uplink noise and RFI, respectively. $y_2(t)$ can also be written as

$$y_2(t) = \sqrt{2}\, r(t)\cos\left(\omega t + \psi_1 + \tan^{-1}\frac{B(t)}{A(t)}\right) \tag{2}$$

where

$$\begin{aligned} A(t) &= \sqrt{P}d_1(t) + n_{u_1}(t) + w_1(t) \\ B(t) &= n_{u_2}(t) + w_2(t) \\ r(t) &= \sqrt{A^2(t)+B^2(t)} \end{aligned} \tag{3}$$

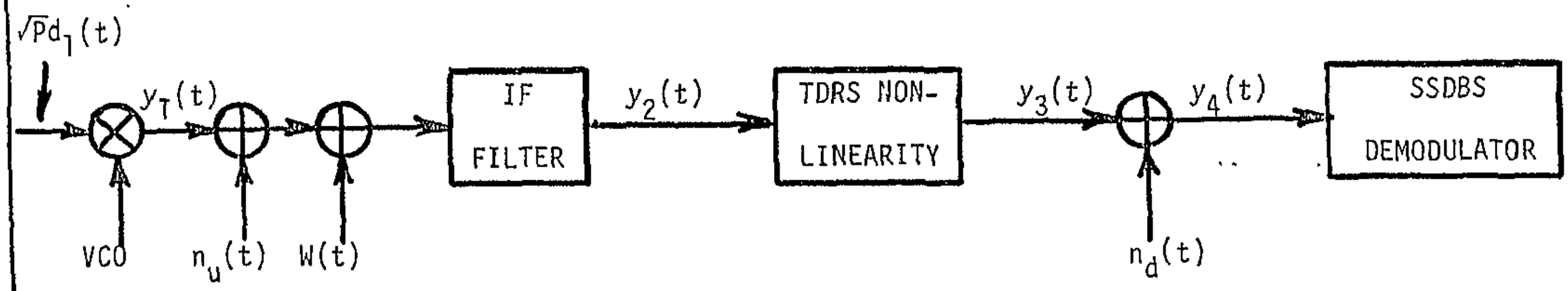

Figure 1. Link Diagram.

After the nonlinearity, because of the AM-AM ($f(r)$) and AM-PM ($g(r)$) conversions, we can write $y_3(t)$ as

$$\begin{aligned} y_3(t) &= \sqrt{2} f(r(t)) \cos\left(\omega t + \psi_1 + \tan^{-1}\frac{B(t)}{A(t)} + g(r(t))\right) \\ &= \sqrt{2}\,[h_1(r)\cdot A - h_2(r)\cdot B]\cos(\omega t+\psi_1) \\ &\qquad - \sqrt{2}[h_2(r)\cdot A + h_1(r)\cdot B]\sin(\omega t+\psi_1) \end{aligned} \tag{4}$$

where

$$\begin{aligned} h_1(r) &= f(r)\cos(g(r))/r \\ h_2(r) &= f(r)\sin(g(r))/r \end{aligned} \tag{5}$$

At this point, downlink noise must be added. But since the amount of downlink thermal noise is small, it is neglected from here on. Its inclusion is straightforward and could be implemented if necessary. $y_3(t)$ can be further separated into signal and noise components

$$y_{3S}(t) = \sqrt{2}[h_1\sqrt{P}d_1(t)]\cos(\omega t+\psi_1) - \sqrt{2}[h_2\sqrt{P}d_1(t)]\sin(\omega t+\psi_1)$$

and

$$\begin{aligned} y_{3N}(t) &= \sqrt{2}[h_1(n_{u_1}+w_1) - h_2(n_{u_2}+w_2)]\cos(\omega t+\psi_1) \\ &\qquad - \sqrt{2}[h_1(n_{u_2}+w_2)+h_2(n_{u_1}+w_1)]\sin(\omega t+\psi_1) \end{aligned} \tag{6}$$

where

$$y_3(t) = y_{3S}(t) + y_{3N}(t) \tag{7}$$

Expressions for signal and noise power are given by

$$P_S = E\{(h_1\sqrt{P}d_1)^2 + (h_2\sqrt{P}d_1)^2\}$$

$$= P\ E\{(\frac{f(r)}{r})^2\ [(n_{u_1}+w_1)^2+(n_{u_2}+w_2)^2]\} \qquad (9)$$

where P_s is signal power and P_n is noise power.

The SNR in the carrier loop bandwidth can be calculated as follows. Conditioned on all the RFI processes and on the no-RFI condition, we compute a set of P_{s_i} and P_{n_i}. Then the average signal and noise power can be obtained simply by weighting the P_{s_i} and P_{n_i} by the corresponding duty cycles and summing. This averaging can be justified by the fact that the demodulator loop bandwidth (28.8 KHz) is small compared to the inverse of the RFI pulse duration (3.5 μsec) so that RFI is effectively spread in time. Thus, the average SNR can be obtained as

$$\text{SNR} = \frac{\sum_i P_{s_i}}{\sum_i P_{n_i}} \qquad (10)$$

where the noise power is that which enters the carrier loop bandwidth only.

3. Numerical Results

Numerical calculation has been performed of the SNR degradation due to RFI for both mode 1 and mode 2. The RFI environment used Model C from [1] , which is the worst environment LinCom has for Shuttle. The results are given in Table 1. The degradation is about 1.2 dB for the given RFI environment.

From [2], the minimum SNR required for normal demodulator acquisition is

Table 1. Average SNR in Carrier Loop Bandwidth.

	3 dB CLIPPER		9 dB CLIPPER	
	NO RFI	RFI	NO RFI	RFI
MODE 1	14.1 dB	12.9 dB	13.2 dB	10.7 dB
MODE 2	17.1	15.9	16.2	13.6

9.70 dB	for Mode 1
12.71 dB	for Mode 2

With the given RFI environment, the SNR in the demodulator is still well above the minimum required. Thus we expect that even under severe RFI environments, the acquisition process will be little affected.

REFERENCES

1. John J. Schwartz, "Simplified Radio Frequency Interference (RFI) for the TDRSS S-band Return Link Evaluation," GSFC, MD, 5 November 1981.
2. "S-Band Shuttle Demodulator/Bit Synchronizer," Motorola Government Electronics Division, Scottsdale, Arizona, June 1978.

3. ASSESSMENT OF ESTL SIMULATOR AND TDRSS FLIGHT HARDWARE CHARACTERISTICS

3.1 Introduction

This chapter documents the work accomplished under Task #3, which requires assessment of the differences between the ESTL simulation hardware and the TDRSS system design. The work dealt with ESTL tests involving simulated radio-frequency interference (RFI). Section 3.2 gives the method by which the RFI environments provided to JSC and LinCom on December 8, 1981, were approximated by the RFI Test Generator. This method is also applicable to future reprogrammings of the RFI Test Generator. Attachment 3 of this final report documents one of the sets of predictions made by LinCsim of the RFI degradation to bit error rate seen by the ESTL equipment. Section 3.3 presents an attempt to explain the discrepancy between prediction and observation.

3.2 PROGRAMMING OF RFI TEST GENERATOR

1. Introduction

On December 8, 1981, a new set of RFI environments was provided to JSC and LinCom [1]. This report shows how these environments can be approximated by the RFI test generator (RTG) and furnishes all the information required to reprogram the RTG for the new environments.

Section 2 gives some background information about the restrictions on the RFI modeling in the RTG. Section 3 contains tables of data which must be stored in the RTG's PROMS and explains how these tables are to be used. Section 4 compares the modeling performed here with the PROM data in [1].

2. Modeling of RFI Environments in the RTG

The RTG uses two kinds of stored tables to define one RFI environment.

The first table defines the probability P_p that a given interval of duration τ (the RFI pulse duration) contains an RFI pulse (either noise or CW). In the RTG manual it is called the Probability PROM table. This table contains one value for CW pulses and another for noise pulses for each RFI environment and each pulse duration. The relationship between table entry C and pulse probability P_p is

$$C = 128 P_p$$

or, since there are τ^{-1} intervals per second, the table entry is related to the pulse rate $PPS = P_p/\tau$ by

$$C = 128 \cdot PPS \cdot \tau$$

C must be an integer in [0,127], hence the quantization of the pulse rate is quite coarse. Table 1 lists the minimum increment of PPS for various values of τ.

The second kind of table stored in the RTG defines the relative frequency of the various power levels given that a pulse is generated. It is called the amplitude PROM table in the RTG manual.

The modeling of the RFI environment consists of the determination of the entries for both types of tables. In order to obtain accurate results it is best to start out with the determination of the table entry C. A problem which arises in this process is that PPS will take on a different value for each pulse duration τ. This problem was dealt with here by modifying the pulse power distribution curves at the low power levels (20 dBW and less) to result in very similar values of PPS for all values of τ. The result is, however, that the pulse rate for the lowest power level differs in some cases substantially from the levels suggested by the environments in [1]. This difference is only substantial on a relative scale, however. The maximum error is 1.6 Kpulses/sec and from simulations it was determined that this error has a negligible effect on the expected link performance. The second step in the modeling is then the quantization of the modified pulse power distribution curves. The resulting approximation to the original RFI environments are shown in Figures 1 to 8. The modification of the environments is hardly noticeable except for the two nonzero CW environments. The fit above 20 dBW is always very good.

3. Data Required for RTG Programming

3.1 Probability PROM Table

The probability PROM Table is stored in three PROM chips of the type HM-7603: One for noise pulses and two identical ones for CW pulses. The noise chip should be programmed according to Table 2 and the two CW chips according to Table 3.

The amplitude PROM tables require a total of 32 PROM chips of the

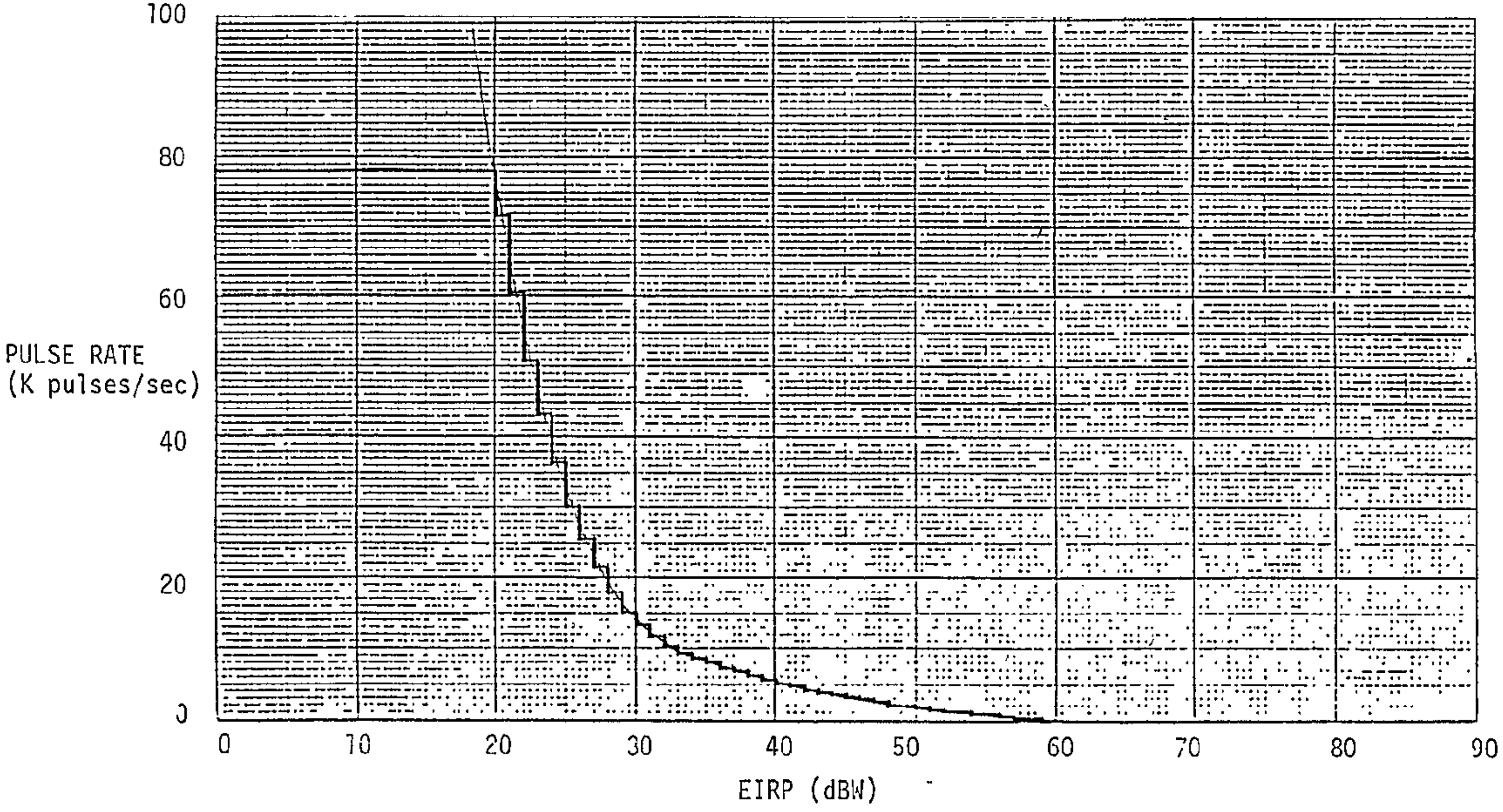

Figure 1. Approximation for Environment 1 (EH,Noise).

ORIGINAL PAGE IS
OF POOR QUALITY

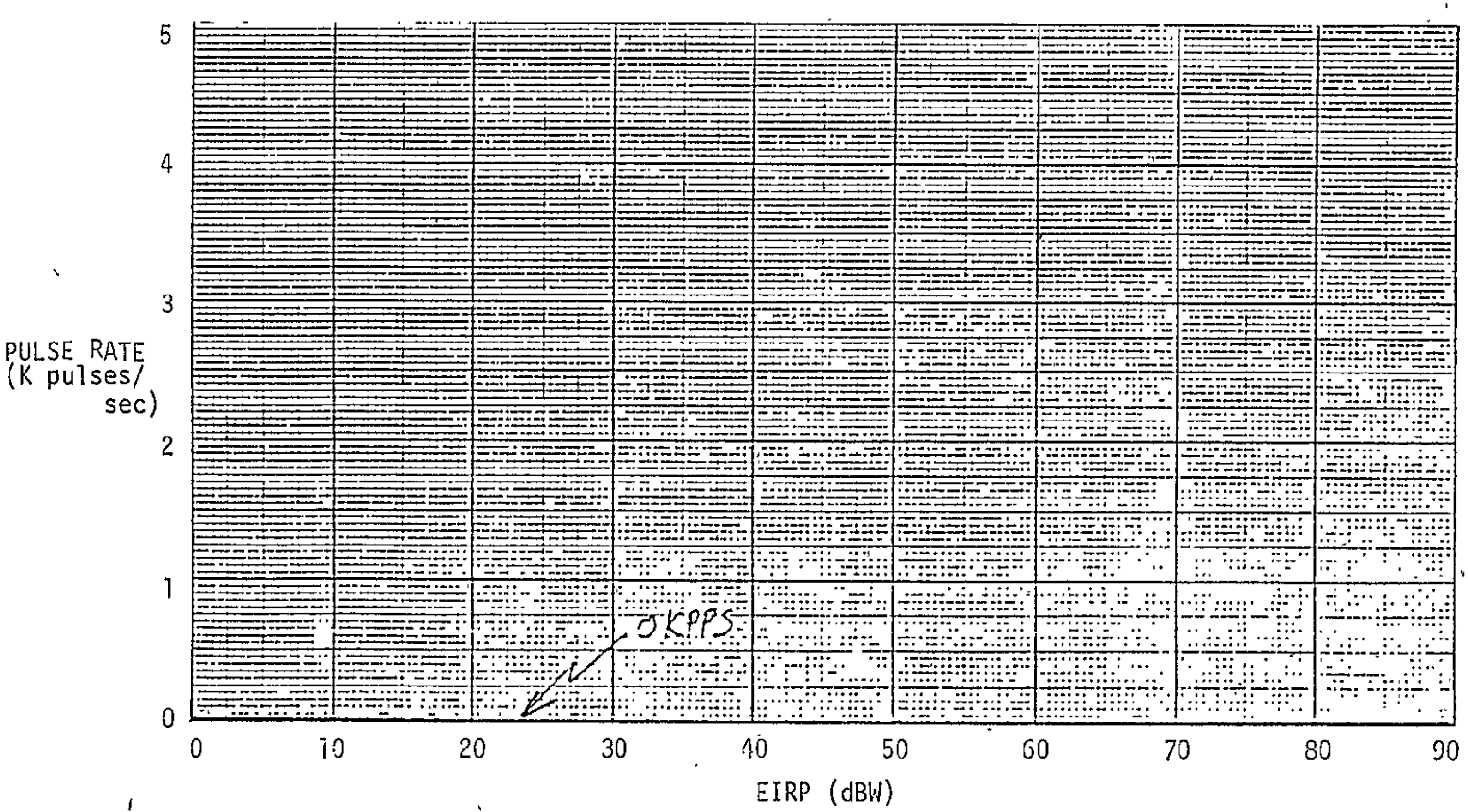

Figure 2. Approximation for Environment 1 (EH, CW).

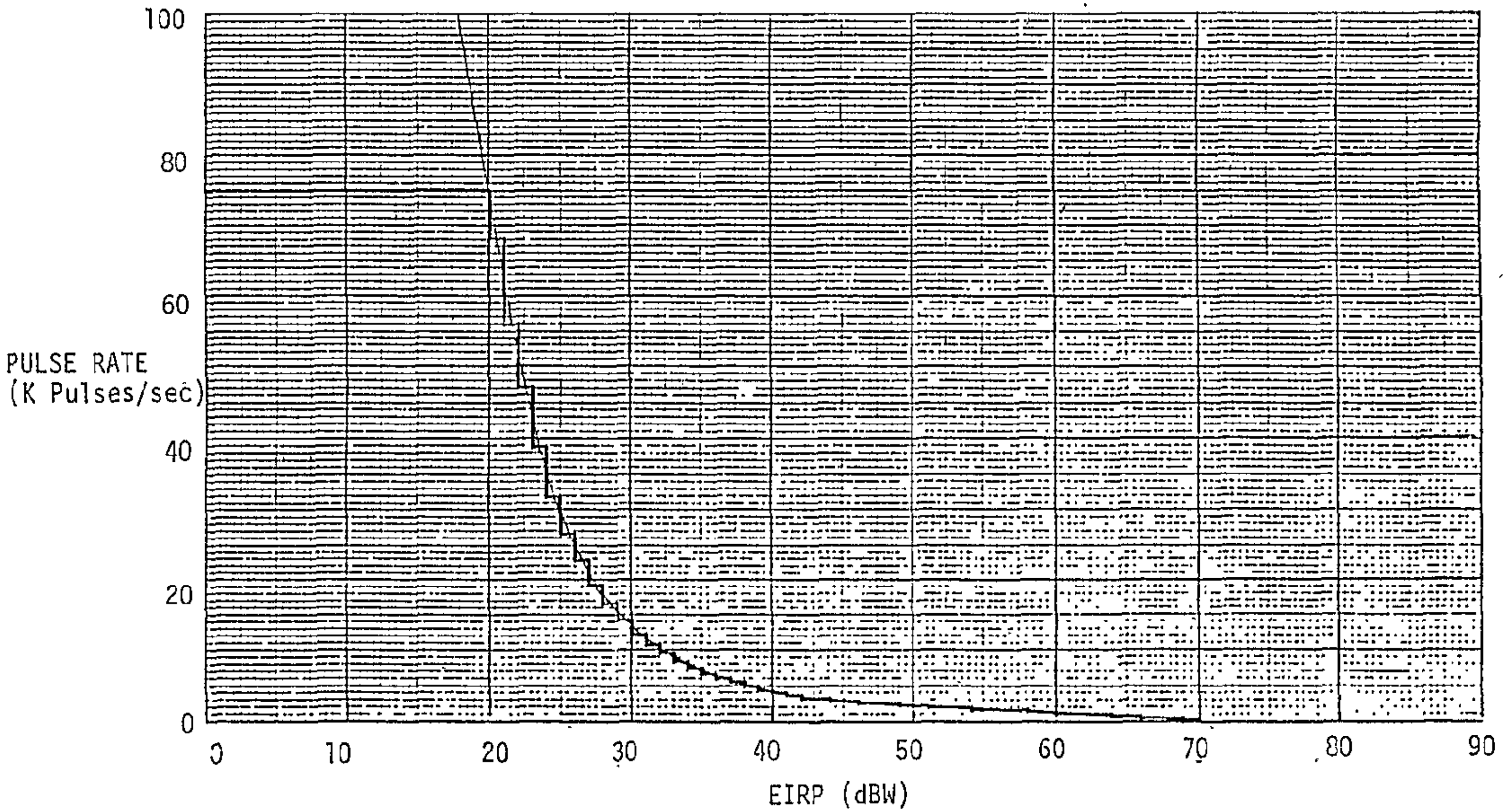

Figure 3. Approximation for Environment 2 (EL, Noise).

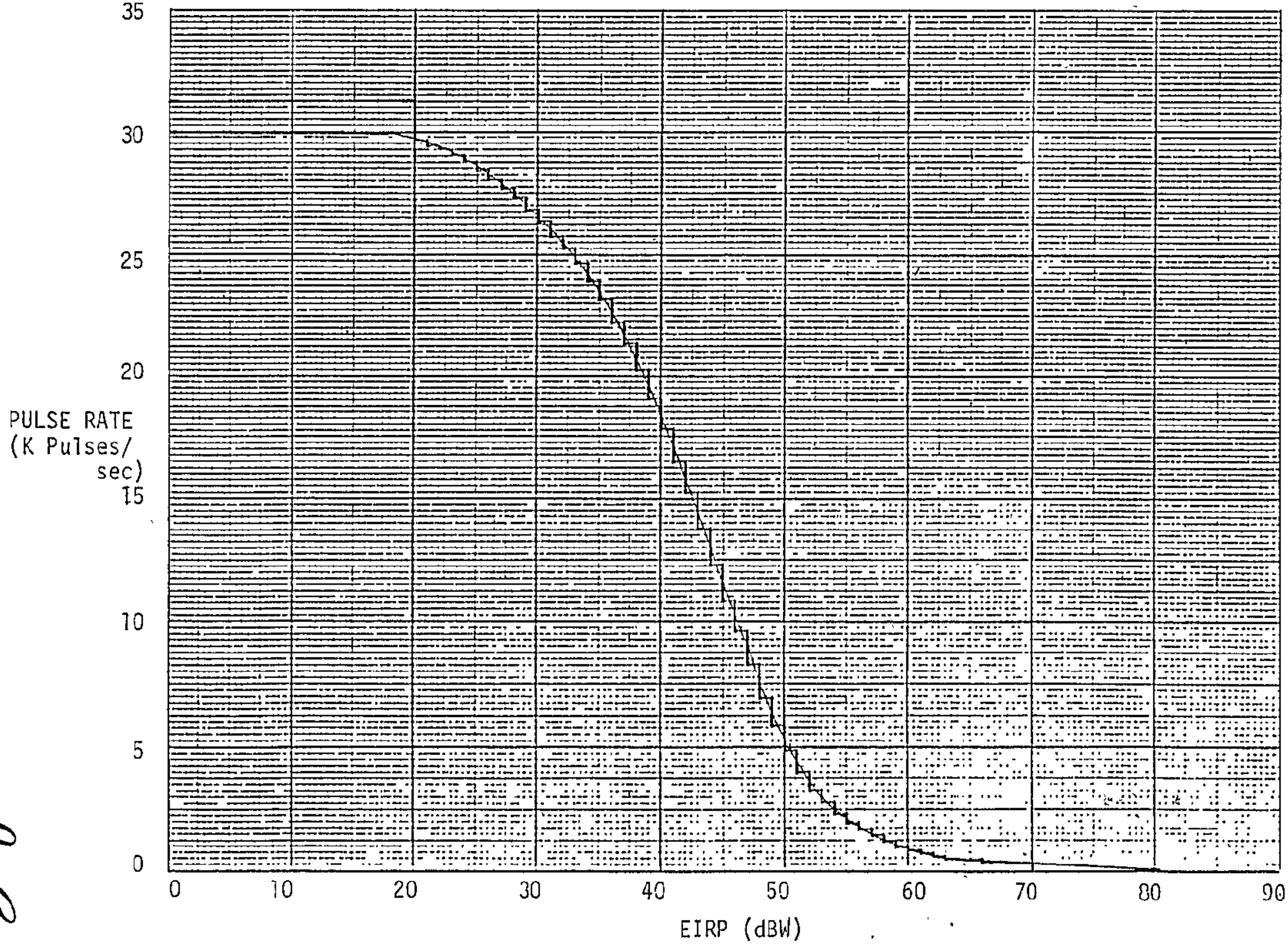

Figure 4. Approximation for Environment 2 (EL,CW).

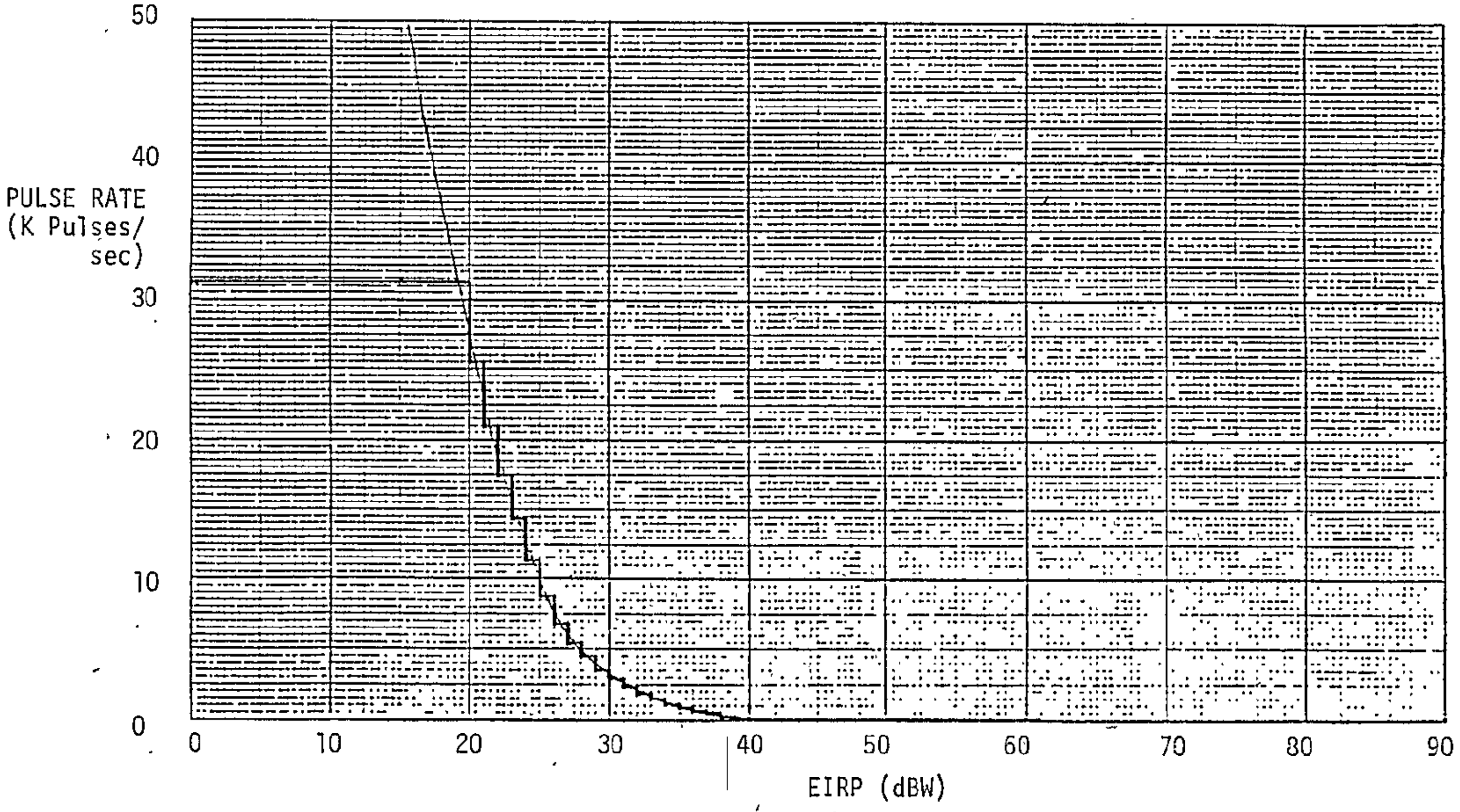

Figure 5. Approximation for Environment 3 (WH, Noise).

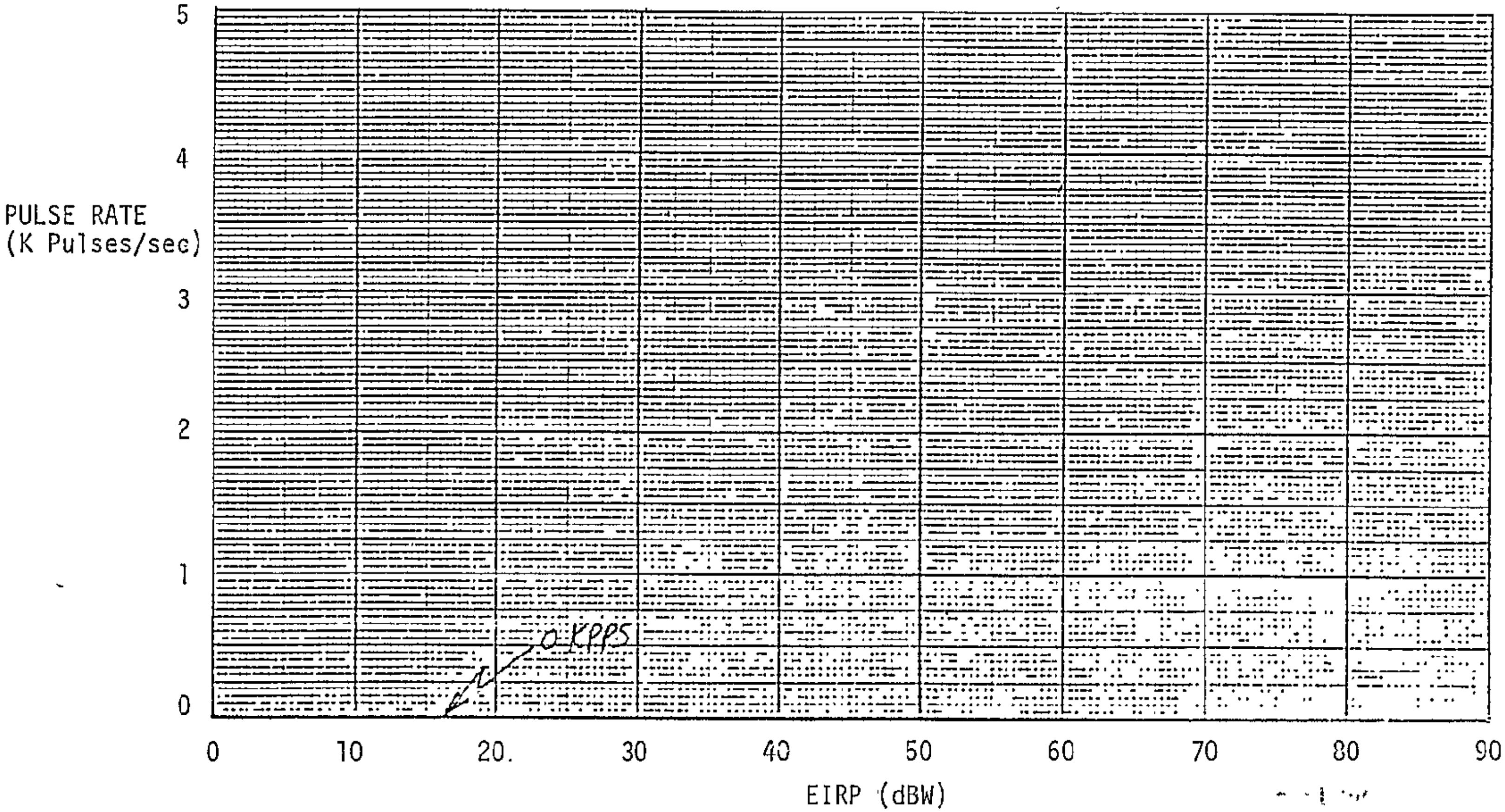

Figure 6. Approximation for Environment 3 (WH, CW).

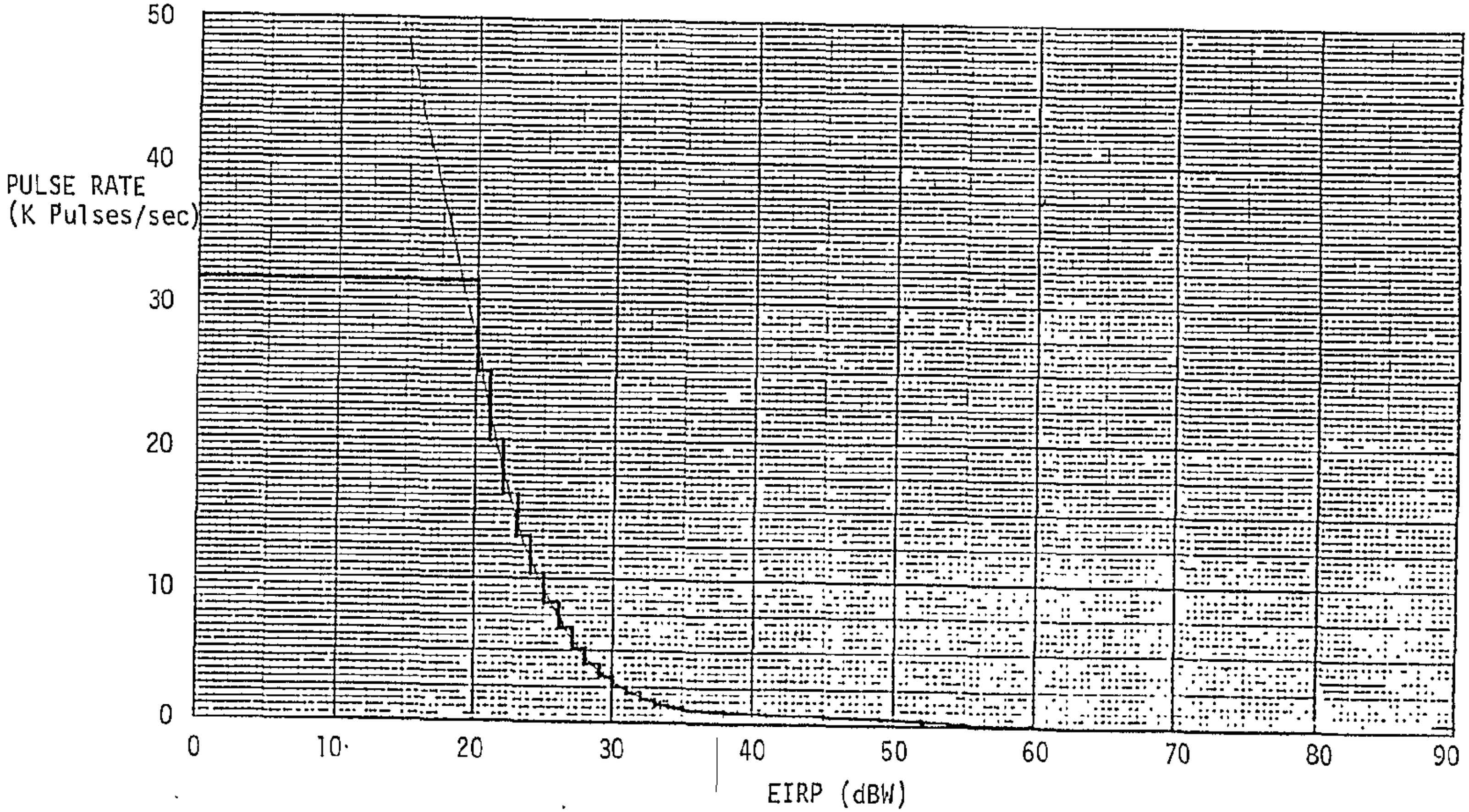

Figure 7. Approximation for Environment 4 (WL, Noise).

ORIGINAL PAGE IS
OF POOR QUALITY

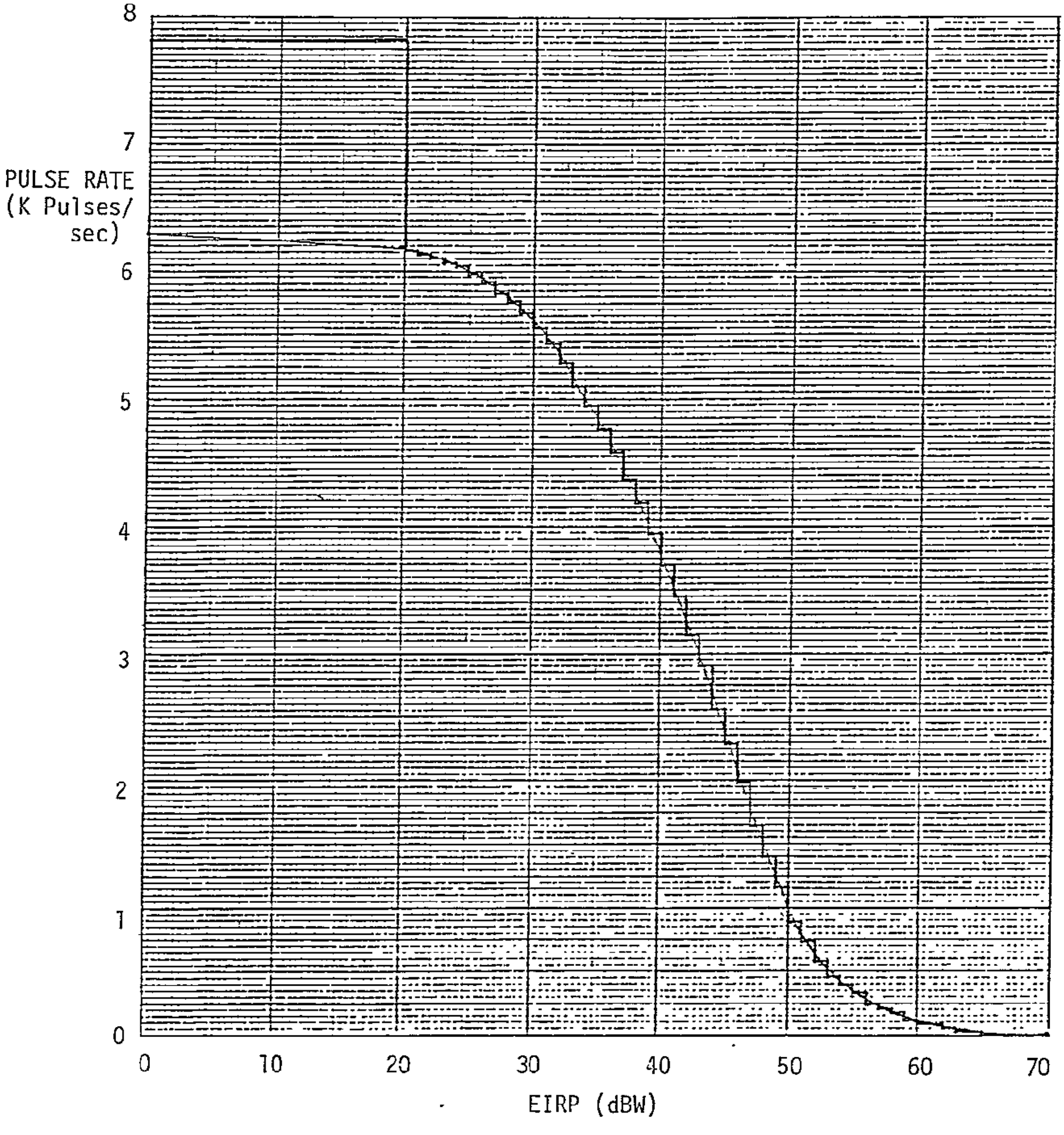

Figure 8. Approximation for Environment 4 (WL, CW).

Table 1. Increment of Pulse Rate.

PULSE DURATION (μ sec)	INCREMENT ON PPS (K Pulses/sec)
2	3.9
3	2.6
4	2.0
5	1.6
6	1.3

ADDRESS		CONTENTS	
DEC	HEX	DEC	HEX
0	00	255	FF
1	01	255	FF
2	02	255	FF
3	03	255	FF
4	04	255	FF
5	05	255	FF
6	06	255	FF
7	07	255	FF
8	08	24	18
9	09	58	3A
10	0A	60	3C
11	0B	24	18
12	0C	20	14
13	0D	48	30
14	0E	50	32
15	0F	20	14
16	10	16	10
17	11	38	26
18	12	40	28
19	13	16	10
20	14	12	0C
21	15	29	1D
22	16	30	1E
23	17	12	0C
24	18	8	08
25	19	19	13
26	1A	20	14
27	1B	8	08
28	1C	255	FF
29	1D	255	FF
30	1E	255	FF
31	1F	255	FF

Table 2. Contents of Probability PROM for Noise.

ADDRESS		CONTENTS	
DEC	HEX	DEC	HEX
0	00	255	FF
1	01	255	FF
2	02	255	FF
3	03	255	FF
4	04	255	FF
5	05	255	FF
6	06	255	FF
7	07	255	FF
8	08	0	00
9	09	24	18
10	0A	0	00
11	0B	6	06
12	0C	0	00
13	0D	20	14
14	0E	0	00
15	0F	5	05
16	10	0	00
17	11	16	10
18	12	0	00
19	13	4	04
20	14	0	00
21	15	12	0C
22	16	0	00
23	17	3	03
24	18	0	00
25	19	8	08
26	1A	0	00
27	1B	2	02
28	1C	255	FF
29	1D	255	FF
30	1E	255	FF
31	1F	255	FF

Table 3. Contents of Probability PROMs for CW.

type HM-17611. These are 256x4 bit memories. Since the numbers to be stored are between 0 and 50 (HEX 32) there are two chips required to store one table: one contains the most significant (HEX) digit (MSD) and the other the least significant (HEX) digit (LSD). Each of the four environments requires one table for noise pulses and one for CW pulses and each table has a duplicate, resulting in

$$\underset{\text{(environments)}}{4} \times \underset{\text{(noise/CW)}}{2} \times \underset{\text{(duplicate)}}{2} \times \underset{\text{(chips/table)}}{2} = 32$$

chips. The memory contents of these chips is listed in Tables 4 through 11. As pointed out, the MSD of the HEX number goes into one chip (suffix 1) and the LSD goes into another (suffix 2) and a duplicate is to be programmed for each.

4. Comparison with Previous PROM Data

The PROM tables given in [1] for the same RFI environments differ in two aspects from those presented in this report:

(1) The values in the probability PROM tables are approximately one-half of the values given here.

(2) The values in the amplitude PROM tables are approximately 20 units larger than the values shown here.

In both cases the source of the difference could be traced to the poor documentation for the RTG. The values given here supersede the ones previously documented in [1].

Reference

[1] TDRSS/WEC-81-062-GJ, Letter to Melvin Kapell from Gene Jones, December 8, 1981.

3.3 COMPARISON OF ESTL RFI TEST RESULTS AND LinCsim PREDICTIONS

1. Introduction

In early May 1982 tests were performed at ESTL of Johnson Space Center to measure the performance of the simulated S-band Shuttle/TDRSS return links in the presence of simulated pulsed radio-frequency interference [1]. The performance measures obtained which are of concern in this report are symbol error rate (SER, at matched-filter output) and bit error rate (BER, at Viterbi decoder output). LinCsim was used to obtain predictions of the performance to compare with the measurement. The BER comparison is bad. The SER comparison is good for a certain range of Shuttle-to-TDRSS CNR's but unfortunately not for the range of interest. In this report we attempt to explain the discrepancy.

The sections that follow are these. In Section 2 some actual and predicted results are compared. In Section 3 analysis in support of our predictions is summarized, which assumes that the receiver losses are the same with and without RFI. In Section 4 the symbol synchronizer performance with and without RFI is studied. Finally, in Section 5 some conclusions are presented.

2. Comparison of Hardware Results and Predictions

Since predicted BER does not compare well with measured BER, in this report a more basic comparison is made, that of SER. Measured and predicted values of SER as a function of delta CNR are presented in Figures 1 and 2. Link characteristics are listed in Table 1. Figure 2 is a continuation upward of Figure 1. As a reference the link performance without RFI is also shown. The delta CNR is relative to the CNR at which SER = 10^{-2} without RFI. The RFI environment used in obtaining these results is the most severe of those used in the ESTL

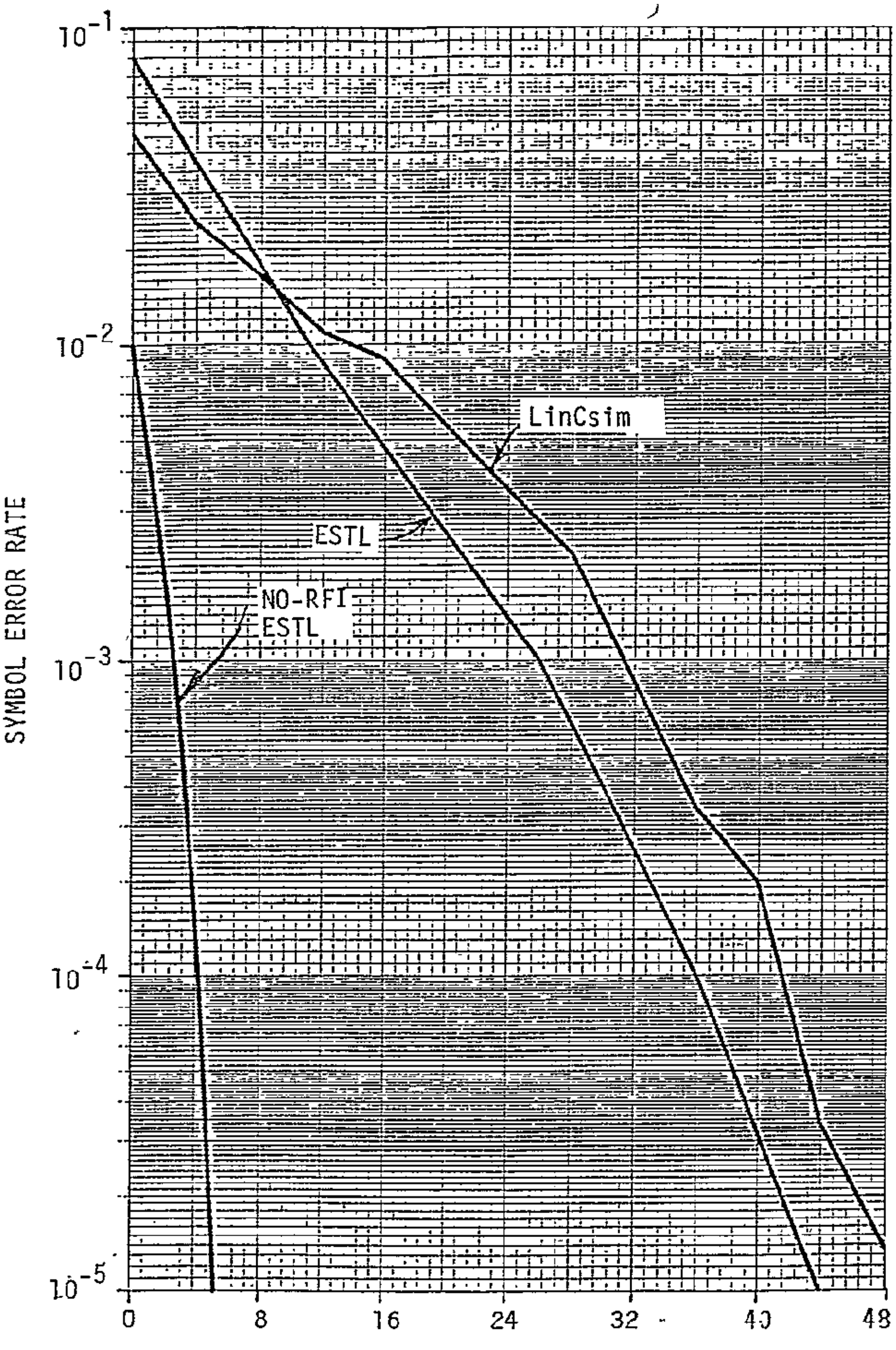

Figure 1. Comparison of ESTL Results with LinCsim Prediction--Symbol Error Rate as a Function of ΔCNR.

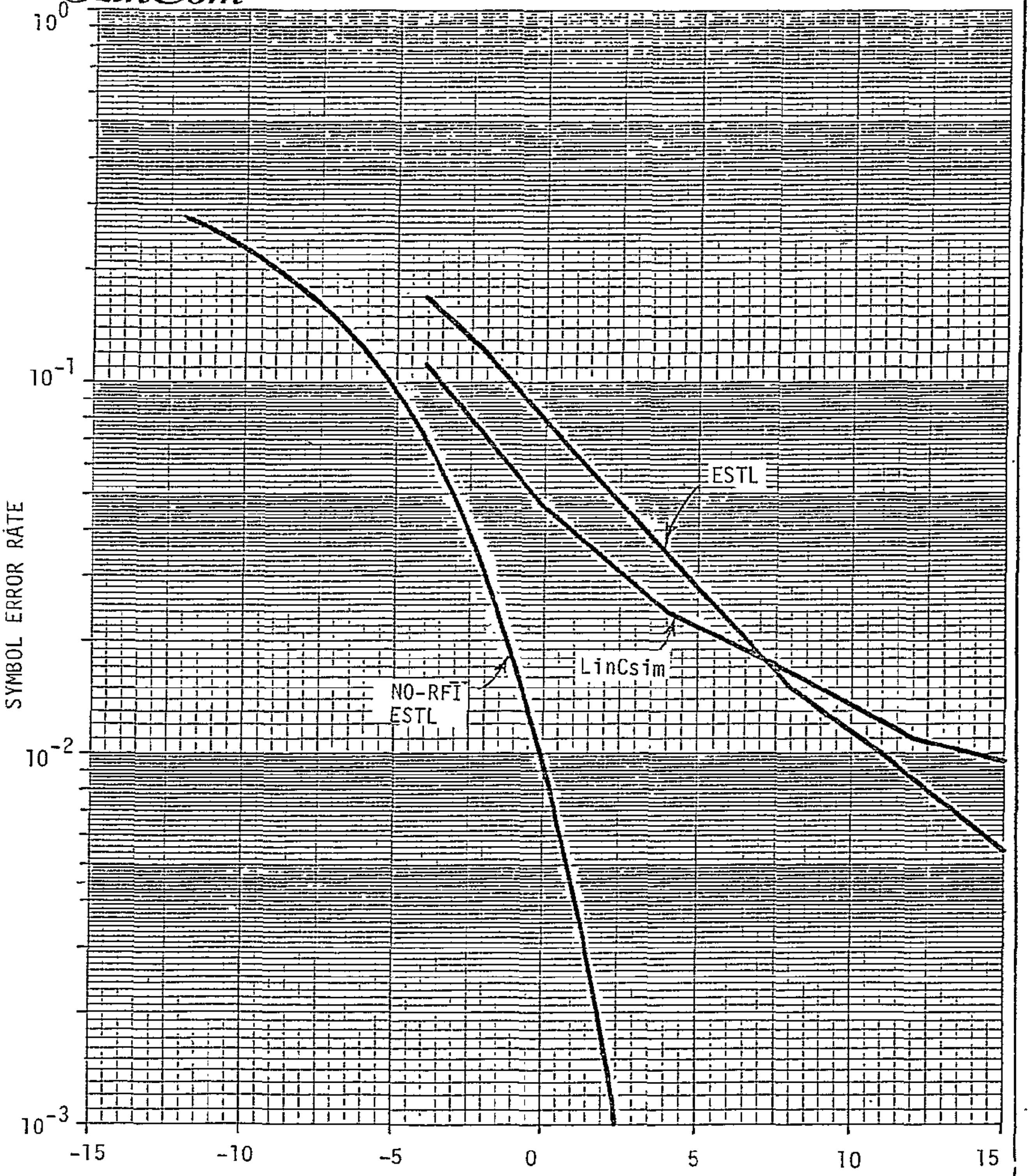

Figure 2. More Comparison of ESTL Results with LinCsim Prediction--Symbol Error Rate as a Function of ΔCNR.

C'2

Table 1. Link Characteristics.

Shuttle mode 1

Equivalent Thermal Noise EIRP 27.6 dBW in 20 MHz

One-sided IF bandwidth of TDRS input filter = 17.5 MHz

TDRS nonlinearity = clipper followed by TWTA

Clipper characteristics:

- 1-dB compression point 6 dB above operating point
- output power 3 dB below saturation at 1-dB compression point
- AM/PM distortion 1.2 deg/dB for inputs > 1-dB compression point -.3 dB

TWTA characteristics:

- 18.5 dB input backoff
- maximum AM/PM distortion 5.5 deg/dB

tests and includes both noise- and continuous-wave(CW)-type RFI. No antenna off-pointing is assumed. RFI pulse duration is 5 μsec. In our predictions, channel losses (not including the effect of the TDRS nonlinearity) are assumed to be the same with RFI as without RFI and the same for all CNR's.

It can be seen in Figures 1 and 2 that for SER's less than .015 the predicted SER is greater than the measured SER, as expected since the LinCsim program was written to be slightly conservative when it couldn't be more accurate. However, for SER's greater than .015 the prediction is optimistic. Unfortunately, this is the region of interest, since at least for a Gaussian channel an SER of about .10 corresponds to a BER of 10^{-5} with the rate-1/3 code. Our prediction is that an SER of .10 occurs with 2.4 dB less CNR than the measured results indicate.

The desire to explain this discrepancy led us to perform the analyses described in the next two sections.

3. Analysis of Predictions

We have elsewhere performed an analysis of our predictions of the RFI effect on BER which supports the reasonableness of them. Reference [2] is a study of our predictions of EIRP degradation due to RFI (i.e., increase in EIRP required to overcome the RFI effect) for the whole range of SSA data rates. The Shuttle S-band data rates fall in this range. The reasons for the shape of the degradation vs. data rate curve are analyzed for the cases of a fairly severe RFI environment with noise RFI and high-power CW RFI and of the same environment with the CW RFI replaced by noise RFI. The differences between the two curves are also analyzed. The analysis is in terms of the behavior of the eight-level-quantized probability density function of the matched-filter output as a function of data rate and type of RFI.

For the predictions presented here and in [2], it is assumed that channel losses (not including the effect of the TDRS nonlinearity) are the same with and without RFI and the same for all CNR's. This was found by analysis to be true for symbol rates about equal to those used by the Shuttle, for a general SSA return-link user who employs rate-1/2 coding. One source of losses, the symbol synchronizer, is studied in the next section, to see if the assumption is good for the Shuttle, at least for losses associated with it.

4. Analysis of Performance of Symbol Synchronizer

Since the predicted SER and the measured SER behave so differently around SER=.10, our link model must lack something. Aaron Weinberg suggested that perhaps the symbol synchronizer, a version of the digital data-transition tracking loop (DTTL), does not behave as well as expected. He pointed out that 16 points per symbol are taken in the digital symbol sync, so perhaps what would be a small rms timing error in an analog symbol sync could become a larger rms timing error in a digital one. An error of slightly more than 3.125% would become an error of 6.25% in the actual symbol sync. Although we were told by people who ran the ESTL test that the carrier tracking loop and the symbol sync behaved as well with RFI as without, the point seemed worth investigating.

The block diagram of our model of the DTTL is given in Figure 3. It differs from the actual DTTL in two ways. First, the DTTL and demodulator are actually integrated. Second, we show the quantities at the output of I_1, I_2, an I_3 as integrals, even though they are actually sums of samples. We are not sure of the signs with which the outputs of

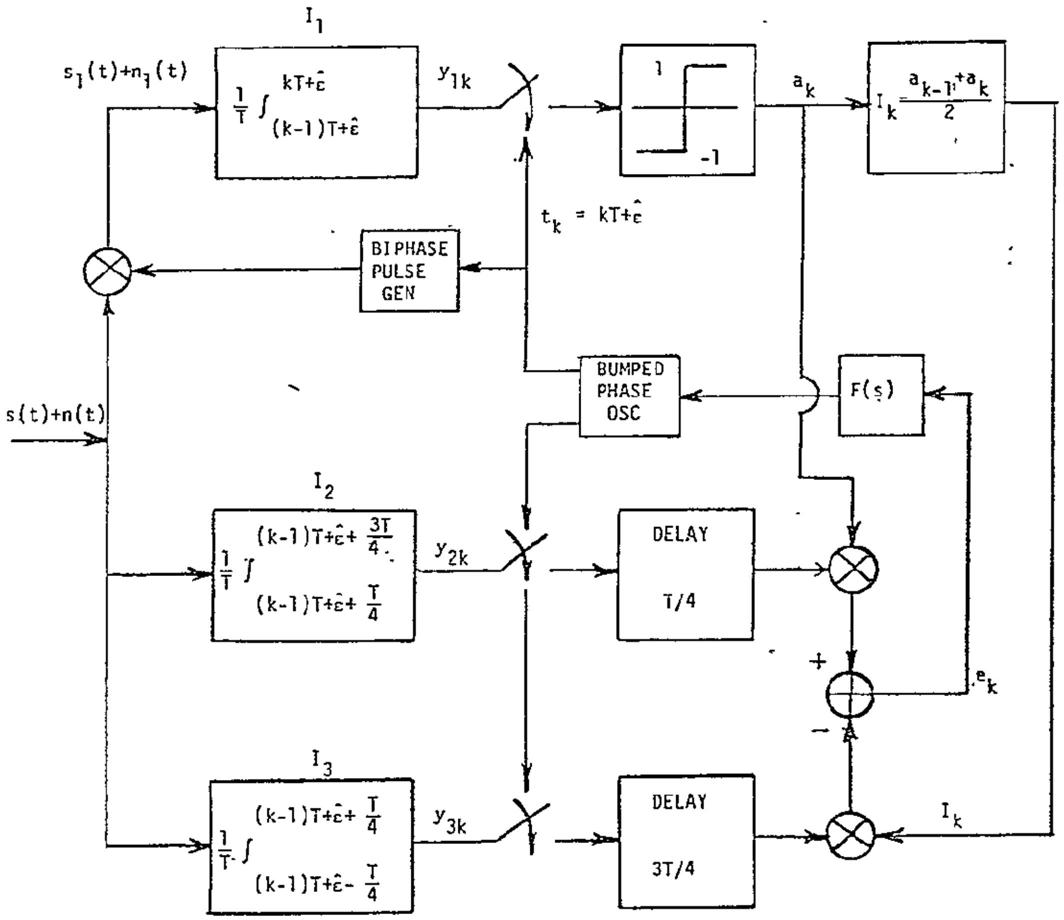

Figure 3. DTTL Model for Biphase Signal.

I_2 and I_3 are combined. If the signs are as shown (one positive and one negative), the tracking performance is considerably better than if the signs are as indicated in [3] (both positive [2]. We think perhaps an oversight was made in [3].

The full analysis of the performance of the DTTL is given in Section 1.3 of this final report.

The results to be presented are based on the following assumptions. The superior implementation of the loop is the actual one. The behavior of the DTTL is determined by an average of the RFI/no-RFI conditions since in a correlation time of the loop many RFI pulses occur. Different values of EIRP are used in the RFI and no-RFI cases, but in each case the EIRP is used at which LinCsim predicts an SER of .10 when the channel loss due to such things as imperfect carrier tracking is at its no-RFI value.

With these conditions we predict that without RFI the rms timing error is 1.2% of a symbol duration, while with RFI it is 1.4%.

Even though our analysis assumes that the timing error can take on a continuous range of values instead of the actual discrete set, our predictions indicate that the DTTL performance with RFI is about the same as the performance without RFI and that in both cases the performance is probably good.

5. Conclusions

Two conclusions may be drawn from our analysis: first, that our predictions are probably good within our model of the receiver, and second, that the assumption of our predictions that the symbol synchronizer works as well with RFI as without is probably a good one. We do not have the digital carrier tracking loop modeled, so we make no statement regarding it.

A possible source of trouble in the receiver that can be eliminated by studying [3], if [3] is accurate, is overflows in the accumulators.

Since we cannot explain the divergence between measurement and prediction, we feel there is probably some element of the receiver which does not act as expected when RFI is present. We would like to know if the receiver matches its description in [3].

REFERENCES

1. "TDRSS RFI Test Summary," Electronic Systems Test Laboratory, NASA/JSC, May 1982.

2. T. M. McKenzie et al., "First Interim Report, Analytical Evaulation of the Communication Features of TDRSS," TR-0483-8214, LinCom Corporation, Los Angeles, CA, April 1983.

3. Motorola Technical Proposal 2502-500, June 30, 1978. Prepared for Harris Electronic Systems Division.

4. TDRSS RFI MODEL AND SIMULATION

4.1 INTRODUCTION

In this chapter we report on the work done under Task #4, which calls for the updating of analytical models to describe the effects of the TDRSS radio-frequency interference (RFI) environment on Shuttle communication links. During the last two years, the analytical BER model was considerably refined. This is reproted on in Section 4.2. More recently, a Monte Carlo-type simulation of the RFI effect on BER has been developed in order to better model the S-Band Shuttle return links, on which interleaving is not used. The model, with a comparison of some of its preliminary results with those of the analytical model, is discussed in Section 4.3. Excellent agreement of the results of both models at data rates where interleaving has little effect tends to validate both models. Finally, in Section 4.4 the model of the RFI effect on synchronization and Doppler tracking performance is presented.

4.2 ANALYTICAL MODEL OF RFI EFFECT ON BIT ERROR RATE

1. Introduction

The TDRSS S-band return link and, to a lesser extent, the other TDRSS links (forward and return) will be subject to pulsed radio-frequency interference (RFI) of two types: wideband Gaussian noise and continuous wave (CW).

Supporting analysis of the model which has been developed to predict the RFI effect on bit error rate (BER) is presented here.

The organization of the rest of this reprot is as follows. Section 2 describes the generalized link which is treated. Section 3 gives the RFI environment model. Section 4 goes into general aspects of the model. The general approach had to be developed differently for the cases where more than one RFI pulses occurs in a symbol with significant and insignificatn probability. The two developments are called the low- and high-rate models, respectively, after the range of symbol rates in which they are applicable, and are described in Sections 5 and 6.

2. Link

2.1 General Link

The generalized link that is treated is sketched in Figures 2.1, 2.2, and 2.3. We now describe each element in the link.

The transmitted signal has the following characteristics. The modulation is BPSK. The data may be coded at rate 1/3 or uncoded, the symbol format may be NRZ or biphase, and the channel may be PN-spread or unspread. The modulator may exhibit gian and phase imbalance. There may be data asymmetry.

To the transmitted signal are added thermal noise and, possibly, RFI.

The receiver is modeled as follows. The first element is a bandpass filter which is assumed wide enough to pass the signal and PN sequence without distortion. Next is a composite nonlinearity which may be one nonlinearity, a cascade of such, or a linear amplifier. THen there is the PN-despreader, if appropriate, followed by the demodulator, matched filter, and Viterbi decoder, if appropriate. Post-nonlinearity thermal noise is negligible on the TDRSS links so is ignored. The receiver losses on the signal component of the matched-fitler output, with no loss on the random component due to pre-nonlinearity thermal noise and RFI. The receiver losses include those due to PN-despreading, demodulating, bit synchronizing, and imperfect transmitted signal.

2.2 Forward Link

For the forward link, the range channel is ignored with little effect on the BER of the command channel. The transmitter that is modeled is the one in the TDR satellite. We can ignore the uplink because it is essentially noise-free. THe receiver that is treated is the one in the user spacecraft.

2.3. Return Link

For the return link the transmitter is in the user spacecraft. The receiver is a combination of the receivers in the TDR satellite and the ground station. For the S-band and K-band links the bandpass filter is in the TDR satellite. The composite nonlinearity consists of the composite nonlinearity in the TDR satellite and, if the filter at input to the ground station receiver is at least as wide as the one at input to the TDR satellite, any nonlinearity at output of the ground receiver input filter.

3. RFI Environment Model

The model of the RFI environments is as follows.

First, the RFI is of two types, Gaussian noise and CW. In the entire passband of the IF filter preceding the link nonlinearity, noise-type RFI has flat power spectral density and the frequency of CW-type RFI is uniformly distributed.

Second, the correlation time of the IF filter preceding the link nonlinearity is less than the RFI pulse durations.

Third, the number of RFI pulses of any one type and power arriving in an interval of fixed duration is Poisson distributed.

4. General Approach

4.1 Introduction

In this chapter are discussed aspects of the model applicable at all symbol rates. The first section describes aspects of the sample-sum approach to approximating the matched-filter output, namely, the basic sample-sum approach, the basic sample description, sampling at less than the Nyquist rate, and sample descriptions in the PN-spread case. The next section tells how the CW-RFI frequency points are chosen over which averaging is done. The next section tells how that part of the matched-filter output corresponding to a CW.RFI pulse is modeled for RFI frequencies which cannot be modeled by the sample-sum approach. The last sections describe how decoder quantization step size is set, how a non-Gaussian quantized probability density function (pdf) is calculated, and how the coded BER is computed.

4.2 Sample-Sum Approach

4.2.1 Basic Sample-Sum Approach

In the sample sum approach the matched-filter output z is approximated by the sum of independent samples of the filter input taken at rate B, the one-sided IF frequency of the pre-nonlinearity filter, and scaled by 1/BT, as follows [2]:

$$z = \begin{cases} \sum_{i=1}^{BT} z_i, & \text{NRZ symbols} \\ \sum_{i=1}^{BT/2} z_i - \sum_{i=BT/2+1}^{BT} z_i, & \text{biphase symbols} \end{cases} \qquad (1)$$

where 1/T is the symbol rate (=data rate divided by code rate) of channel 1, the channel of interest, and where the channel-1 symbol format is as indicated. B is the Nyquist sampling rate. The samples are mutually independent if thermal noise and noise RFI are present during any or all of the samples and if when CW RFI is present its frequency and phase at the beginning of the pulse(s) are known. It is a good approximation to assume that the phase of CW RFI is constant during a sample duration.

Since the samples are independent, then the characteristic function Φ of z can be written as the product of the characteristic functions Φ_i of z_i:

$$\Phi(ju) = \begin{cases} \prod_{i=1}^{BT} \Phi_i(ju/BT), & \text{NRZ} \\ \prod_{i=1}^{BT/2} \Phi_i(ju/BT) \prod_{i=BT/2+1}^{BT} \Phi^*_i(ju/BT), & \text{biphase} \end{cases} \tag{2}$$

4.2.2 Description of Samples Taken at Nyquist Rate

When sampling is done at the Nyquist rate, a sample is the in-phase component of the nonlinearity output, adjusted for receiver loss and scaled by 1/BT. Post-nonlinearity thermal noise is negligible on the TDRSS links.

The input to the nonlinearity at any given time t is of the form $(S+n_{u1})\cos(\omega_0 t+\alpha) - n_{u2}\sin(\omega_0 t+\alpha)$, where ω_0 is the carrier radian frequency, S and α are the amplitude and phase, respectively, of the signal plus CW RFI, if present, and n_{u1} and n_{u2} are independent Gaussian random variables representing thermal noise plus noise RFI, if present. The nonlinearity input can be rewritten

ORIGINAL PAGE IS
OF POOR QUALITY

$$(S+n_{u1})\cos(\omega_0 t+\alpha) - n_{u2}\sin(\omega_0 t+\alpha) = R\cos(\omega_0 t+\alpha+\eta) \tag{3}$$

where

$$R^2 = (S+n_{u1})^2 + n_{u2}^2$$

$$\tan \eta = \frac{n_{u2}}{S+n_{u1}}$$

The output of the nonlinearity is $f(R)\cos(\omega_0 t+\alpha+\eta+g(R))$, where f and g are, respectively, the AM-to-AM and AM-to-PM functions of the nonlinearity.

In the receiver the signal is demodulated. The in-phase sample w_i is given by

$$w_i = f(R)\cos(\alpha+\eta+g(R)-\overline{g}) \tag{4}$$

where $\overline{g}$ is the phase tracked out by the demodulator.

Now the receiver losses must be accounted for. This is done by multiplying the signal component of w_i by a constant less than one. The receiver losses due to imperfect synchronization of the PN-despreader, demodulator, and symbol synchronizer and those due to imperfect transmitted signal can be well modeled this way. The RFI component is not similarly degraded. The receiver losses just described have either no effect or on the average no effect on the RFI component. The pre-nonlinearity thermal noise component of w_i is also left unaltered. The problem that remains is how to define the signal component s_i of w_i. Basically, s_i is defined by

$$s_i = Ew_i \tag{5}$$

where the expectation is taken over the independent quadrature components (q.c.) of pre-nonlinearity thermal noise if no RFI occurs when the sample is taken, over the independent q.c.'s of pre-nonlinearity thermal noise plus RFI if noise-type RFI occurs, and over the independent q.c.'s of pre-nonlinearity thermal noise and over the phase (which is uniformly distributed from $-\pi$ to π) of the RFI if CW-type RFI occurs.

Finally, the sample must be scaled by 1/BT.

Thus, the sample z_i is defined by

$$z_i = \frac{1}{BT} (\gamma s_i + w_i - s_i) \qquad (6)$$

where the receiver loss in dB is $-20 \log_{10}(\lambda)$.

The BER/RFI computer program calculates statistics of the sample z_i, which depend on signal phasor, power of RFI process, type of process, and, for a CW-type process, RFI phase.

4.2.3 Sampling at Less than Nyquist Rate

For some signals it is practically necessary to sample at a rate less than the Nyquist rate. The samples are independent, just as before. A lower sample rate is used for a signal with PN-spread channel. The mean and variance of the sample are the mean and variance of the Nyquist-rate sample scaled by B/R_s and $(B/R_s)^2$, respectively, where R_s is the lower sample rate.

4.2.4 Samples in the PN-Spread Case

In the case where the channel is PN-spread, the sample descriptions must be further developed. Over each of the sample durations (=inverse of PN-chip rate R_c) it is equally likely that the PN chip had positive and negative sign. Therefore, if M_+ and V_+ are the sample mean and variance, respectively, when the data and chip have the same sign and M_- and V_- are for different signs, then after despreading the sample mean and variance are given by

$$\text{Mean} = .5*(M_+ - M_-)$$

$$\text{Variance} = .5*(M_+^2 + V_+ + M_-^2 + V_-) - \text{Mean}^2 \qquad (7)$$

when the data has positive sign. When the data has negative sign the mean is the opposite of that given above and the variance is the same.

CW RFI frequencies more than $R_c/4$ away from the carrier frequency cannot be represented in the sample-sum approach. This point is addressed in Section 4.4.

4.3 Frequency Points Taken in CW-RFI Averaging

Some CW RFI frequencies are more damaging than others. Consider the matched-filter output when an RFI pulse which is much more powerful than signal plus pre-nonlinearity thermal noise occurs during the entire symbol. Roughly speaking, if the RFI frequency is near the carrier then for a good portion of the possible initial RFI phases the matched-filter output will fall in the soft-decision quantization level farthest from zero and on the opposite side of zero from the symbol, indicating a heavily weighted incorrect symbol to the decoder. In general, for a nonlinear link, if the RFI frequency is far from the carrier then for all values of initial RFI phase the matched-filter output will almost always fall in one of the two middle quantization levels, indicating a lightly-weighted symbol to the decoder, which is desirable under the circumstances.

The relative effect of the various frequencies depends on the pulse duration, symbol duration, symbol forman and whether the channel is PN-spread or not. Figures 4.1 to 4.5 give curves of a function of the RFI frequency relative to the carrier. In general, the larger the function's absolute value at a particular RFI frequency, the more harmful that frequency is to communication. Figures 4.1 and 4.2 show the matched-filter (M.F.) output when CW RFI and neither signal nor noise occur over the symbol duration, the channel is not spread, and, respectively, the symbol format is NRZ and biphase. Figure 4.3 shows the matched-filter output when the input over the symbol duration is all zero except for a CW occurring in a pulse short enough to be wholly contained in an NRZ symbol or in the first or second half of a biphase symbol and when the channel is not spread. Figure 4.4 shows the variance of the matched-filter output when a despread CW over the symbol duration is the matched-filter input. Figure 4.5 is the same as Figure 4.4 except that the despread CW occurs only in a pulse wholly contained in a symbol.

The other considerations in choosing a set of frequency points to be averaged over are accuracy and computation time.

Therefore, in general more points are used in the ranges over which the appropriate curve (of those given in Figures 4.1 to 4.5) has large magnitude than in the ranges over which the magnitude is small. Also, M.F. INPUT: $\cos(2\pi ft+\alpha)$, $0 \le t \le T$, where T = symbol duration

M.F. OUTPUT: $\frac{\sin(\pi fT)}{\pi fT}\cos(\pi fT+\alpha)$

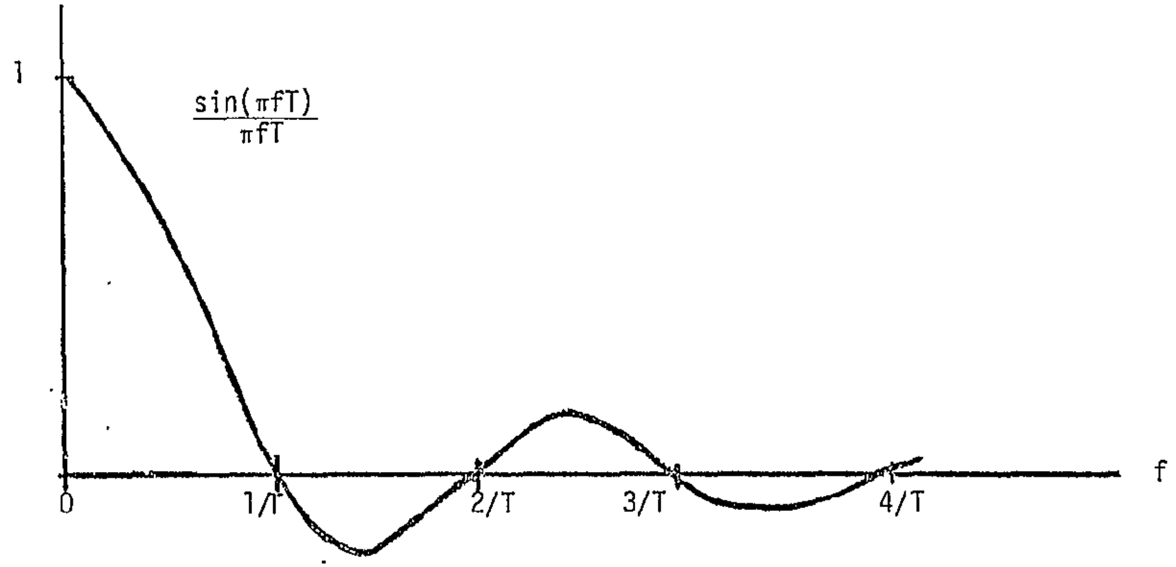

Figure 4.1. NRZ Matched-Filter Output When Input Is CW for Symbol Duration.

M.F. INPUT: $\cos(2\pi ft+\alpha)$, $0 \le t \le T$, where T = symbol duration

M.F. OUTPUT: $\frac{\sin^2(\pi fT/2)}{\pi fT/2}\ \sin(\pi fT+\overset{\alpha}{\phi})$

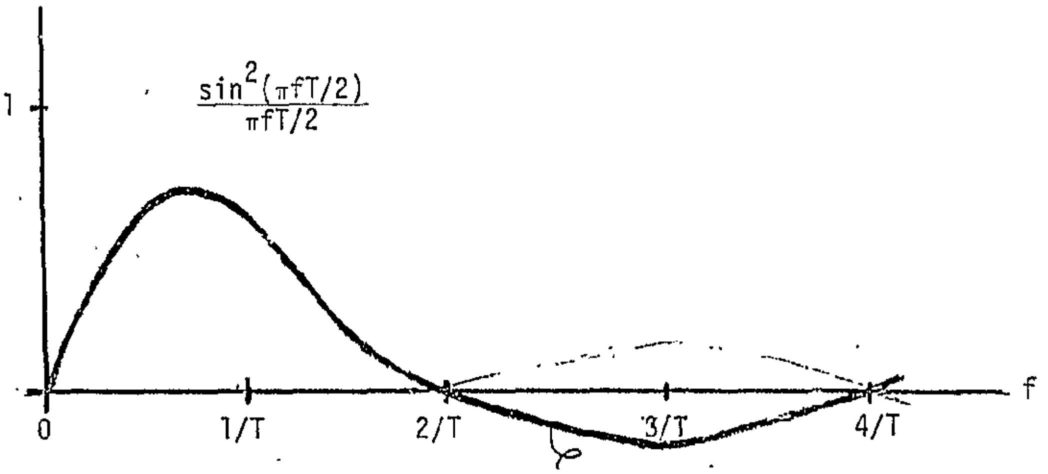

Figure 4.2. Biphase Matched-Filter Output When Input Is CW for Symbol Duration.

M.F. INPUT: $\cos(2\pi ft+\alpha)$ for $0 \le t \le \tau \le T/2$ and 0 for $\tau < t \le T/2$
where T = symbol duration and τ = RFI pulse duration

M.F. OUTPUT: $\frac{\tau}{T}\frac{\sin(\pi f\tau)}{\pi f\tau}\cos(\pi f\tau+\alpha)$

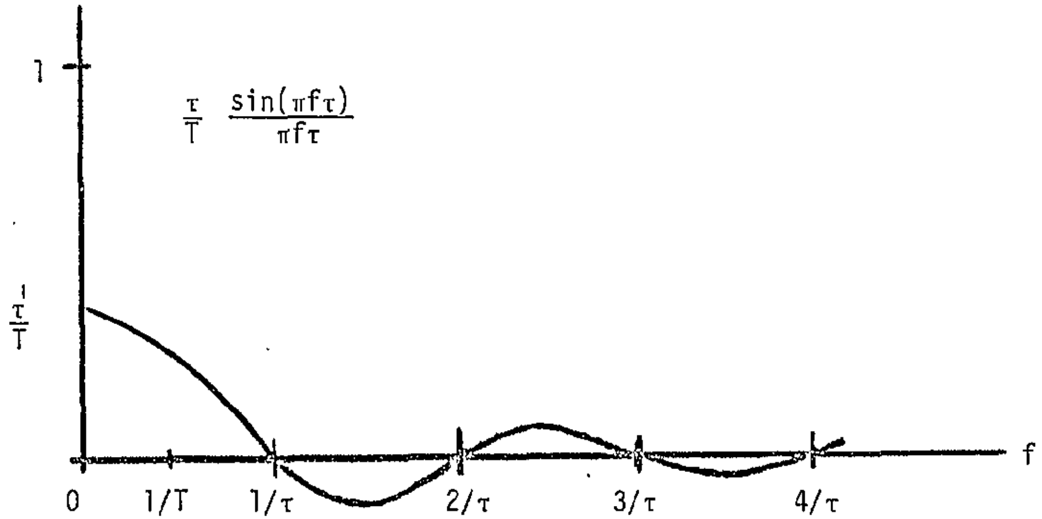

Figure 4.3. Matched-Filter Output When Input Is All Zero Except for a CW Pulse.

M.F. INPUT: PN-sequence times $\cos(2\pi ft+\alpha)$, $0 \le t \le T$, where T = symbol duration

VARIANCE OF M.F. OUTPUT: $$\frac{T_c}{T}\left(\frac{\sin(\pi f T_c)}{\pi f T_c}\right)^2 \frac{1}{2}\left[1+\frac{2\pi f T_c}{\sin(2\pi f T_c)}\;\frac{\sin(2\pi f T)}{2\pi f T}\;\cos(2\pi f T+2\alpha)\right]$$

where T_c = PN-chip duration

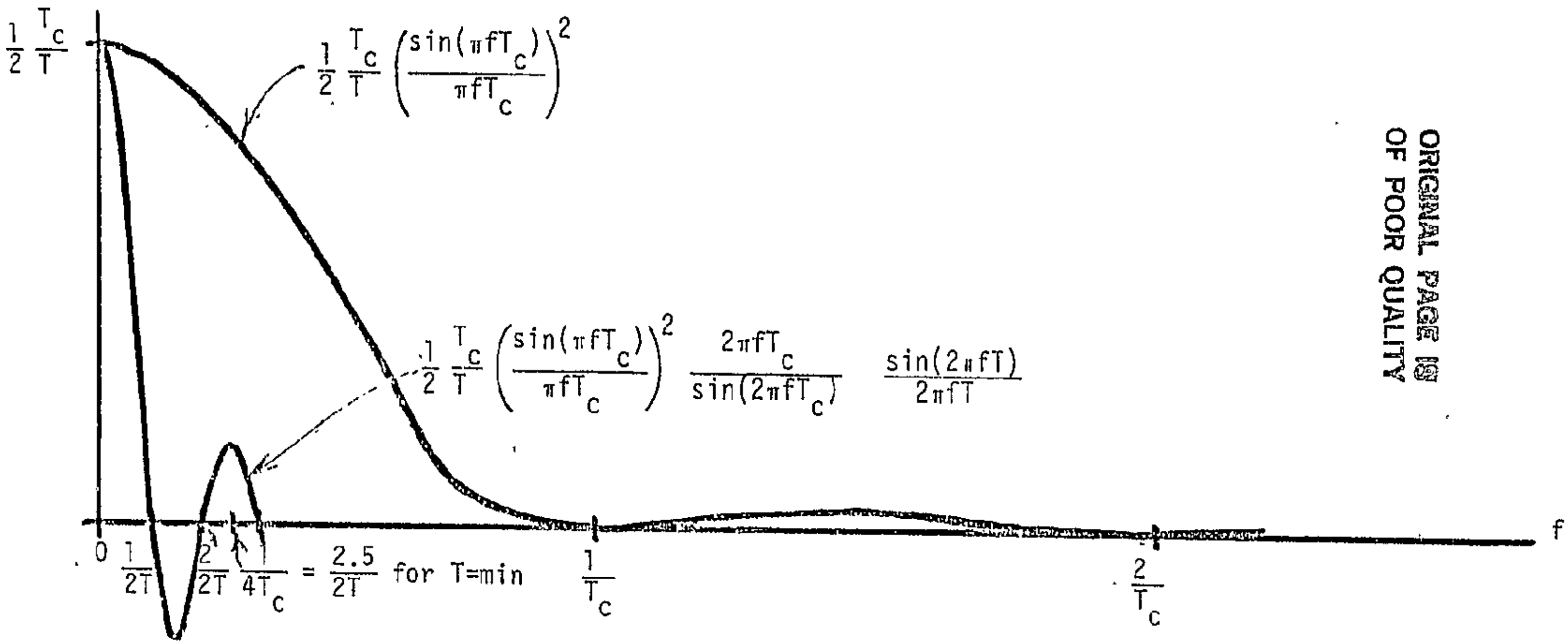

Figure 4.4. Variance of M.F. Output When Input Is Despread CW for Symbol Duration.

$$\text{M.F. INPUT:} \quad \begin{cases} \text{PN-sequence times } \cos(2\pi ft+\alpha), & 0 \le t \le \tau \le T, \\ 0, & \tau < t < T \end{cases}$$

where T = symbol duration and τ = pulse duration

$$\text{M.F. OUTPUT:} \quad \frac{\tau T_c}{T^2}\left(\frac{\sin(\pi f T_c)}{\pi f T_c}\right)^2 \frac{1}{2}\left[1 + \frac{2\pi f T_c}{\sin(2\pi f T_c)} \; \frac{\sin(2\pi f\tau)}{2\pi f\tau} \; \cos(2\pi f\tau + 2\alpha)\right]$$

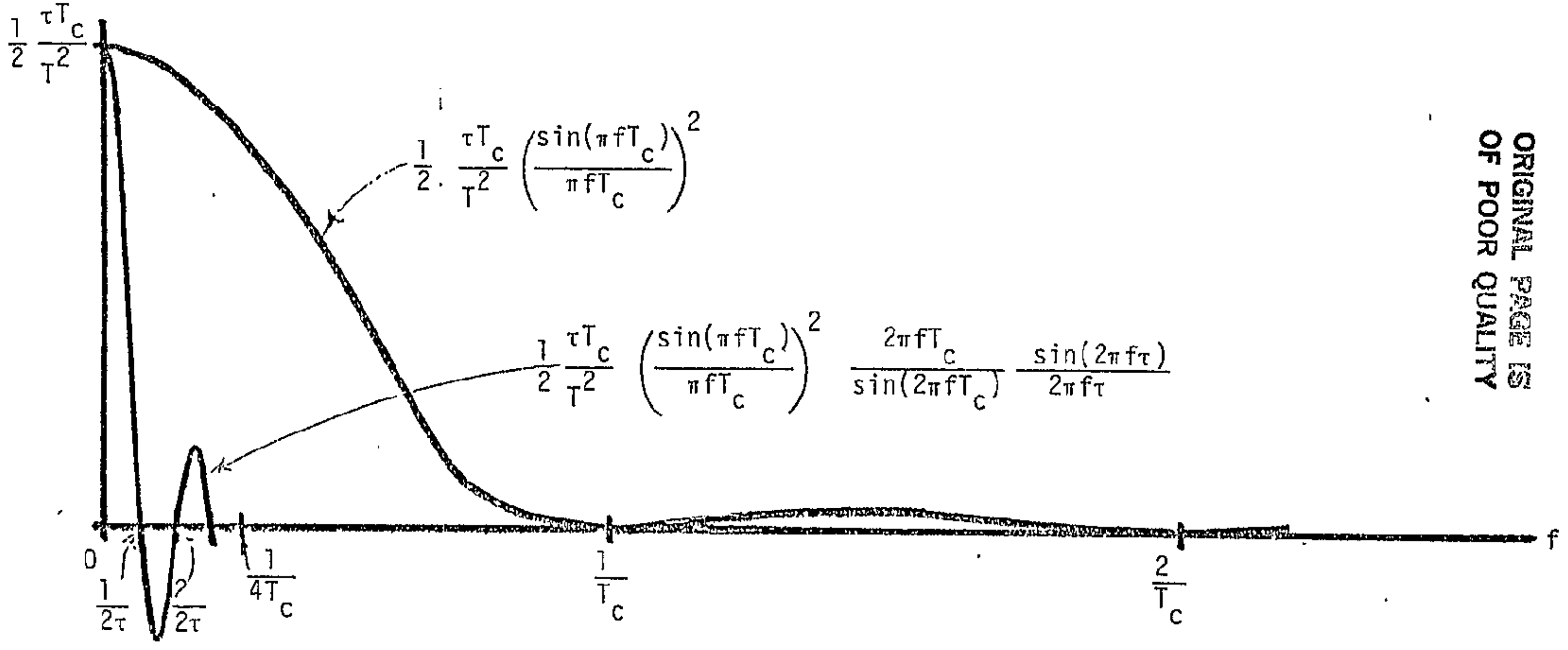

Figure 4.5. Variance of M.F. Output When Input Is All Zero Except for a Despread CW Pulse.

in the PN-spread cases, represented in Figures 4.4 and 4.5, more frequencies are chosen between 0 and approximately 1.5/min(τ,T), where the curve fluctuates significantly, than between 1.5/min(τ,T) and $R_C/4$, where the fluctuation is less. Here, τ is an RFI pulse duration.

4.4 Matched-Filter Output When Sample-Sum Approach Cannot Be Used

The sample-sum approach can be used to approximate the part of the matched-filter output due to periods of time when no RFI or noise RFI or CW RFI of some frequencies is occurring. When the sample rate is the Nyquist rate all CW RFI frequencies can be represented, since at least two samples per period are needed in the case of channel 1 unspread. However, when the sample rate is lower, the CW RFI frequencies farthest from the carrier cannot be represented, as is described in Sub-Section 4.2.4. The pessimistic assumption is made that for those frequencies, during the CW RFI pulse no signal and no noise are present, which is close to the truth for the RFI environments seem so far. Then the mean of that part of the matched-filter output due to an RFI pulse is zero and the variance can be analytically obtained, as given in Figures 4.4 and 4.5, with the part of the result dependent on RFI initial phase neglected.

4.5 Decoder Quantization STep Size

The step size of the 8-level quantizer at input to the Viterbi decoder will be based on a coherent or non-coherent power measurement at some point in the receiver. The step size we have chosen yields good results but is by no means universally used.

The step size is a fraction of the matched-filter output mean when no RFI occurs during the symbol duration. The fraction depends on the code rate and the BER for which the decoder is designed. If the channel were linear with only additive white Gaussian noise, the step size would equal $\sigma/2$, where σ^2 is the variance of the matched-filter output, which is the optimal step size under such conditions.

It was found that this step size yields smaller EIRP degradations due to RFI than a step size which equals half the variance of the non-RFI matched-filter output. The improvement is 0.1, 0.9, and 2.6 dB on degradations of 2.3, 5.8, and 12.6 dB, respectively.

4.6 Calculation of Non-Gaussian Quantized Pdf

Calculation of a non-Gaussian quantized pdf is called for in two cases, one, for the high-rate model when one wishes to treat non-Gaussian conditional pdf's and, two, for the low-rate model always. In general, to obtain the quantized pdf the probability must be calculated that the matched-filter output z is in three types of intervals, finite, infinite on the left, and infinite on the right. From [3], the expressions for such probability are:

$$\Pr(Z_1<z<Z_2) = \frac{2}{\pi}\int_0^\infty \frac{1}{u} R(u)\cos\left(\frac{Z_1+Z_2}{2}u-\theta(u)\right)\sin\left(\frac{Z_2-Z_1}{2}u\right)du \qquad (8)$$

$$\Pr(z<Z_1) = \frac{1}{2}-\frac{1}{\pi}\int_0^\infty \frac{1}{u} R(u)\sin(\theta(u)-Z_1u)du \qquad (9)$$

$$\Pr(Z_2<z) = \frac{1}{2}+\frac{1}{\pi}\int_0^\infty \frac{1}{u} R(u)\sin(\theta(u)-Z_2u)du \qquad (10)$$

where R and θ are, respectively, the radius and phase functions of the characteristic function of z.

ORIGINAL PAGE IS
OF POOR QUALITY

4.7 Calculation of BER From Quantized Pdf

For both the coded and uncoded links the BER is calculated from the two quantized pdf's of the matched-filter output, one for positive and one for negative symbol.

In the uncoded case the BER is the average of the smaller of the probabilities for each polarity of the symbol.

In the coded case, the BER computation is based on the model that if two different information channels have the same cut-off rate R_0 and the same coder/decoder, then the BER will be the same on both. R_0 is given by [3]

$$R_0 = -\log_2 \sum_{i=1}^{8} \{\tfrac{1}{2}[\sqrt{P_+(i)} + \sqrt{P_-(i)}]\}^2. \qquad (11)$$

where $P_+(i)$ is the probability that the matched-filter output is contained in the i-th quantization level when a positive symbol is transmitted and $P_-(i)$ is the same for negative symbol. By curve-fitting to data points obtained for the linear additive-Gaussian-noise channel, the following relationship was obtained [3]:

$$\log_{10}\mathrm{BER} = \log_{10} K_1(R) + \frac{K_2(R)}{R} \log_{10}\left[\frac{2^{1-R_0}-1}{1+\exp(a(R_0-b))}\right] \qquad (12)$$

where

R = code rate = 1/2 or 1/3

$a = 3.017$, $b = 1.602$

$$\left.\begin{matrix} K_1 = 102.31 \\ K_2 = 5.834 \end{matrix}\right\} \text{if } R = 1/2, \qquad \left.\begin{matrix} K_1 = 42.284 \\ K_2 = 5.918 \end{matrix}\right\} \text{if } R = 1/3$$

5. Low-Rate Model

5.1 Introduction

THe low-rate model is used when the probability of more than one RFI pulse arriving in a symbol duration is significant and the average RFI pulse duration is less than half the symbol duration for NRZ symbols, one fourth the symbol duration for biphase symbols.

The rest of this chapter is organized as follows. In the next section the model assumptions are given. Then in the next two sections the pulse types are described, on which the model is based. In the next section the characteristic function of the matched-filter output is derived. Lastly, the method of carrier phase recovery is treated.

5.2 Assumptions

The low-rate model is based on two assumptions:

- Each RFI pulse is wholly contained in a symbol if symbol format is NRZ and wholly contained in half a symbol if symbol format is biphase.
- RFI pulse duration is negligible compared to pulse inter-arrival time.

5.3 Pulse Types

For each RFI process in the original environment description there is defined a pulse type. For each CW-type pulse type there are defined many sub-types, each corresponding to a pair from a discrete set of pairs of RFI frequency and initial phase values.

In order to extend the applicability of the low-rate model to a little bit higher symbol rates, corresponding to each pulse type with the ratio of the pulse duration τ to symbol duration T equal to at least .33 a new pulse type is created. This is an attempt to account for the fact that a sizeable portion of such long pulses will not lie wholly within one symbol (half symbol if biphase). The pulse duration of the new type will be half that of the parent type. If λ is the pulse arrival rate of the parent pulse type then the parent's arrival rate is reduced by $\frac{1}{2}\frac{\tau}{T}\lambda$ and the new type's arrival rate is set to $\frac{\tau}{T}\lambda$.

5.4 Pulse Description

A description of each pulse type or sub-type, conditioned on signal phasor, is obtained in the following way. It is assumed that the signal phasor stays the same throughout a pulse. The mean M_i and variance V_i of that part of a matched-filter output corresponding to the pulse is obtained by summing up the mean and variance of samples occurring during the pulse. The sample rate is the filter bandwidth in the unspread case and the PN chip rate in the spread case. Phase of CW RFI is assumed constant during a sample. Lastly, the mean M_0 and variance V_0 of that part of a matched-filter output corresponding to no RFI during the pulse duration are subtracted from the mean and variance with RFI.

We have in this way obtained a ratio Ψ_i of Gaussian characteristic functions. Let Φ_i be the characteristic function for a pulse duration with RFI, Φ_0 without RFI. Then

$$\Phi_i(ju) = \exp(jM_iu - V_i^2u^2/2) \tag{13}$$

$$\Phi_0(ju) = \exp(jM_0u - V_0^2u^2/2) \tag{14}$$

$$\Psi_i(ju) = \Phi_i(ju)/\Phi_0(ju) = \exp[j(M_i-M_0)u-(V_i^2-V_0^2)u^2/2] \tag{15}$$

5.5 Characteristic Function of Matched-Filter Output

To obtain the characteristic function Φ of the matched-filter output, functions Ψ_+ and Ψ_- have to be defined for the total RFI pulse process and then the Poisson statistics have to be applied.

Since each of the RFI pulse types has a Poisson arrival process, then all the types may be combined into one type which also has a Poisson arrival process. If λ_i is the arrival rate of the i-th pulse type then we define the functions Ψ_+ and Ψ_- as follows:

$$\Psi_+ = \frac{1}{\lambda}\sum_i \lambda_i \Psi_{+i} \tag{16}$$

$$\Psi_- = \frac{1}{\lambda}\sum_i \lambda_i \Psi_{-i} \tag{17}$$

where

$$\lambda = \sum_i \lambda_i$$

and where Ψ_{+i} and Ψ_{-i} are Ψ_i conditioned on, respectively, positive and negative channel-1 symbol.

We need the characteristic function of the matched-filter output when there are no RFI pulses in the symbol. Suppose Φ_{0+} is the characteristic function of the contribution to an integrate-and-dump filter output of one sample where the channel-1 signal is positive, Φ_{0-} the same but for negative signal. Suppose that N_{++} and N_{+-} are the number of positive-signal samples that are, respectively, added and subtracted into the matched-filter output and N_{-+} and N_{--} are the number of negative-signal samples that are, respectively, added and subtracted into the matched-filter output. Then the characteristic function Φ_0 of the no-RFI matched-filter output conditioned on a particular symbol polarity and asymmetry situation (which determines N_{++}, N_{+-}, N_{-+}, and N_{--}) is given by

$$\Phi_0 = \Phi_{0^+}^{N_{++}} (\Phi^*_{0^+})^{N_{+-}} \Phi_{0^-}^{N_{-+}} (\Phi^*_{0^-})^{N_{--}} \tag{18}$$

We now make the assumption that pulse duration is small compared to pulse inter-arrival time and to symbol duration. We employ the Poisson statistics of the combined pulse process to obtain the characteristic function

$$\begin{aligned}\Phi(ju) = {} & \Phi_0(ju)\exp\{\lambda \frac{N_{++}}{N} T[\Psi_+(ju)-1]+\lambda \frac{N_{+-}}{N} T[\Psi^*_+(ju)-1] \\ & + \lambda \frac{N_{-+}}{N} T[\Psi_-(ju)-1] + \lambda \frac{N_{--}}{N} T[\Psi^*_-(ju)-1]\}\end{aligned} \tag{19}$$

where

$N = N_{++} + N_{+-} + N_{-+} + N_{--}$

T = channel-1 symbol duration

5.6 Carrier Phase Recovery

The program calculates an approximate value of carrier phase offset as the sum of two angles.

The first is that angle which brings the i-th signal phasor to the i-th half-plane in such a way that the sum of the inner products of the actual phasors with nominal (i.e., before any gain and phase imbalance are imposed) is maximized.

The second angle is due to the RFI and the nonlinearity and is calculated as follows. Take a phasor with squared magnitude equal to the average transmitted signal power and with zero phase. Obtain the average phasor out of the nonlinearity conditioned on no-RFI and on each RFI process in the environment description. This is done for CW-type processes in the manner of noise-type processes. Weight the conditional phasors by duty cycles and sum. The second angle is the phase of the result.

6. High-Rate Model

6.1 Introduction

The high-rate model is used when the low-rate model is not applicable.

In the rest of this chapter we discuss the model assumptions, the symbol types on which the model is based, the probability density function (pdf) of the matched-filter output, and the carrier phase recovery.

6.2 Assumptions

The basic assumptions of the high-rate model are these:

- There is no RFI pulse overlap.
- All or part of at most one pulse occurs during a symbol.
- For coded links, the RFI effects on symbols which are successive at the encoder output are independent; i.e., interleaving is used when the symbol rate is high enough so that there is a significant probability that one RFI pulse

may overlap successive symbols.

6.3 Symbol Types

Over the duration of a symbol, either no RFI or RFI of a particular type, power, and duration occurs. Each such case is herein called a symbol type.

The symbol types and their duty cycles are derived from the description of the RFI environment as follows.

If an RFI process has $\tau > T$, where τ is pulse duration and T is symbol duration, then the type of symbol which corresponds to it has RFI occurring during the entire symbol and has the same duty cycle as the process. For an RFI process for which $\tau < T$ and duty cycle is c, the symbol type has RFI occurring during τ out of T and no RFI during the rest and has duty cycle cT/τ.

When τ and T are roughly comparable, then it will happen with significant probability that RFI occurs during only part of a particular symbol when $\tau > T$ and that only part of a pulse occurs during a symbol when $\tau < T$. We take the range of affected rates to be those for which $\tau/4 \leq T \leq 3\tau$. A new symbol type is created. The new symbol has RFI occurring during $\min(\frac{1}{2}T, \frac{1}{2}\tau)$ and no RFI occurring for the rest of T. Say the duty cycle of the parent symbol type is c. Then the duty cycle of the parent is decreased by $\frac{1}{2}\frac{T}{\tau}c$ if $\tau > T$ and by $\frac{1}{2}\frac{\tau}{T}c$ if $\tau < T$. In both instances the duty cycle of the new symbol type is taken to be twice the amount by which the parent is decreased.

6.4 Pdf of the Matched-Filter Output

The pdf of the matched-filter output is obtained as the weighted sum of many conditional pdf's. For a particular symbol polarity, set of preceding and following symbols when there is data asymmetry, and epoch of RFI pulse within the symbol, the pdf is calculated as follows:

$$P(\cdot) = p(\cdot|\text{symbol has no RFI}) \times (\text{duty cycle of no-RFI symbol}) + \sum_i p(\cdot|\text{symbol is i-th type with RFI}) \times (\text{duty cycle of i-th type of symbol with RFI}) \tag{20}$$

If the i-th type of symbol has CW RFI then p(·| symbol has i-th type of RFI) is actually the weighted sum of pdf's conditioned on RFI frequency and initial phase. This pdf is then averaged over the set of preceding and following symbols if there is data asymmetry and over the epoch of the RFI pulse, to obtain the final, unconditional pdf.

6.5 Carrier Phase Recovery

Just as in the low-rate model the carrier phase offset is calculated as the sum of two angles.

The first angle is the same as in the lo-rate model.

The second angle is obtained by roughly modeling the Costas loop that would actually be used for phase tracking in the TDR satellite. The angle is obtained as follows. Take a phasor with squared magnitude equal to the average transmitted power with zero phase. For each type of loop arm-filter output (i.e., no-RFI or with RFI from a particular RFI process occurring during the appropriate fraction of the symbol) obtain the average phasor out of the nonlinearity. These average phasors are then raised to 2, weighted, and summed. The phase of the result is the second angle.

REFERENCES

1. "Tracking and Data Relay Satellite System (TDRSS) Users' Guide," Revision 4, STDN No. 101.2, GSFC, Greenbelt, MD, January 1980.
2. Davisson, L. D., and Milstein, L. B., "On the Performance of Digital Communications Systems with Bandpass Limiters--Parts I and II," IEEE Transactions on Communications, Vol. COM-20, No. 5, pp. 972-980, October 1972.
3. Weinberg, Aaron, "Coded BER Performance for the Nonlinear TDRSS Communication Channel Corrupted by Pulsed RFI," STI/E-TR-8115, Stanford Telecommunications, Inc., McLean, VA, 21 March 1980.

4.3 MONTE CARLO-TYPE SIMULATION OF RFI EFFECT ON BIT ERROR RATE

1. Introduction

These sections describe our Monte Carlo program that models the effect of pulsed radio-frequency interference (RFI) on the bit error rate (BER) of a convolutionally encoded signal when no interleaving is done. Section 2 introduces the link model used. Section 3 discusses the simulation approach. Section 4 shows some results obtained by this method and compares them with those obtained with the analytical CLASS program documented in Section 4.2 of this final report.

2. Link Model

The link model is sketched in Figure 2.1. We proceed to write expressions for the signal at various places in the link.

First we describe the transmitted signal. We assume the information data are binary. Each data stream is coded with code rate 1/2. The symbol format is non-return-to-zero (NRZ). A perfect signal is assumed. Thus for each data bit d, a pair of symbols $\underline{v} = (v_1, v_2)$ are generated. In this simulation we use only BPSK modulation. The extension to QPSK is immediate. The signal is given by

$$S(t) = \sqrt{2P}\,(\cos \omega_0 t + \theta_v) \qquad (1)$$

where θ_v is determined by a symbol. Specifically, $\theta_v=0$ for $v_i = 0$, $\theta_v = \pi$ for $v_i = 1$ where v_i denotes any symbol out of encoder; P is the signal power; ω_0 is the carrier frequency.

The uplink noise process after filtering by the TDRS input bandpass filter (BPF) can be represented as

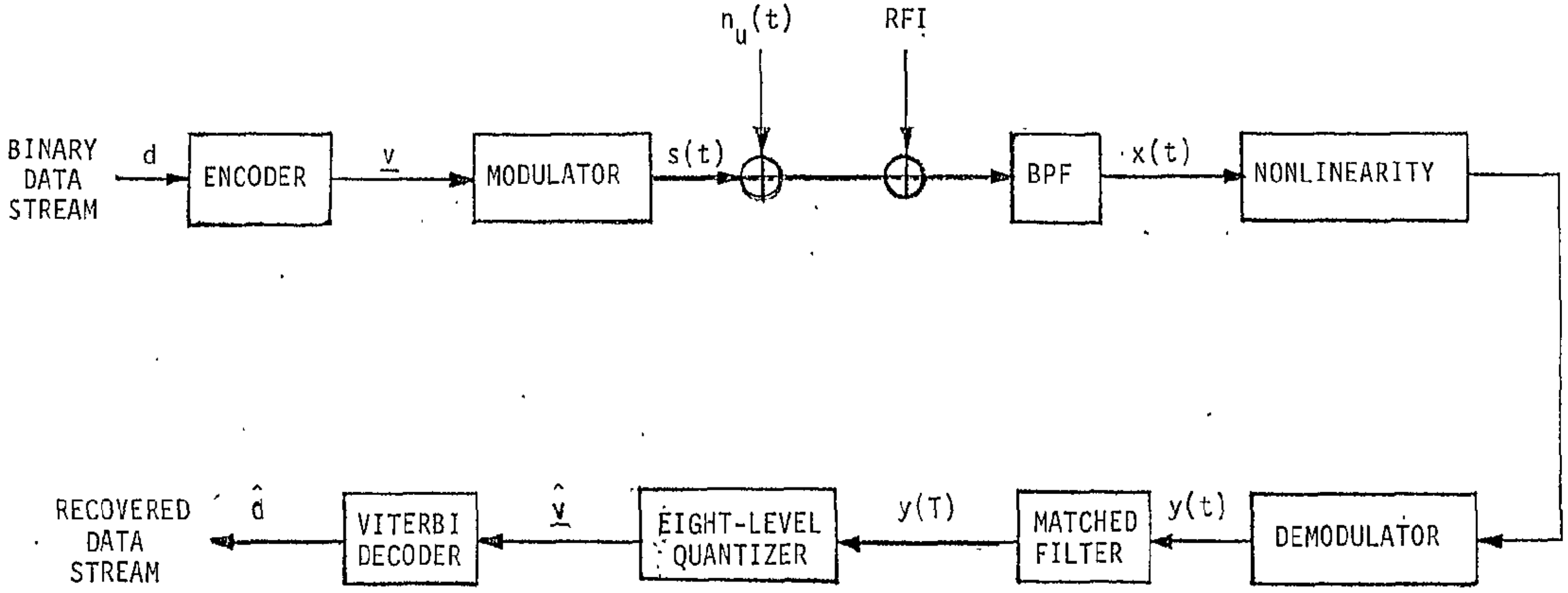

Figure 2.1 Link Model

$$n_u(t) = \sqrt{2}\, n_c(t) \cos \omega_0 t - \sqrt{2}\, n_s(t) \sin \omega_0 T \qquad (2)$$

$n_u(t)$ is a noise process with two-sided power spectral density $N_0/2$. Thus $n_c(t)$ and $n_s(t)$ are random variables with the distribution $N(0,N_0B/2)$ where B is the one-sided IF bandwidth of the input filter.

Also in the uplink, RFI is added to the signal. The RFI environment is composed of two types of processes, namely, the noise-like process and CW processes. They can be represented respectively as follows:

$$RFI_{noise} = \sqrt{2}\, N_c \cos \omega_0 t - \sqrt{2}\, N_s \sin \omega_0 t \qquad (3)$$

$$RFI_{CW} = \sqrt{2J} \cos(\omega_1 t+\theta) \cos \omega_0 t - \sqrt{2J} \sin(\omega_1 t+\theta) \sin \omega_0 t \qquad (4)$$

where N_c, N_s are Gaussian random variables with the distribution $N(0,N_0'B/2)$ and J is the power of a CW pulse. θ is uniformly distributed over $(0,2\pi)$. ω_1 is the frequency relative to the carrier frequency within the bandwidth of BPF. ω_1 is also a random variable uniformly distributed over the whole bandwidth. Note that RFI does not occur all the time. Its arrival process is exponentially distributed with some rate. Details of RFI processes will be discussed in Section 3. We assume the BPF passes the signal without distortion. Thus the signal prior to the clipper can be represented as

$$x(t) = s(t) + n_u(t) + RFI\cdot I(t)$$

$$= \sqrt{2P} \cos(\omega_0 t+\theta_v) + (\sqrt{2}\, n_c \cos \omega_0 t - \sqrt{2}\, n_s \sin \omega_0 t)$$

$$+ I_1(t)(\sqrt{2}\, N_c \cos \omega_0 t - \sqrt{2}\, N_s \sin \omega_0 t)$$

$$+ I_2(t)(\sqrt{2J} \cos(\omega_1 t+\theta) \cos \omega_0 t - \sqrt{2J} \sin(\omega_1 t+\theta) \sin \omega_0 t) \tag{5}$$

where $I(t)$, $I_1(t)$, $I_2(t)$ are binary random variables, i.e. 0 or 1 with the probabilities determined from arrival rates and pulse duration.

$x(t)$ can be rewritten in complex form as

$$x(t) = \mathrm{Re}\{\sqrt{2P}\, e^{j(\omega_0 t+\theta_v)} + (\sqrt{2}n_c + j\sqrt{2}n_s)e^{j\omega_0 t} + I_1(t)(\sqrt{2}N_c + j\sqrt{2}N_s)e^{j\omega_0 t}$$

$$+ I_2(t)\sqrt{2J}\, e^{j(\omega_1 t+\theta)}\, e^{j\omega_0 t}\}$$

$$= \mathrm{Re}\{[(\sqrt{2P}d + \sqrt{2}n_c + I_1(t)\sqrt{2}N_c + I_2(t)\sqrt{2J}\cos\phi(t))$$

$$+ j(\sqrt{2}n_s + I_1(t)\sqrt{2}N_s + I_2(t)\sqrt{2J}\sin\phi(t))]e^{j\omega_0 t}\}$$

$$= \mathrm{Re}\{[x_1(t) + jx_2(t)]e^{j\omega_0 t}\} \tag{6}$$

where

$d = \pm 1$ with equal probability,

$\phi(t) = \omega_1 t+\theta$, ω_1 and θ are random variables defined before

$$x_1(t) = \sqrt{2P}d + \sqrt{2}n_c + I_1(t)\sqrt{2}N_c + I_2(t)\sqrt{2J}\cos\phi(t) \tag{7}$$

$$x_2(t) = \sqrt{2}n_s + I_1(t)\sqrt{2}N_s + I_2(t)\sqrt{2J}\sin\phi(t) \tag{8}$$

Note that $x_1(t)$ and $x_2(t)$ are random variables and functions of t. Define

$$R(t) = \sqrt{x_1^2(t)+x_2^2(t)} \tag{9}$$

$$\psi(t) = \tan^{-1}(x_2(t)/x_1(t)) \tag{10}$$

So are R(t) and $\psi(t)$ random variables.

We can represent x(t) in the following way:

$$x(t) = \mathrm{Re}\{R(t)e^{j\psi(t)}e^{j\omega_0 t}\} \tag{11}$$

From now on, we suppress t in R(t) and $\psi(t)$ for convenience. The characteristics of the clipper are shown in Figure 2.2. We denote the AM/AM characteristic as f(R) and the AM/PM characteristic as g(R). Then we have the following signal representation after the clipper:

$$z(t) = \mathrm{Re}\{f(R)e^{j(\omega_0 t+\psi(t)+g(R))}\} \tag{12}$$

The demodulated signal can be represented as

$$y(t) = \mathrm{Re}\{f(R)e^{j(\psi(t)+g(R)-\overline{\theta})}\} = f(R)\cos(\psi(t)+g(R)-\overline{\theta}) \tag{13}$$

where $\overline{\theta}$ is the tracked phase.

In the next step, the signal goes to the matched filter. The matched filter is modeled as an integrate-and-dump filter which performs as follows:

$$y(T) = \frac{1}{T}\int_{t_0}^{t_0+T} y(t)dt \tag{14}$$

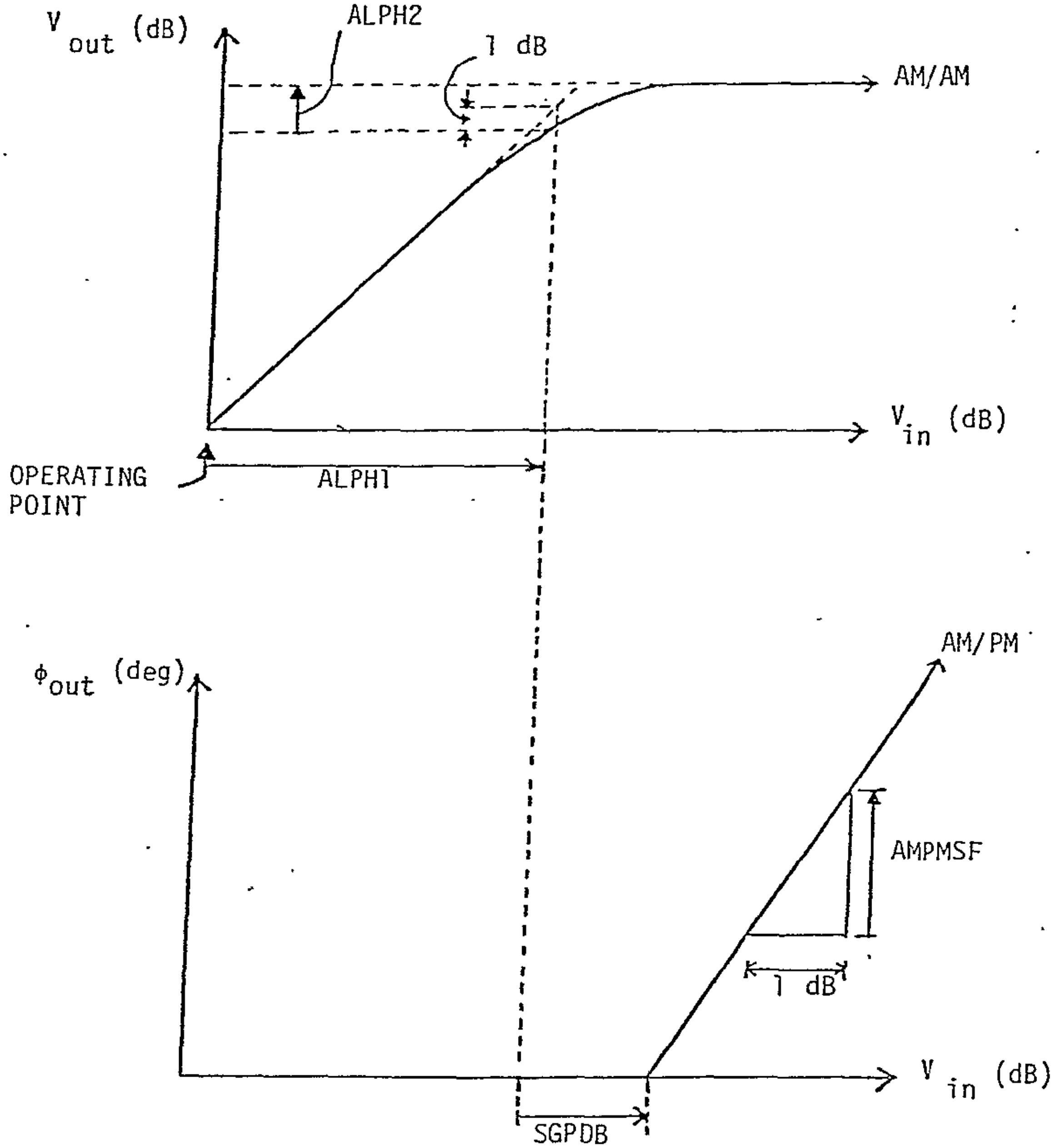

Figure 2.2 Parameters Defining Clipper Characteristic

where t_0 is the optimum time to start integrating. We assume an ideal symbol synchronizer. Next, y(T) passes through the quantizer which is eight-level with fixed step size. Finally, the signal enters the Viterbi decoder which attempts to reconstruct the data stream. Note that the Viterbi decoder in this simulation is only suboptimal because of the RFI environment and the eight-level quantizer being used.

3. Simulation Approach

Having presented the overall picture of the link model, we are now ready to describe the simulation approach. In Section 3.1, the comparison of baseband and RF signal representations is discussed. In Section 3.2, how the RFI processes are generated and added to the signal is presented. In Section 3.3, how the output of the matched filter is approximated is presented. In Section 3.4, the Viterbi decoder and quantizer used in the program are discussed. In Section 3.5, how the random number generator works is presented. Finally, in Section 3.6, a flow chart is presented to show how the simulation works.

3.1 Comparison of Baseband and RF Signal Representations

Although we have carrier frequency involved in the derivation of Section 2, we don't need it in the simulation because we assume no distortion in the BPF and ideal carrier recovery in the demodulator. Thus baseband representation is used in the simulation. In baseband representation the signal is represented as

$$S = (\sqrt{2P}\, v, 0)$$

where v is a binary symbol (0 or 1) with equal probability. Its power is 2P. In RF representation, the signal is represented as

$$s(t) = \sqrt{2P}(\cos \omega_0 t+\theta_v) = \pm\sqrt{2P}\cos \omega_0 t$$

where θ_v is either 0 or π with equal probability and its power is

$$\frac{1}{T}\int_0^T s^2(t)dt = 2P\frac{1}{T}\int_0^T \cos^2 \omega_0 t\, dt = P$$

We see that the signal power in baseband representation is twice that in RF representation. However, we can see that the noise power in baseband representation is also twice that in RF representation. Thus we wind up with the same SNR in both representations. As far as bit error rate is concerned, both representations give the same answer.

3.2 Generating RFI Processes

RFI processes are characterized by power levels, arrival rates, and pulse durations. The arrival processes of RFI are assumed to be Poisson processes. Up to ten noise-like and ten CW processes may occur in this simulation. Each pulse has the same pulse duration. The product of arrival rate and pulse duration is duty cycle, which reflects the traffic intensity of the RFI process. Since we are interested in the steady-state behavior and the pulse duration is constant, all statistical features are determined by arrival rates. Two well-known results in queueing theory apply to our model. First, the sum of several Poisson processes yields another Poisson process with the new rate being the sum of rates of each process. Second, the interarrival times of a Poisson process with rate λ are independently and identically exponentially distributed with parameter λ^{-1}. These facts determine our approach to generating RFI pulses.

3.3 Approximation of Output of Matched Filter

The signal out of the matched filter is represented in Eq. (2-14), which is rewritten as follows:

$$y(T) = \frac{1}{T}\int_{t_0}^{t_0+T} y(t)dt$$

We approximate this integration by summing samples taken at the Nyquist rate B, where B is the bandwidth of the BPF. Thus,

$$y(T) \approx \frac{1}{N}\sum_{n=1}^{N} y(t_0+\frac{n}{B})$$

3.4 Eight-Level Quantization and Viterbi Decoder

For binary input over the additive white Gaussian noise (AWGN) channel, the Viterbi decoder is to find the data bit stream that maximizes the metric

$$\sum_{i=1}^{L}\sum_{j=1}^{n} y_{ij}x_{mij} \qquad (1)$$

where n is the inverse of the code rate; $m\varepsilon[1,2,3,\ldots,2^M]$, M is the memory length of code; L is the length of the code sequence, which can be any integer. x_{mij} is either 1 or -1. Note that this metric is optimal only when the channel is AWGN and y_{ij} is a real number which is the output of the matched filter. However, since the matched-filter output must be quantized and since RFI is present, the Viterbi decoder operation is suboptimal. An eight-level quantizer is put in front of the Viterbi decoder. We get the decoded data after 4K bits where K is the constraint length of the encoder.

3.5 Pseudorandom Number Generator

Theoretically, it is impossible to generate a random sequence in a digital computer; yet it is possible to generate sequence of numbers with very large period and fair randomness. The random sequences we need in this simulation are a uniform random sequence, a Gaussian random sequence, and an exponential random sequence. The latter two sequences are obtained from the first one. In the uniform random sequence generator, we use the multiplicative congruential method [1].

3.6 Flow Diagram of Program

The whole flow diagram of the program is sketched in Figure 3.1. This diagram shows the procedure for one data bit only.

There are two sources for the data needed in this program: INPUT and BLOCK DATA. The content of each source is as follows:

INPUT: Initial seed for random number generator, E_b/N_0, step size, tracked phase and symbol rate.

BLOCK DATA: Pulse rate, pulse duration, the distribution of each kind of pulse, the power level of each kind of pulse.

4. Results Compared with Those of Analytical RFI Program

In this section we present some results. We present a comparison of results from the Monte Carlo program and the analytical RFI program that shows two things: one, that under conditions where interleaving is not needed the two programs give results that are very close, which tends to validate both programs; and, two, that under some conditions where interleaving is not currently used in TDRSS, interleaving would improve the bit error rate (BER). We also give some analytical upper bounds to the BER, which when compared to the programs' results also tend to validate the programs.

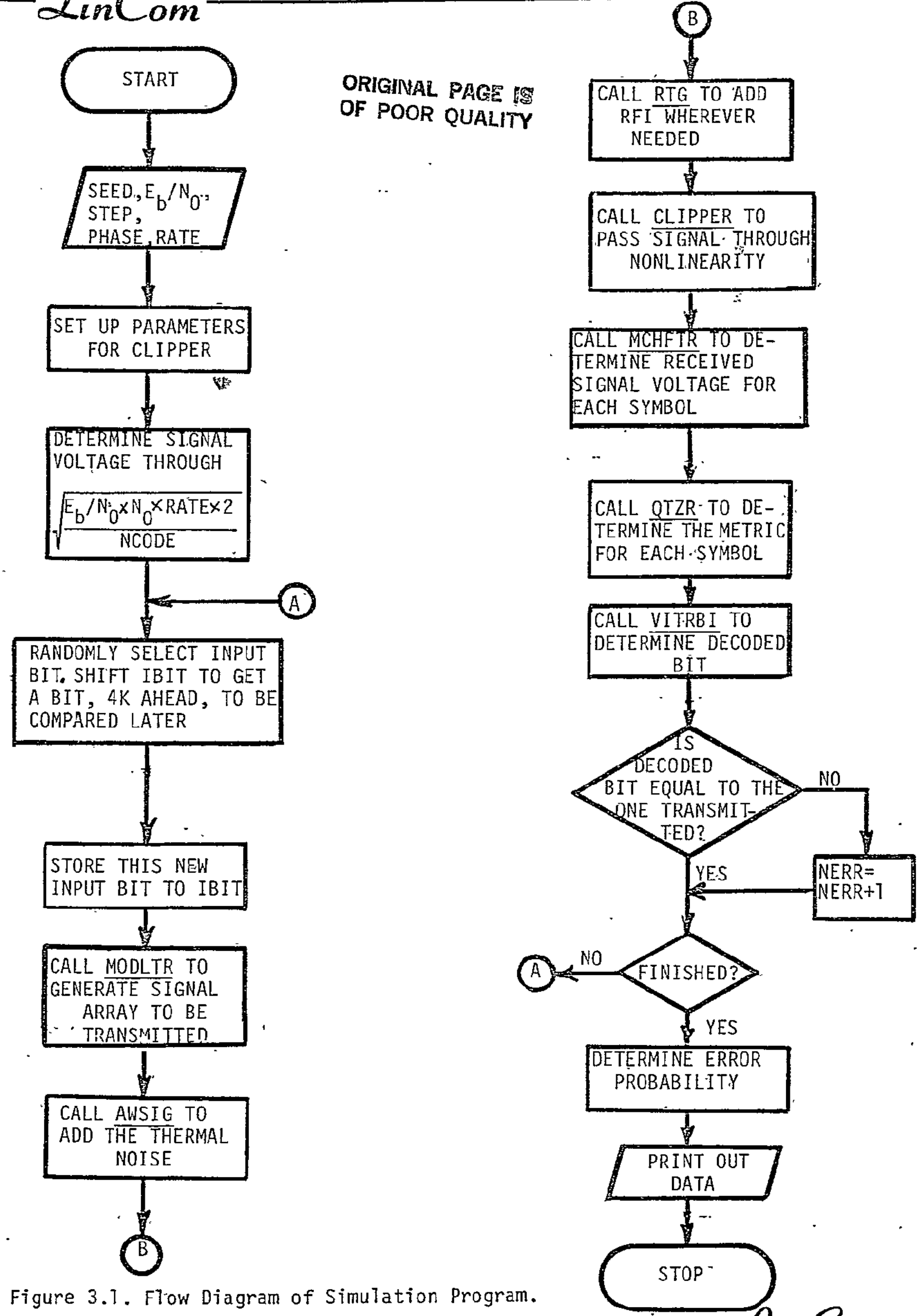

Figure 3.1. Flow Diagram of Simulation Program.

The results we present are in terms of five BER values.

The first is the BER computed by the analytical program.

The second is the BER computed by the Monte Carlo simulation program.

Now, in the analytical RFI program the distribution of the eight-level-quantized matched-filter output is computed, from which the cutoff rate R_0 [2] is computed. The BER is then computed from R_0 through an empirical formula which is derived from the Gaussian channel assumption. A result shown in [2] is that for a general channel the coded bit error rate can be decoupled into two factors. One of them is the cutoff rate R_0 and the other one is a function B(.). R_0 is cmputed from the channel statistics and B(.), which is determined solely by the specific code, is a function to compute the BER from R_0. The empirical formula used in the analytical program is indeed this B(.). In order to check the validity of the BER computation in the analytical program, given the distribution of the matched-filter output, the third quantity presented is the BER based on the matched-filter output distribution but then computed as it would be in the analytical program.

The fourth and fifth values presented are upper bounds on BER which are good for any memoryless channel. They are the generating function bound, given in [2]. They are both computed as follows:

$$\text{BER} \leqslant \frac{1}{2}[36D^{10}+211D^{12}+1404D^{14}+11633D^{6}+\ldots]$$

$$D = \sum_{i=1}^{8} \sqrt{\Pr(\ell_i|0)\Pr(\ell_i|1)}$$

where ℓ_i is the i-th quantization level of the matched-filter output.

The fourth quantity is calculated from the distribution of the matched-filter output obtained in the Monte Carlo simulation and the fifth quantity is calculated from the distribution found by the analytical program.

For the sake of brevity, we define the following notation for the five quantities about to be presented:

BER1 = error rate of analytic RFI program.

BER2 = error rate obtained from the simulation.

BER3 = error rate computed with the empirical formula B(.) used in analytical program form the distribution obtained from the simulation.

BER4 = the generating function bound calculated from channel statistics obtained from the simulation.

BER5 = the generating function bound calculated from channel statistics obtained from the analytical program.

The error rates are tabulated in Table 4.1 and Table 4.2, which are for RFI pulse durations of 5 μsec and 2 μsec, respectively. Both tables have the same E_b/N_0 (6 dB) and same total RFI duty cycle (53%). The ratios of RFI pulse duration to symbol duration are also included in the tables.

From these tabulated data, we can make the following observations, where σ is defined as the ratio of RFI pulse duration to symbol duration:

(1) When $\sigma \leq 0.4$, the results of the simulation and the analytical RFI program are essentially identical. This is because interleaving is not needed. The generating function bound is conservative although it is still a valid bound.

Table 4.1. The BER's for Different Data Rates.
E_b/N_0 = 6 dB, Total RFI Duty Cycle = 53%.
RFI Pulse Duration = 5 μs.

BER / DATA RATE	BER1	BER2	BER3	BER4	BER5	PULSE DURATION / SYMBOL DURATION
150K	6.668E-4	--	--	--	3.344E-3	1.5
75K	3.583E-4	1.067E-3	4.970E-4	2.458E-3	1.750E-3	0.75
50K	2.964E-4	8.004E-4	3.679E-4	1.798E-3	--	0.5

Table 4.2. The BER's for Different Data Rates.
E_b/N_0 = 6dB, Total RFI Duty Cycle = 53%
RFI Pulse Duration = 2 μs

BER / DATA RATE	BER1	BER2	BER3	BER4	BER5	PULSE DURATION / SYMBOL DURATION
150K	8.520E-4	2.023E-3	1.069E-3	5.527E-3	4.344E-3	0.6
75K	9.300E-4	1.032E-3	1.021E-3	5.264E-3	--	0.4
50K	1.000E-3	1.170E-3	1.367E-3	7.702E-3	--	0.2

Notes:

(1) The values obtained in both tables are with the parameter values in the clipper. They are as follows. AMPMSF = 1.2 dB, ALPH1 = .9 dB, ALPH2 = 0.1 dB, SGPDB = -0.3 dB.

(2) The blanks (with --) mean irrelevant to our results.

(2) For larger σ (say larger than .75), the bit error rate obtained form the analytical program is less than the simulation predicts. This is expected, since the analytical program assumes ideal interleaving while the simulation uses no interleaving.

The first observation suggests the following. For an RFI pulse duration of 5 μsec, for data rates below 40 K bits per second no interleaver is needed. For the case of 2 μs, this critical rate is 100 K bits per second.

The second observation can be interpreted as follows. The channel statistic (cutoff rate R_0 or D) does not reflect the degree of correlation in the channel. As mentioned earlier, the empirical function B(.) is obtained from the additive-white-Gaussian, memoryless channel. For a σ larger than about .75, adjacent symbols into the decoder are not independent. Thus B(.) becomes not a good formula. On the other hand, the generating function bound is a union bound of all possible error paths in the trellis diagram [3]. This generating function bound is insensitive to the memory in the channel since it has included all possible error paths. Our second observation is consistent with the above argument as σ becomes large, the discrepancy of adjacent symbols becomes greater and hence B(.) becomes not a good approximation while the generating function bound becomes closer to the actual value.

REFERENCES

[ ] D. E. Knuth, The Art of Computer Programming Seminumerical Algorithms, Vol. 2, 2nd Ed., Addison-Wesley, Massachusetts, 1981.

[ ] J. K. Omura, and B. K. Levitt, "Coded Error Probabilty for Antijam Communication Systems," IEEE Trans. on Comm., Vol. COM-30, No. 5, pp. 896-903, May 1982.

[ ] A. J. Viterbi and J. K. Omura, Prnciples of Digital Communications and Coding, McGraw-Hill, New York, 1979.

4.4 RFI EFFECT ON SYNCHRONIZATION AND DOPPLER TRACKING

1. Introduction

The RFI will affect the performance of the synchronizers and the Doppler tracking system in the TDRSS ground station. We predict that in general the effect will be small because the signal EIRP will be increased above what is required to achieve nominal performance without RFI. The TDRS clippers for the S-band links work well to minimize the RFI impact.

The sections that follow are these. Section 2 analyzes the RFI impact on the rms phase error and cycle slip rate of both the carrier tracking loops and symbol synchronizers. Section 3 describes how the RFI effect on Doppler tracking is modeled.

2. Rms Phase Error and Cycle Slip Rate of Carrier Tracking Loop and Symbol Synchronizer for Shuttle/TDRSS Links with RFI

2.1 Introduction

The analysis described herein provides the rms tracking error and mean time between cycle slipping events for boht the carrier loops and symbol synchornizers for the Shuttle/TDRSS S-band and Ku-band return links with RFI present. In Section 2.2 we breifly describe the computation of the statistics in the absence of RFI. Then in Sections 2.3 and 2.4 we present models for the RFI effect in the high- and low-symbol rate cases, respectively. If the average RFI pulse duration is less than half the correlation time of the arm fitler, then the low-rate model is to be used. It has been found that the exact cut-off rate between the two models is not important. The low- and high-rate models are so different that they need to be discussed separately.

2.2 No-RFI Model

In the no-RFI model for the tracking performance of the carrier loop or symbol synchronizer, first the derivative $S'(0)$ at zero of the loop S-curve, the one-sided power spectral density N_0 of the equivalent noise, and the S-curve as a function of phase error are obtained. Then the loop tracking error variance σ_λ^2 is given by

$$\sigma_\lambda^2 = N_0 B_L / (S'(0))^2 \tag{1}$$

where λ is phase in radians for the carrier loop and is timing error in units of symbol duration for the symbol sync and where B_L is the one-sided loop bandwidth. The average time $\tilde{T}$ between cycle slips is given for a first-order loop by [1]

$$\tilde{T} = \frac{1}{4B_L\sigma_\lambda^2}\int_0^{\lambda_p} dx \int_x^{\lambda_p} dy \, \exp\left(\frac{1}{\sigma_\lambda^2}\int_x^y \frac{S(z)}{S'(0)}\, dz\right) \tag{2}$$

where λ_p is the period of the S-curve. $\tilde{T}$ can also be written

$$\tilde{T} = \frac{\rho}{4B_L}\int_0^{2\pi} dx \int_x^{2\pi} dy \, \exp\left(\rho \int_x^y \frac{2\pi}{\lambda_p S'(0)}\, S\left(\frac{\lambda_p}{2\pi} z\right) dz\right) \tag{3}$$

where

$$\rho = \text{loop SNR} = \frac{1}{\sigma_\lambda^2 (2\pi/\lambda_p)^2} \tag{4}$$

For the same value of σ_λ^2 for the carrier loops and symbol syncs, the loop SNR will be greater for the carrier loop by a factor of π^2.

2.3 High-Symbol-Rate Model with RFI

In the high-rate model with RFI the loop's arm filter(s) is (are) Assumed to do no averaging of RFI conditions. Thus, during a pulse of RFI, we may assume that $S'(0)$, N_0, and $S(\lambda)$ take on values conditioned on the particular type of RFI. This is because for the symbol rates treated here, the RFI pulse durations are comparable to or larger than the symbol duration. The loop's arm filter(s) has (have) bandwidth comparable to the symbol rate, so at input to the loop filters little averaging over RFI/no-RFI conditions has occurred.

Thus, for a given time interval where a particular sequence of RFI pulses occurs, $S'(0)$, N_0, and $S(\lambda)$ may be computed as the sum of conditional values and from them σ_λ^2 and $1/\tilde{T}$ may be calculated. It can be observed in experimental results [2] that the time between the start and completion of the first cycle slip in a slipping event of a second-order loop is close to $2/B_L$. For this reason, σ_λ^2 and $1/\tilde{T}$ are computed for a whole set of possible RFI conditions in $2/B_L$ and then weighted with probability of occurrence and summed to yield unconditional σ_λ^2 and $1/\tilde{T}$.

A set of possible RFI conditions in $2/B_L$, instead of just one average condition, is treated because the slip rate is related to loop SNR ρ in a highly nonlinear way and it is thought that the relatively rare occurrence of many more than the average number of pulses in $2/B_L$ may be more important to the slip rate than the much more common occurrence of a nearly average number of pulses.

The set of conditions in $2/B_L$ is obtained as follows. The less powerful half (in duty cycle) of the RFI is assumed to occur at its average rate without pulse overlap. The rest of the RFI is treated as one Poisson process with pulse duration τ equal to the average in the group, pulse arrival rate μ equal to the sum, and power equal to first the least value in the group and then the greatest value. (Two values of each of σ_λ^2 and $1/\tilde{T}$ can thus be calculated which roughly bound the actual values.) It is well known that the probability of there being N pulses of the combination bad RFI processes in $2/B_L$ is given by, since $\tau << 2/B_L$,

$$P(N) = e^{-\mu 2/B_L}(\mu 2/B_L)^N/N! \tag{5}$$

Now, given that there are N pulses, the fraction of $2/B_L$ on which the bad RFI is present must be computed. Since overlaps may occur, the fraction is properly described by a probability distribution, but we will just use its average value. To calculate it, consider the random process I defined on 0 to $2/B_L$ by

$$I(t) = \begin{cases} 0 & \text{if there is no pulse occurring at } t \\ 1 & \text{otherwise} \end{cases} \tag{6}$$

Then the arrival times T_i, $i=1,\ldots,N$, of the pulses are independent and uniformly distributed on 0 to $2/B_L$. So

$$\begin{aligned} Pr(I(t)=0)) &= Pr(|t-T_i| > \tau/2 \text{ for all } i=1,\ldots,N) \\ &= [Pr(|t-T_1| > \tau/2)]^N \\ &= \left(1 - \frac{\tau}{2/B_L}\right)^N \end{aligned} \tag{7}$$

The average fraction of the time during which bad RFI occurs is then

$$EI(t) = 1 \cdot Pr(I(t)=1) = 1 - \left(1 - \frac{\tau}{2/B_L}\right)^N \qquad (8)$$

It is assumed that the less powerful half of the RFI and the bad RFI do not overlap in time, a somewhat pessimistic assumption.

A variation of the high-rate model is used when the arm filters do no averaging of RFI conditions and the average number of RFI pulses arriving in twice the inverse of the loop bandwidth is large. Then all the RFI processes are assumed to arrive at their average rate.

2.4 Low-Symbol-Rate Model with RFI

In the low-rate model it is assumed that the loop's arm filter(s) averages the RFI conditions. The average signal power and noise level during the no-RFI condition and all the RFI processes are obtained, weighted by duty cycle, and summed. In this way, the averaging effect of the arm filters is approximated. The rms phase error and cycle-slippling-event rate are computed for the appropriate loop, the latter being based on the loop S-curve and phase jitter.

3. RFI Effect on Doppler Tracking

3.1 Introduction

The Doppler estimate is derived in the TDRSS ground station from the carrier tracking loop by integrating the recovered carrier frequency over the Doppler count time τ and dividing the result by τ. The RFI contribution to the Doppler estimation error can, therefore, be broken into two components:

(1) The difference between the RFI-induced phase error at the beginning and end of the Doppler count interval.

(2) The net number of RFI-induced cycle slips (number of clockwise cycle slips minus number of counterclockwise cycle slips) during the Doppler count interval.

These two components will be assessed separately below.

3.2 Phase Error Component of Doppler Error

Since the Doppler count interval is many orders of magnitude longer than the RFI pulses and also considerably longer than the inverse of the carrier tracking loop bandwidth, the phase error at the beginning and end of the Doppler count interval can be treated as independent, identically distributed random variables. Denoting the RFI contribution to the carrier tracking error variance by σ_R^2 the contribution to the variance of the Doppler frequency estimate is given by

$$\sigma_1^2 = \frac{2\sigma_R^2}{(2\pi)^2\tau} \quad [\mathrm{Hz}^2]$$

3.3 Cycle Slip Component of Doppler Error

Denoting the RFI induced cycle slip rate by N^+ and N^- for clockwise and counterclockwise slips, respectively, and assuming that positive and negative cycle slips are independent random events with Poisson statistics the RFI induced cycle slip contribution to the variance of the Doppler estimate is given by

$$\sigma_\tau^2 = \frac{N^+ + N^-}{\tau} \; [\mathrm{Hz}^2]$$

In addition, there is a contribution to the systematic Doppler error of

$$\mu_\tau = N^+ - N^- x \tau \; [\mathrm{Hz}]$$

REFERENCES

1. Viterbi, A. J., Principles of Coherent Communications, McGraw-Hill, 1966.

2. Ascheid, G., and Meyr, H., "Cycle Slips in Phase Locked Loops: A Tutorial Survey," to be published in IEEE Transactions on Communications (Special Issue on Phase Locked Loops), October 1982.

5. SHUTTLE/TDRSS ACQUISITION ANALYSES

5.1 INTRODUCTION

This chapter documents the work performed under Task #5, which requires analytical simulation models for the processes of antenna pointing and PN-code, carrier, and clock acquisition for the Shuttle/TDRSS links. Such a package was developed, that can predict the acquisition performance of the subsystems and also of the entire link. Due to lack of information on the Ku-band receivers, only the S-band receivers were modeled. It is likely that some of the subsystems in the Ku-band receivers are like those in the S-band receivers, in which case at least a partial Ku-band model would exist as soon as parameter values could be obtained. Section 5.2 presents a description of the package and some sample outputs of it.

5.2 MODEL OF SHUTTLE/TDRSS LINK ACQUISITION PERFORMANCE

1. Introduction

This report describes the analytical simulation model of the performance of the TDRSS/Shuttle link acquisition that has been developed. It also provides some sample outputs of the program.

In the total link acquisition, several systems must acquire, drawn from the following: Ku-band autotrack, PN code, carrier, bit synchronizer, ambiguity resolver, etc. Models were developed to describe the probability density function (pdf) of each of these systems except Ku-band autotrack. We assume that these acquisition systems are independent of each other. Thus the total receiver acquisition time is the sum of the acuqisition times of the individual systems and the pdf of the total receiver acquisition time is the convolution of the pdf's of the various acquisition systems involved.

In the following sections, we give descriptions of the analytical models of the Shuttle/TDRSS acquisition systems and some performance predictions in terms of the acquisition time pdf for various link conditions. Only the S-band links are treated because of insufficient information on the Ku-band forward-link PN-code acquisition system and all the Ku-band return-link acquisition systems. Sections 2 and 3 present the models of forward- and return-link acquisition. Section 4 presents some typical results.

2. Forward Link Acquisition

Shuttle forward link acquisition can be divided into two parts: carrier acquisition and PN-code acquisition. Both of these acquisition systems are individually modeled. Assuming that they are statistically independent, the total acquisition time pdf is the convolution of the pdf's of the two acquisition systems. It is possible that the forward link will not be PN-code modulated. In this case, only the carrier acquisition is required of the total acquisition. The bit sync acqusition time is relatively small so that it is neglected in the following analysis.

2.1 PN-Code Acquisition Time Pdf

As described in [1], the PN acquisition algorithm of the Shuttle forward link is that of the fixed double dwell time system. Analysis on the double dwell time system is partly available in [1] in the form of the mean acquisition time but the complete statistical analysis is not available in the literature. For single dwell-time systems, the complete statistical analysis is available in [9]. However, the computation involved is prohibitively complex. A simpler, approximate algorithm was suggested by W. R. Braun [10]. We first show some analogy between the single dwell time and the double dwell time systems and then utilize Braun's simplifying approach to obtain the acquisition time pdf for the double dwell time system.

The double dwell time system can be considered as a special case of the single dwell time system so that existing analysis on the single dwell time can be utilized for the double dwell time.

Let us set τ_1 = first dwell time, τ_2 = second dwell time, $_3$ = penalty time for false alarm, α_1 = first false alarm rate, and α_2 = second false alarm rate. Let us define further notations.

T_{00} = dwell time for correct dismissal

T_{01} = dwell time for false dismissal

T_{10} = dwell time for false alarm

T_{11} = dwell time for correct detection

V_1 = variance of correct dismissal time

V_2 = variance of false alarm time

Then the statistics of the four mean dwell times T_{00}, T_{01}, T_{10}, T_{11} and variances V_1, V_2 can be obtained from the pdf of the dwell times.

For exaple, T_{01} can be represented as in Figure 1, form which we obtain

$$E[T_{01}] = (1-\alpha_1)\tau_1 + \alpha_1(\tau_1+\tau_2+\tau_3)$$

$$= \tau_1 + \alpha_1(\tau_2+\tau_3)$$

and

$$\mathrm{Var}[T_{01}] = V_2$$

$$= (\tau_1-E[T_{01}])^2(1-\alpha_1)+(\tau_1+\tau_2+\tau_3-E[T_{01}])^2\alpha_1$$

In the same way, we can write for T_{10}

$$E[T_{10}] = (1-\beta_1)\tau_1 + \beta_1(\tau_1+\tau_2) = \tau_1 + \beta_1\tau_2$$

and for T_{00}

$$E[T_{00}] = (1-\alpha_1)\tau_1 + \alpha_1(\tau_1+\tau_2) = \tau_1 + \alpha_1\tau_2$$

and finally for T_{11} we merely let

$$E[T_{11}] = \tau_1$$

because for correct detection, we spend only the time τ_1.

The equivalent false alarm probability is set to $\alpha = \alpha_2$ and the equivalent detection probability P_D is set to $P_D = P_{D1}*P_{D2}*P_{SW}$ where P_{D1} is the detection probability of the first dwell time, P_{D2} is the detection probability of the second dwell time and P_{SW} is the switch-over probability to tracking mode which is also discussed in [1].

2.2 Carrier Acquisition Time Pdf

Shuttle forward link carrier acquisition is done by carrier frequency sweep [2]. For sweep acquisition, a finite probability of correct acquisition is associated with the sweep rate R in relation to the loop natural frequency ω_n^2 and loop SNR.

In his classical paper, Viterbi [5] has shown that under no-noise conditions, the acquisition probability is 100% for $R < \frac{1}{2}\omega_n^2$ and decreases fast for $R \geq \frac{1}{2}\omega_n^2$, reaching zero at $R = \omega_n^2$.

Frazier further assumed that under finite SNR, the sweep rate should be reduced for 90% acquiistion probability as given by

$$R_{0.9} = \omega_n^2(1 - (SNR)^{-1/2})$$

Gardner's proposition [7] is more conservative in that he claims

$$R_{0.9} = \frac{\omega_n^2}{2}(1 - 2(SNR)^{-1/2})$$

In view of these claims, we find that there is some discrepancy between researchers for the sweep acquisition probability calculations. Therefore, we felt that only a reasonable compromise between these results may approximately model sweep acquisition.

Our model is shown in Figure 2, where $R_{0.9}$ is given by

$$R_{0.9} = \omega_n^2(1- 2(SNR)^{-1/2})$$

For a given sweep rate, the probability of successful acquisiiton P can be obtained from Figure 2. If acquisition is not successful at the first trial, it must be repeated. Therefore the acquisition time pdf will be given in a form shown in Figure 3, where T is the time taken for a complete sweep and is given by

$$T = \frac{2\Delta\omega_{max}}{R}$$

where $\Delta\omega_{max}$ is the maximum frequency difference in radians. When the integral of the pdf up to nT is more than 0.99, it is truncated at that point to avoid a pdf which is non-zero on an infinite interval, which is impossible to handle numerically.

3. Return Link Acquisition

The Shuttle S-band return link has three modes of operation. For mode 1 and mode 2, the data is BPSK modulated and for mode 3, the carrier is sent unmodulated. PN modulation is not superimposed on any of the modes. For mode 1 and mode 2, total acquisition time is modeled as the sum of carrier acquisition, bit sync acquisition and ambiguity resolution times. For mode 3, only carrier acquisition time is appropriate as there is no data modulation [2]. Again the total acquisition time pdf is obtained as the convolution of the pdf's of the acquisition times of these individual systems.

3.1 Carrier Acquisition Time Pdf

For mode 1 and mode 2, the carrier self-acquires. Analysis of self-acquisition (pull-in) behavior has some theoretical difficulties and only for a limited case is the result available.

Perhaps one of the most reasonable equations of pull-in is the following [8]:

$$T_{ACQ} = \frac{\pi(\Delta\omega)^2}{2\xi\omega_n^3\int_{-\pi}^{\pi} g^2(\phi)\,d\phi}$$

for the arbitrary phase detector charcteristics $g(\phi)$.

For a sinusoidal phase detector and a second order lead-lag type loop with damping factor $\xi = 0.707$, we have the more simplified equation [7]

$$T_{ACQ} = \frac{4.2(\Delta f)^2}{(B_L)^3}$$

This equation is utilized in our program which we believe is adequate for most purposes. This equation is derived for the no-noise condition. Therefore, the effect of noise is considered using empirical results.

The initial frequency uncertainty is assumed to be uniformly distributed. Therefore the pdf of acquisition time shall have the transform given by the equation

$$y = ax^2$$

where x is the random variable with uniform distribution. This transformation is implemented in the program.

For mode 3, the carrier is acquired by sweeping. Therefore, the analysis that is done for the forward link sweep acquisition is directly applicable to this mode with only a change of parameters.

3.2 Bit Sync and Ambiguity Resolution

For the bit sync, the task of frequency acquisition can be neglected due to the fact that the bit rate bias due to Doppler is very small. Therefore, only phase acquisition of the bit sync is of importance.

From [11], the phase acquisition time T_p can be approximated by

$$T_p \simeq \frac{5}{W_L} \frac{r+1}{r}$$

where $r = (2\xi)^2$ and $\xi = 0.707$ is the loop damping factor. By substituting appropriate values of ξ and $W_L = 2B_L$, T_p can be readily obtained for mode 1 and mode 2.

For mode 1 and mode 2, the symbol format is biphase. Inherent to all bi-phase symbol sync is the tendency to achieve lock at mid-symbol transition with probability comparable to locking at the between-symbol (desired) transition. This uncertainty is resolved by the ambiguity resolution logic in the Shuttle received as described in [2].

The ambiguity resolution logic takes a fixed number of bit durations to check for the transition probabilities. This amount of time is the acquisition time. Therefore, the ambiguity resolution time T_R can be expressed as

$$T_R = \frac{\text{Number of Bit Durations for Ambiguity Resolution}}{\text{Bit Rate}}$$

The T_R calculation is implemented for mode 1 and mode 2.

4. Typical Results

Typical numerical results on acquisition statistics are shown in this section for both forward and return link acquisition. Parameter values used are also shown below to identify the results.

4.1 Forward Link

Parameters for PN Acquisition

Doppler Chip Bias = 200 chip/sec

$\tau_1 = 547\ \mu\text{sec}$

$\tau_2 = 12.6$ msec

$\tau_3 = 62.5$ msec

$\alpha_1 = 0.03$

$\alpha_2 = 0.05$

CNR loss in the acquisition circuit = 7.7 dB

Parameters for Carrier Acquisition

Maximum carrier frequency deviation = 50 KHz

Sweep rate = 40 KHz/sec (LinCom estimate)

$B_L = 600$ Hz

$\omega_n^2 = (B_L{*}1.8857)^2 = 1280111\ \text{rad/sec}^2$ (LinCom Estimate)

Acquisition Performance

Forward link acquisition statistics are obtained in Figure 4 to 9. Figures 4, 5 and 6 are for mode 1 and Figures 7, 8 and 9 are for mode 2. Figures 5 and 8 are for nominal EIRP condition and other Figures are for ±2 dB EIRP variations.

From these figures, it is clear that the acquisition time decreases as the signal EIRP increases. Note also that mode 2 has a smaller mean acquisition time at nominal EIRP because it has higher C/N_0. These results can be compared to the acuqisition time specification [3] which is tabulated in Table 1. This indicates that our result is well below the specification.

4.2 Return Link

Parameters for Carrier Acquisition

$\omega_n^2 = 2\pi*45000$ rad/sec^2

sweep rate, R = 22.2475 KHz (mode 3)

max. freq. deviation, $\Delta f = \pm 50$ KHz (mode 1,2)

$= \pm 2.2$ KHz (mode 3)

loop BW, B_L = 28.8 KHz (mode 1,2)

= 112.5 Hz (mode 3)

Parameters for Bit Sync and Ambiguity Resolution

Number of bits for ambiguity resolution = 4096 bis.

Acquisition Time Performance

Return link acquisition statistics plots are given in Figures 10, 11 and 12 for mode 1, mode 2 and mode 3, respectively. The EIRP's used are the nominal EIRP. The results show that the received C/N_0 is sufficiently high to permit rapid acquisition.

For mode 1 and mode 2, fixed acquisition times such as the ambiguity resolution time and the phase acquisition time dominate the short carrier acquisition time so that the pdf curve shows an abrupt transition at the carrier acquisition.

These results can be compared to the predictions made in the SSDBS description [2]. If is found that the current acquisition time estimates based on the pdf give better and more detailed information than the previous result [2].

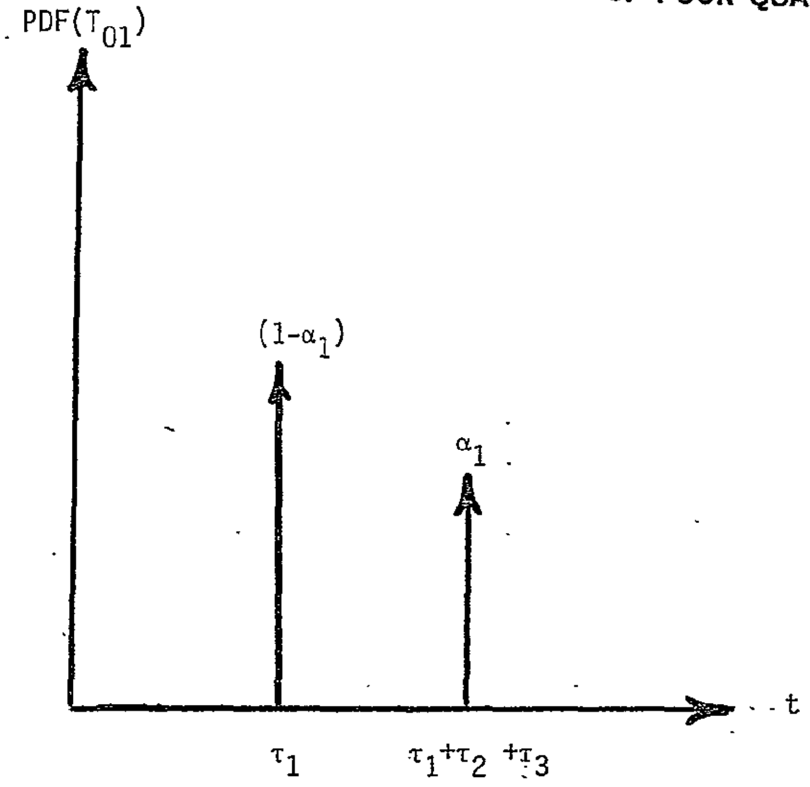

Figure 1. PDF of T_{01}.

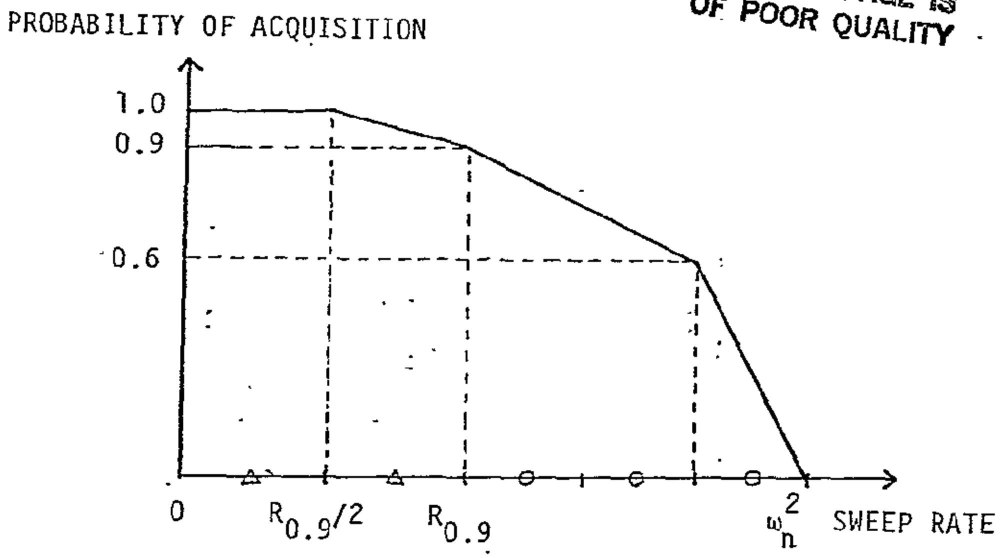

Figure 2. Acquisition Probability.

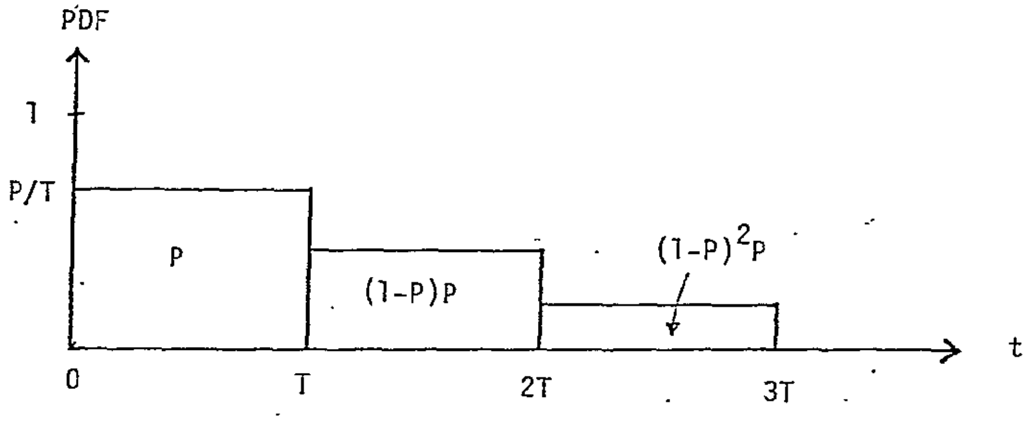

Figure 3. Acquisition Time PDF.

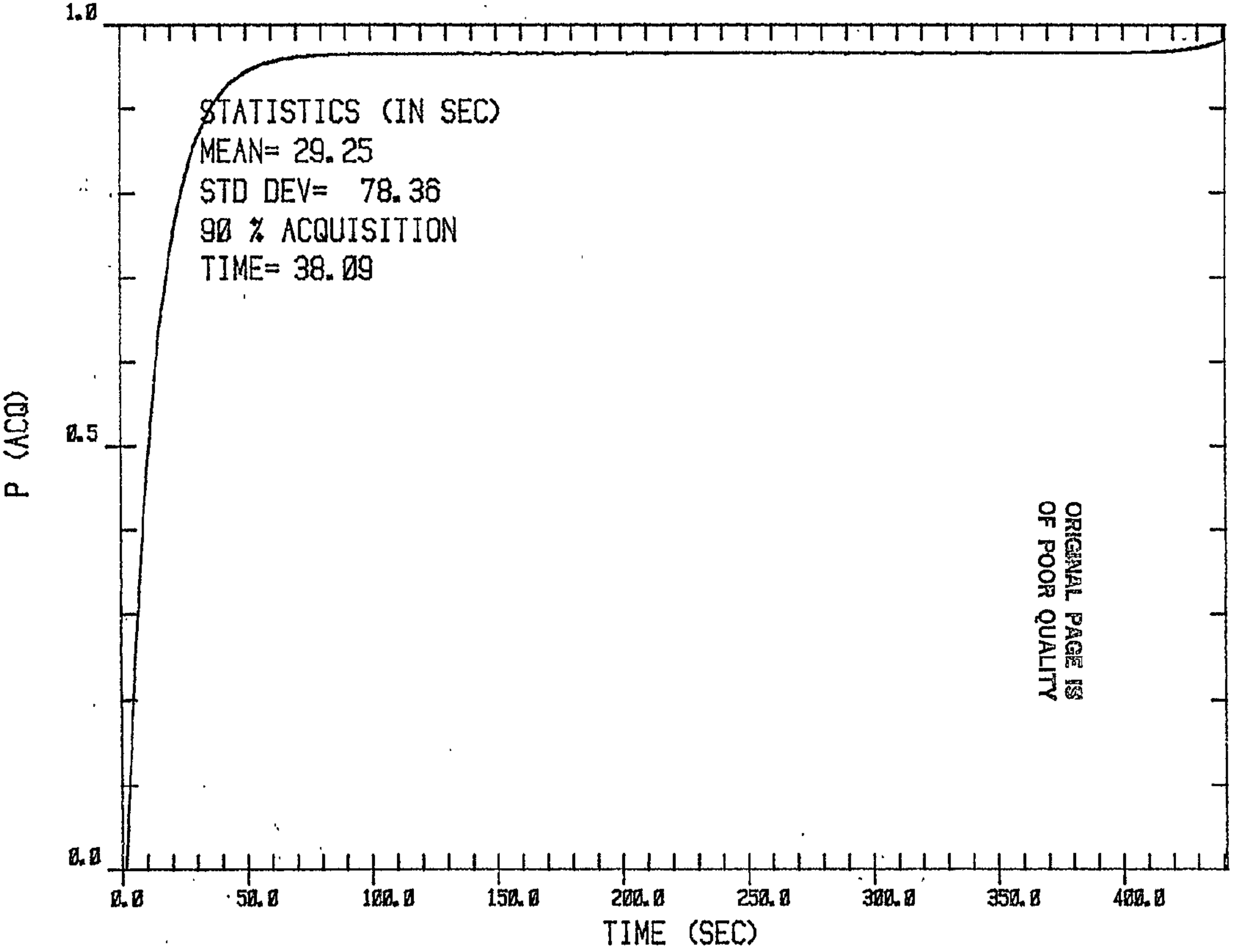

Figure 4. Acquisition-TIme Cumulative Pdf for Shuttle S-band Forward Link Mode 1 with C/N_0 = 50 dB-Hz.

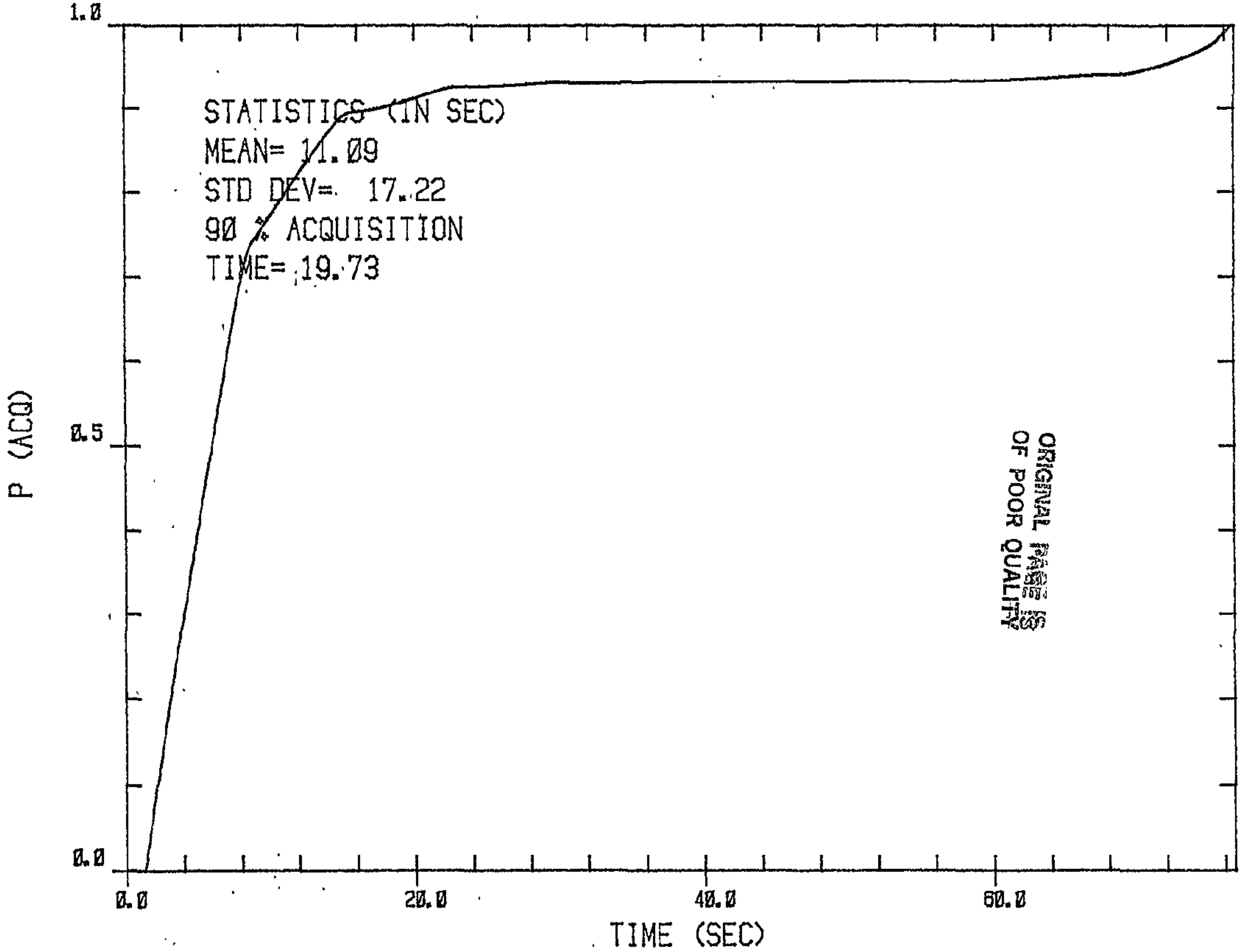

Figure 5. Acquisition-Time Cumulative Pdf for Shuttle S-band Forward Link Mode 1 with C/N_0 = 52 dB-Hz.

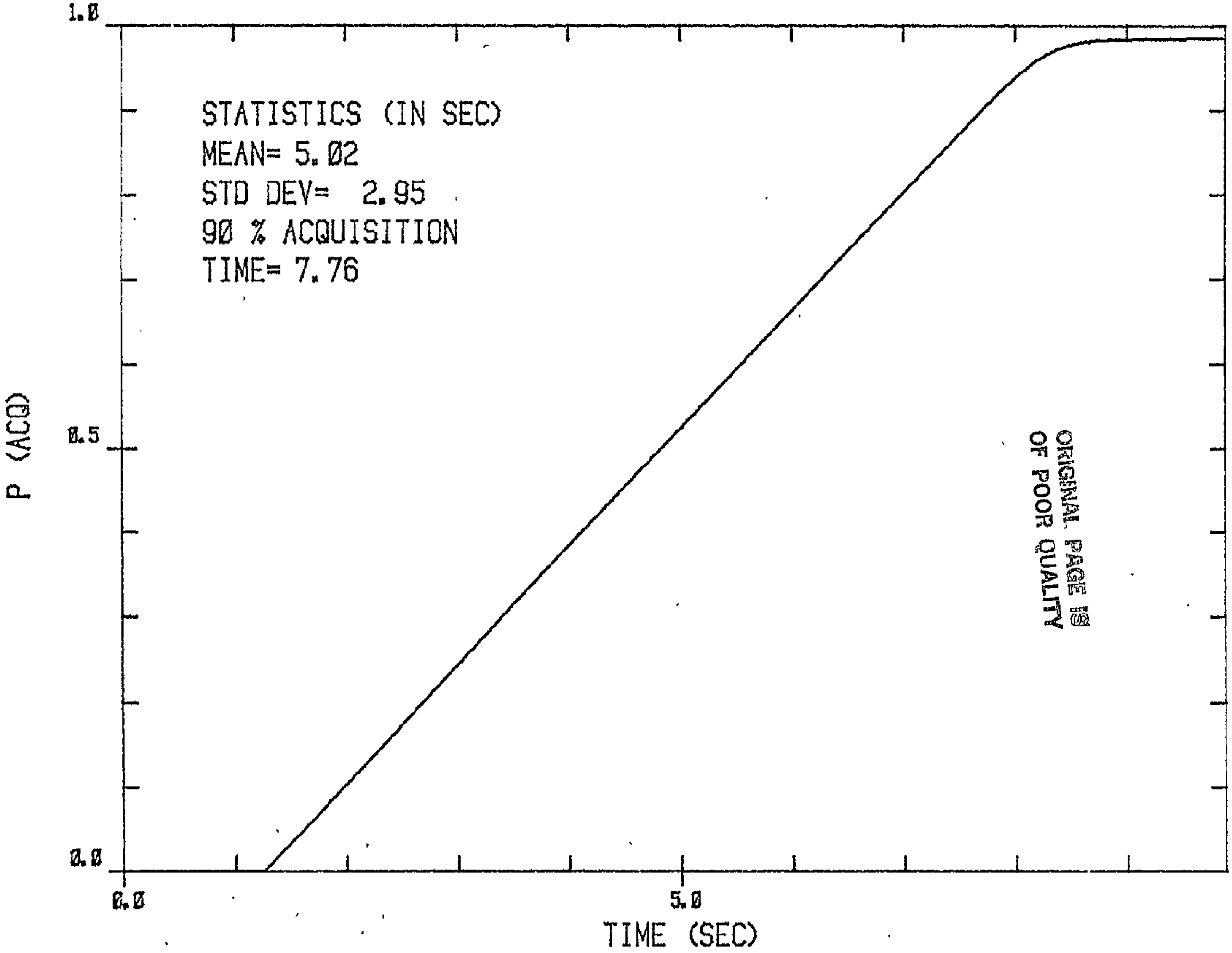

Figure 6. Acquisition-Time Cumulative Pdf for Shuttle S-band Forward Link Mode 1 with C/N_0 = 54 dB-Hz.

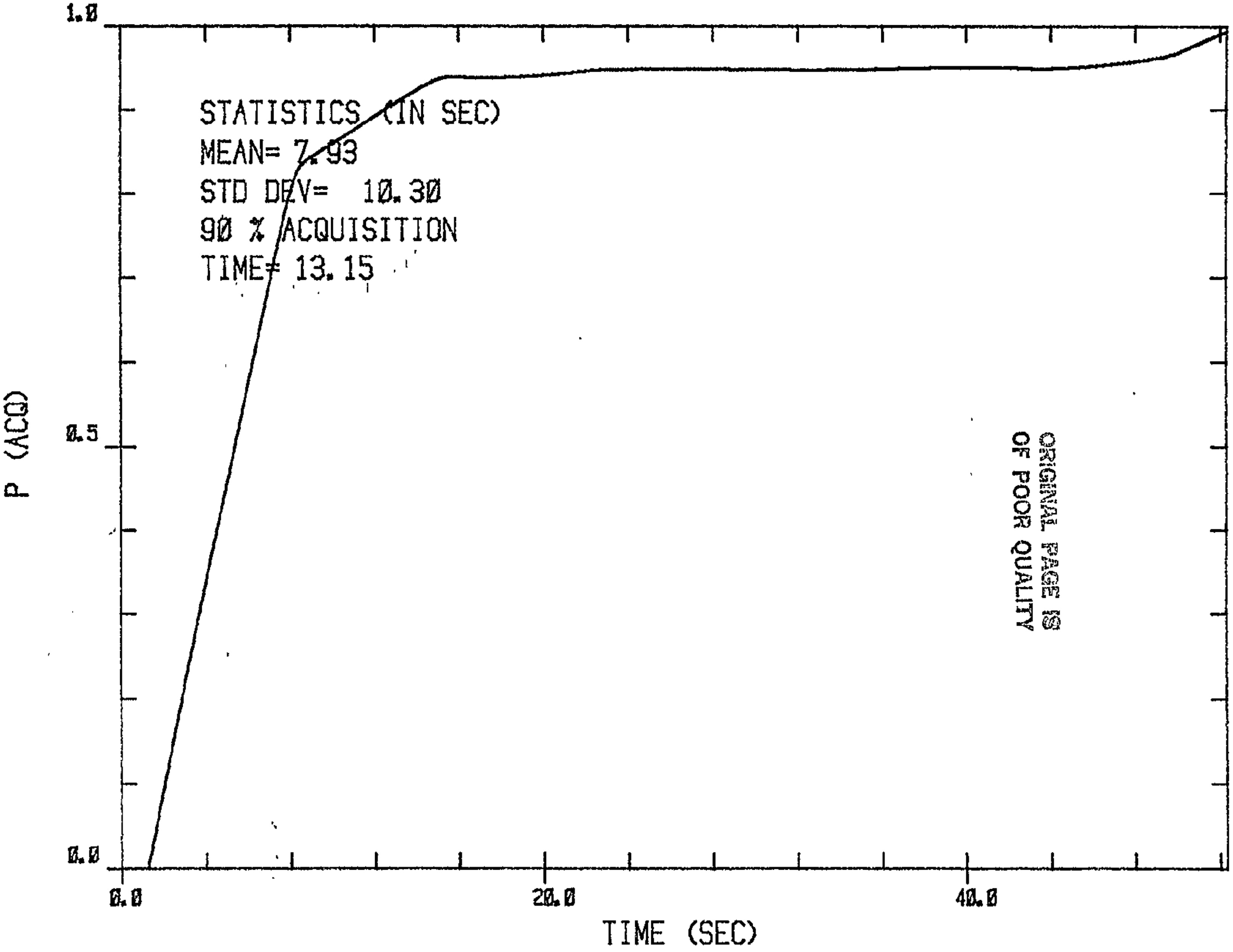

Figure 7. Acquisition-Time Cumulative Pdf for Shuttle S-Band Forward Link Mode 2 with C/N_0 = 53.5 dB-Hz.

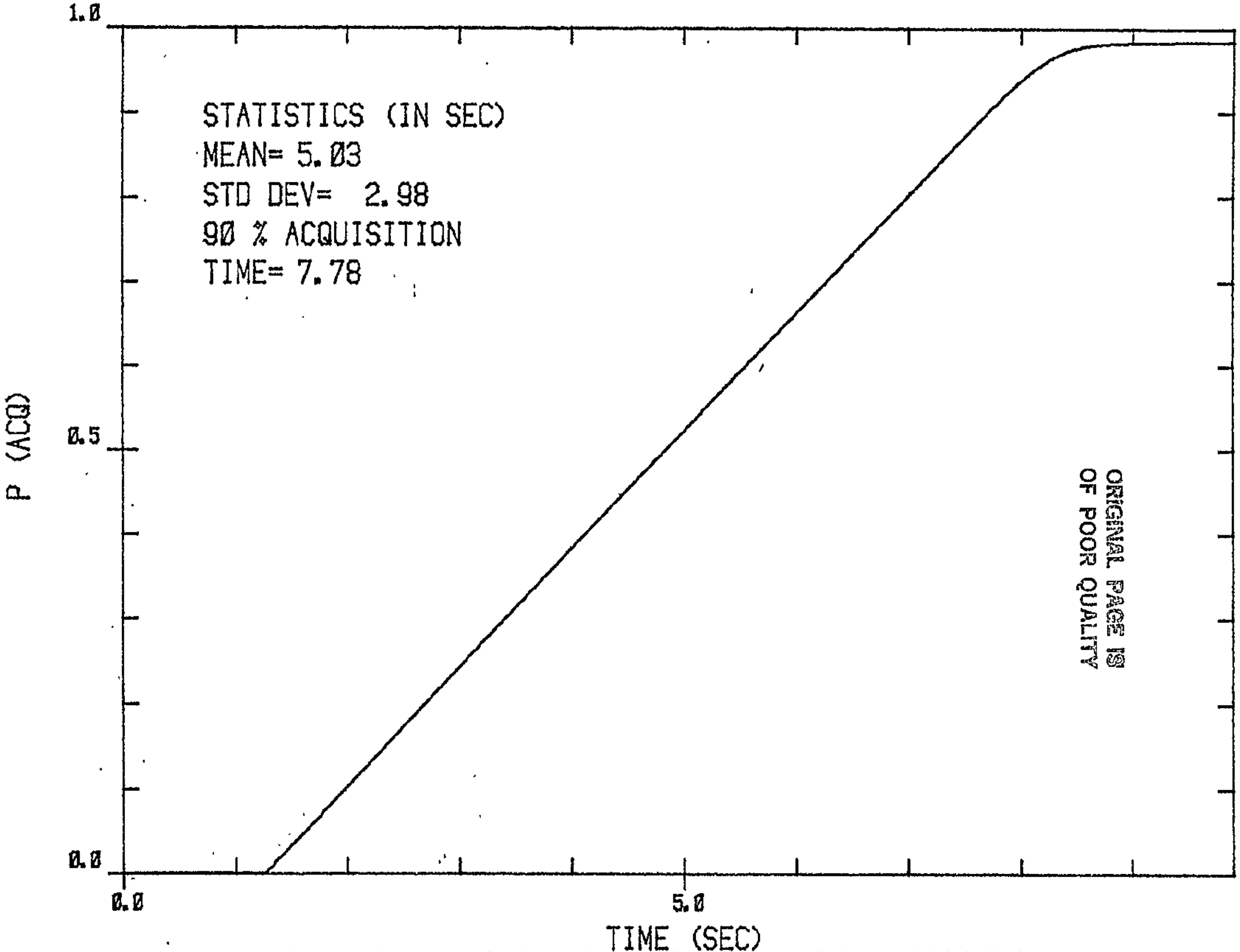

Figure 8. Acquisition-Time Cumulative Pdf for Shuttle S-Band Forward Link Mode 2 with C/N_0 = 55.5 dB-Hz.

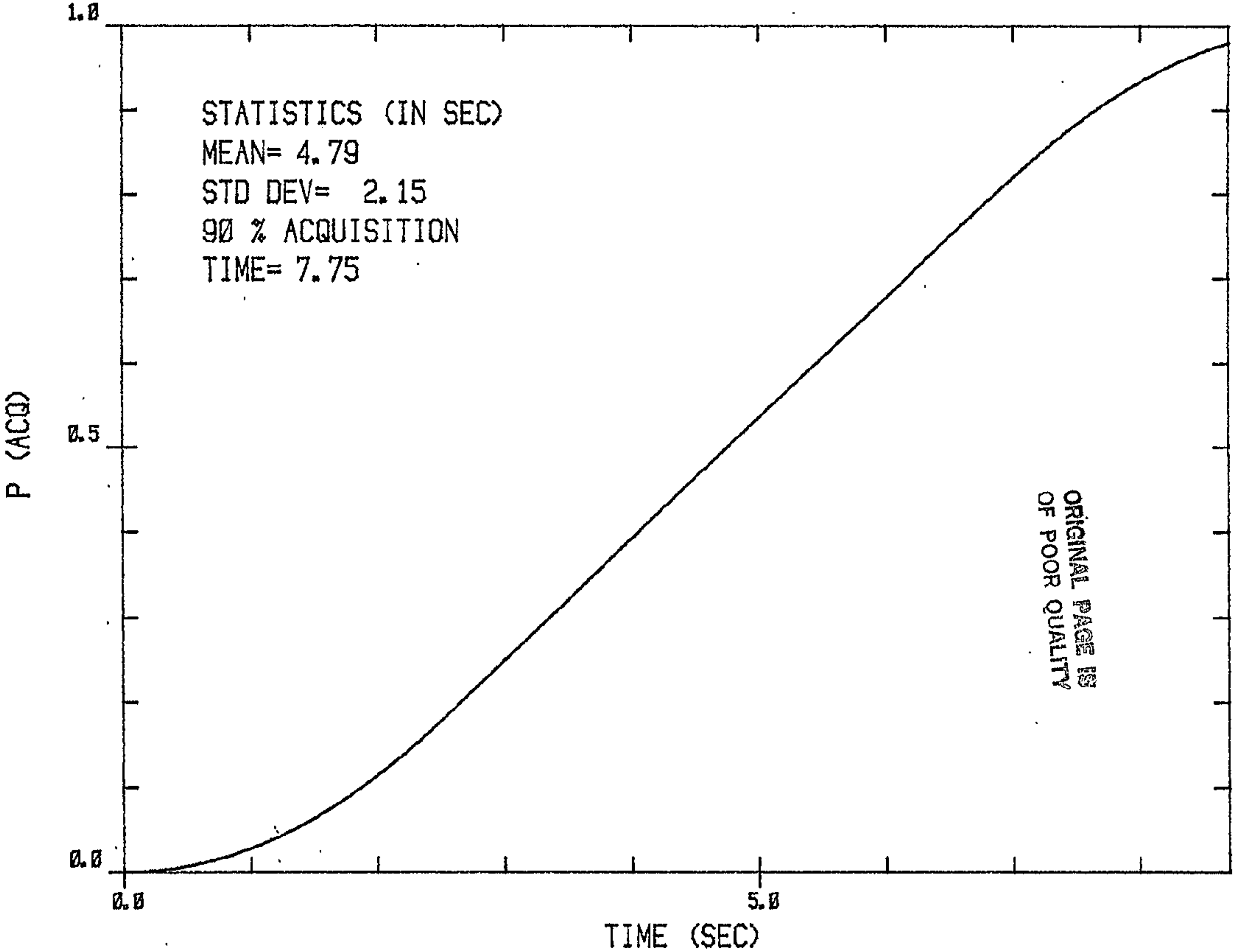

Figure 9. Acquisition-Time/Cumulative Pdf for Shuttle S-Band Forward Link Mode 2 with C/N_0 = 57.5 dB-Hz.

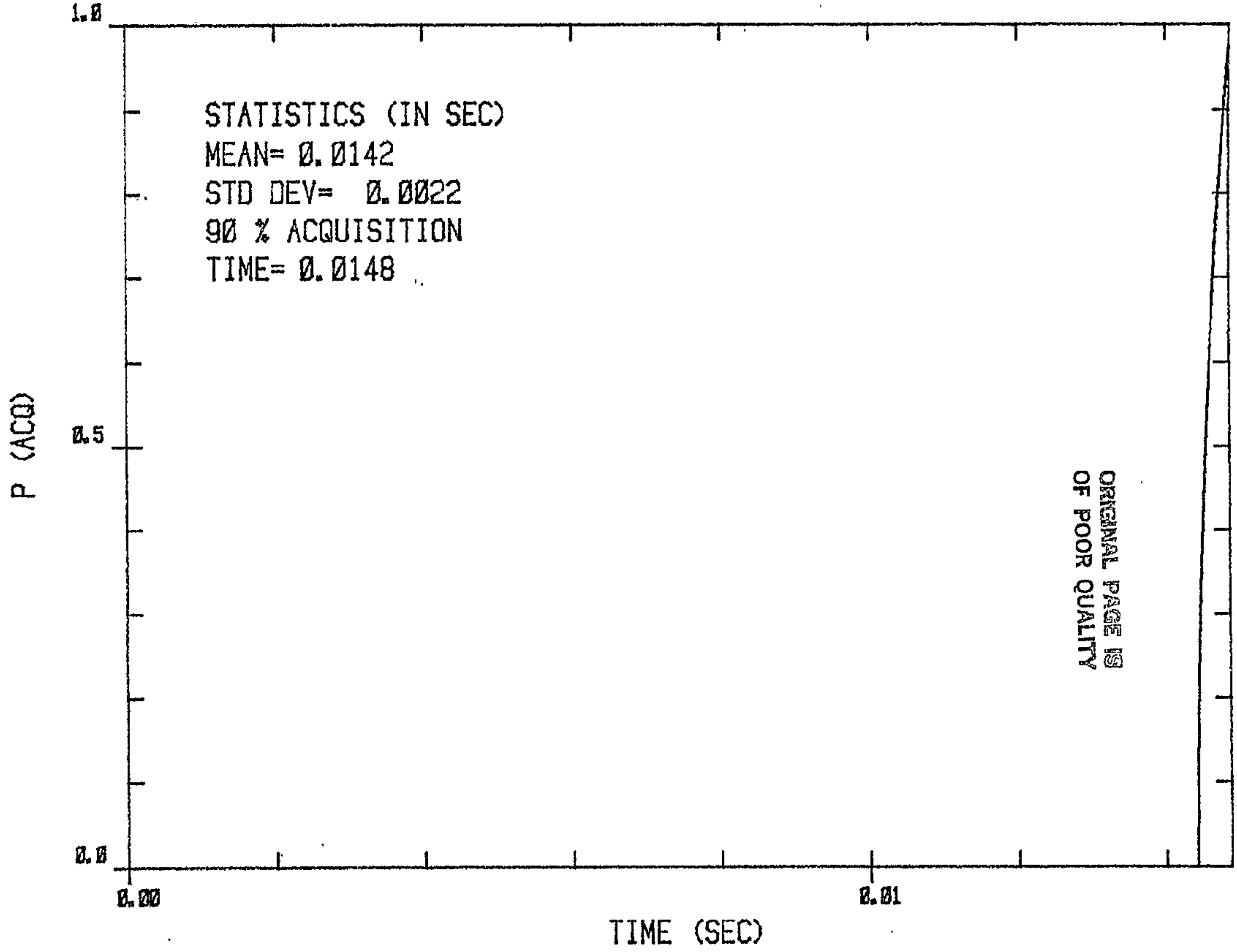

Figure 10. Acquisition Time Cumulative Pdf for Shuttle S-Band Return Link Mode 1 with C/N_0 = 57 dB-Hz.

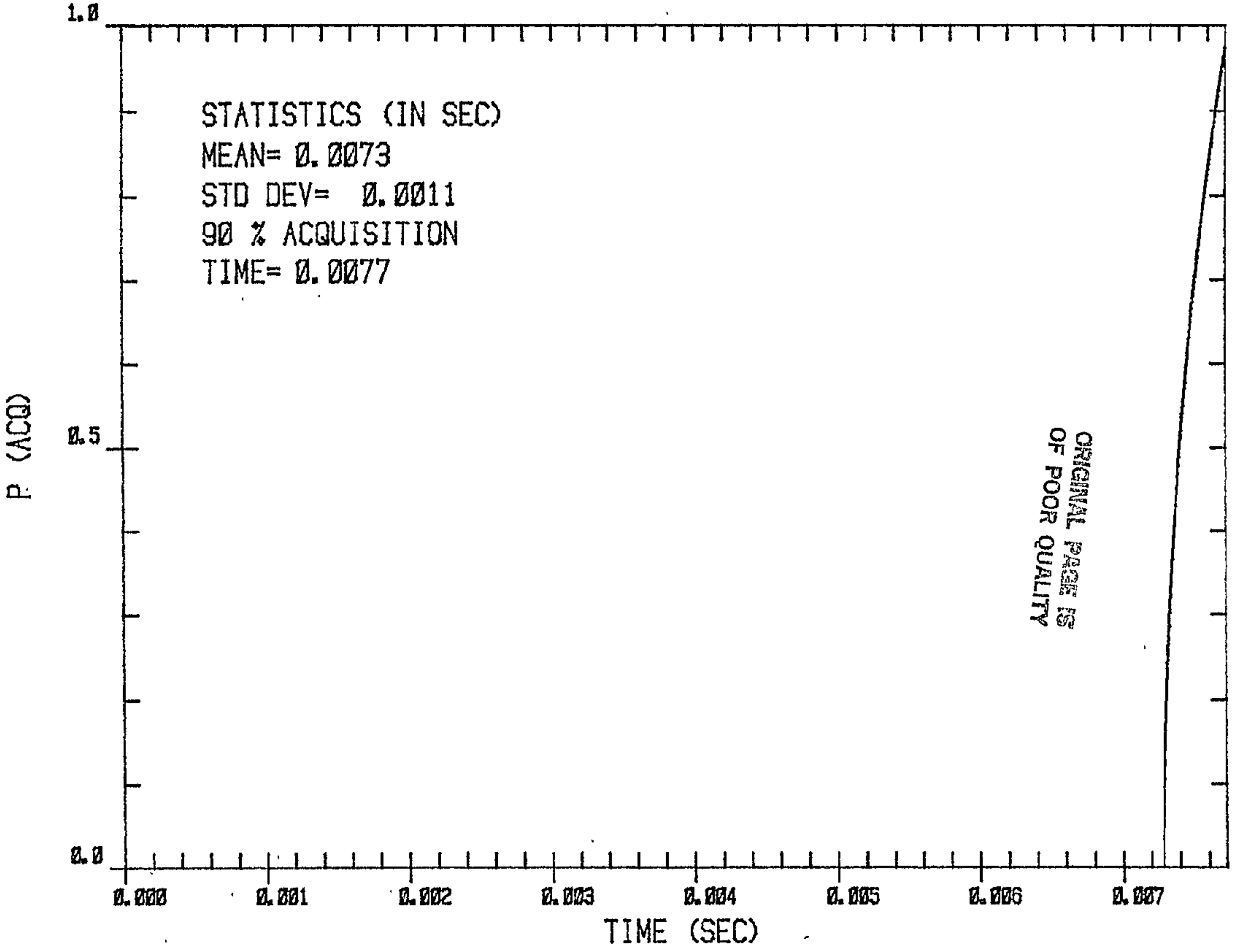

Figure 11. Acquisition Time Cumulative Pdf for Shuttle S-Band Return Link Mode 2 with C/N_0 = 60 dB-Hz.

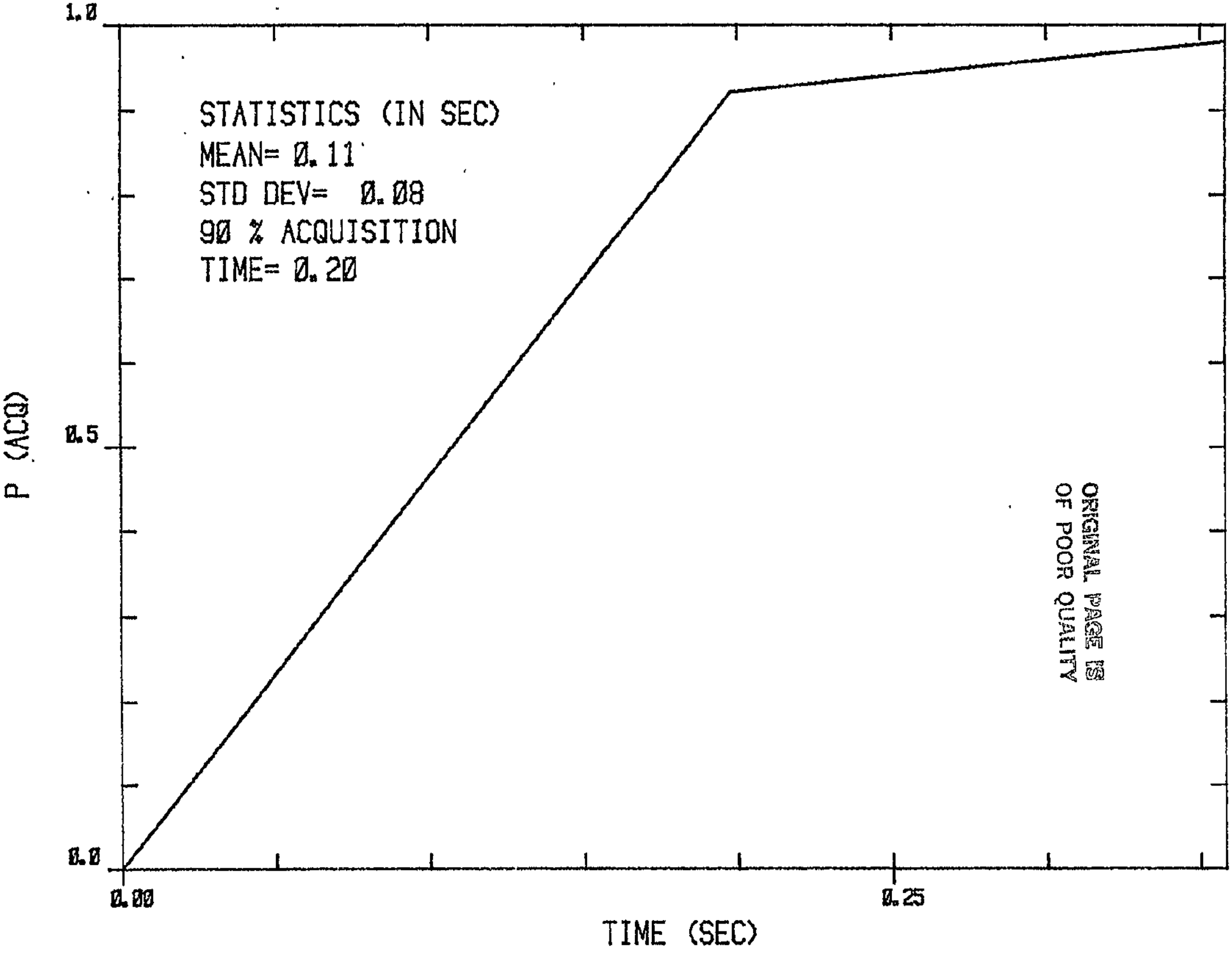

Figure 12. Acquisition Time Cumulative Pdf for Shuttle S-Band Return Link Mode 2 with C/N_0 = 41 dB-Hz.

Table 1. Acquisition Time Specification for Forward Link.

CARRIER ACQUISITION:

ACQUISITION PROBABILITY > 0.9 IN 6 SECONDS

PN ACQUISITON:

P_r/N_0 (dB-Hz)	AVERAGE ACQUISITION TIME (SEC)		AVERAGE TIME TO UNLOCK (SEC)
	96 Ksps	216 Ksps	
49.5	≤ 60	N/A	≥ 3600
51	≤ 20		≥ 3600
53		≤ 30	≥ 3600
54	≤ 10	≤ 10	≥ 3600

REFERENCES

[1] W. H. Alem et al., "Spread Spectrum Acquisition and Tracking Performance for Shuttle Communication Links," IEEE Trans. on Comm., Vol. COM-26, Nov. 1978.

[2] "S-band Shuttle Demodulator/Bit Synchronizer," Motorola Government Electronics Division, Scottsdale, Arizona, June 1978.

[3] R. K. Bacinoki, and R. J. Hegelson, "Orbiter S-band Communications Subsystems," IEEE Trans. on Comm., Vol. COM-26, Nov. 1978.

[4 J. K. Holmes, and C. C. Chen, "Acquisition Time Performance of PN Spread Spectrum Systems," IEEE Trans. on Comm., Vol. COM-25, August 1977.

[5] A. J. Viterbi, Principles of Coherent Communications, McGraw-Hill, New York, 1966, CHapter 3.

[6] J. P. Frazier and J. Page, "Phase-lock Loop Frequency Acquisition Study," IRE Trans., SET-8, pp. 210-227, Sept. 1962.

[7] F. M. Gardner, Phaselock Techniques, Wiley, New York, 1979.

[8] A. Blanchard, Phase-Locked Loops, Wiley, New York, 1976.

[9] D. M. DiCarlo and C. L. Weber, "Statistical Performance of Single Dwell Serial Synchronization Systems," IEEE Trans. on Comm., Vol. COM-28, August 1980.

[10] W. R. Braun, "Performance Analysis for the Expanding Search PN Acquisition Algorithm," IEEE Trans. on Comm., Vol. COM-30, March 1982.

[11] W. C. Lindsey, Synchronization Systems in Communication and Control, Prentice-Hall, Inc., New Jersey, 1972.

6. LINCSIM UPGRADING AND MAINTENANCE

6.1 INTRODUCTION

This chapter reports on some of the work undertaken for Task 6, which requires the continued refinement of the analytical simulation model which is LinCsim. The two remaining sections of this chapter present the models for the effect of two previously unmodeled user constraint parameters on BER, spurious phase modulation (Section 6.2) and incidental amplitude modulation (Section 6.3).

6.2 EFFECT OF SPURIOUS PHASE MODULATION ON BER

In this section we present our model for the effect of spurious carrier phase modulation (PM) on bit error rate (BER).

Consider a carrier sin $(\omega_0 t+\phi(t))$ where the undesirable phase variation is given by

$\phi(t)$ = PM spurs $(Y(t))$+ phase noise $(\theta(t))$

$Y(t)$ is discrete phase modulated components on the carrier

$\Theta(t)$ is random phase modulation.

We first obtain the probability density function (pdf) of $\phi(t)$ and then show how the pdf is applied to the computation of bit error rate.

Each PM can be written as $B_i \sin(\omega_i t+\psi_i)$ for some ω_i and ψ_i. The resulting rms spurious PM will be

$$B \triangleq \sqrt{\sum_{i=1}^{N} B_i^2/2}$$

now, for the worst case, take N=1. Thus

$$B_1 = \sqrt{2B}$$

were B is given. ω_1 is within the specified frequency range, say (a,b). Usually the range is out of the bandwidth of the carrier loop. Assume ω_1 is a random variable uniformly distributed over (a,b). Let $x = \omega_1 t$. Then x is also a random variable uniformly distributed over $(-\pi,\pi)$. Thus,

$$Y = B_1 \sin\omega_1 t$$

Then the pdf of Y is

$$P_Y(y) = \frac{1/B_1}{\pi\sqrt{1-(\frac{y}{B_1})^2}} \qquad , |y| < B$$

and its characteristic function is

$$E(e^{j\lambda Y}) = \frac{1}{\pi}\int_{-B_1}^{B_1} \frac{e^{j\lambda y}\,\frac{1}{B_1}}{\sqrt{1-(\frac{y}{B_1})^2}}\,dy = \frac{1}{2\pi}\int_{-\pi}^{\pi} e^{j\lambda B\cdot\sin x}\,dx = J_0(\lambda B_1)$$

Now, for the second term of the undesirable phase variation, since we assume $\theta(t) \sim N(0,\sigma^2)$, its corresponding characteristic function is

$$E(e^{j\lambda\theta}) = e^{-\frac{\sigma^2\lambda^2}{2}}$$

Now, the characteristic function of the total undesirable phase variation $\phi(t)$ is

$$E(e^{j\lambda\phi}) = J_0(\lambda B_1)\, e^{-\frac{\sigma^2\lambda^2}{2}}$$

The pdf $P(\phi)$ of ϕ is the inverse transform of its characteristic function (p. 100 of "Detection of Signal in Noise" by Whalen)

$$P(\phi) = \frac{1}{\sqrt{2\pi\sigma^2}} \sum_{K=0}^{\infty} \frac{(-\phi^2/2\sigma^2)^K}{k!}\, {}_1F_1(K+\tfrac{1}{2};1;\,-B_1^2/2\sigma^2)$$

where ${}_1F_1(a,b,x)$ is the confluent hypergeometric function defined by

$${}_1F_1\,(a,b,x) = 1+\frac{a}{b}\,\frac{x}{1}+\frac{a(a+1)}{b(b+1)}\,\frac{x^2}{2!}+\frac{a(a+1)\,(a+2)}{b(b+1)\,(b+2)}\,\frac{x^3}{3!}+\cdots$$

We apply this density to the computation of the bit error rate P_e by the following relation:

$$P_e = \int_{-\infty}^{\infty} P(\text{error}|\phi)P(\phi)d\phi$$

Since this density function is not a closed form, only approximation can be done. The number of terms taken is dependent on $\alpha \triangleq \frac{B_1^2}{2\sigma^2}$. The less $B_1^2/2\sigma^2$ is, the faster it converges. Fig. 1 shows the density function $P(x)$, where $x = \frac{\phi}{B_1}$, with α being a parameter. One can see that as α, i.e. as the magnitude of the spur relative to the magnitude of the phase noise, is getting bigger, the departure from Gaussian is more evident. In fact, as $\alpha \to \infty$, $P(x) \to \frac{1}{\pi\sqrt{1-x^2}}$, which is singular at ±1. There being singular points and an infinite power series type function, we have some computational restrictions on a digital computer for large α. In order to overcome this problem, as α is bigger than a certain number, which is set to 10, we use an analytical equation instead of the approximation. Fig. 2 shows there is no essential difference between good approximated values and theoretical values. The disagreement part accounts for the insufficient approximation for large values of ϕ. Fig. 1 also shows that as $\alpha \to 0$, $p(x)$ approaches Gaussian. Hence in order to save computation time, the Gaussian model will replace approximation approach as α is less than .01. Thus the equations to compute the bit error rate can be summarized as follows:

For $\alpha > 10$,

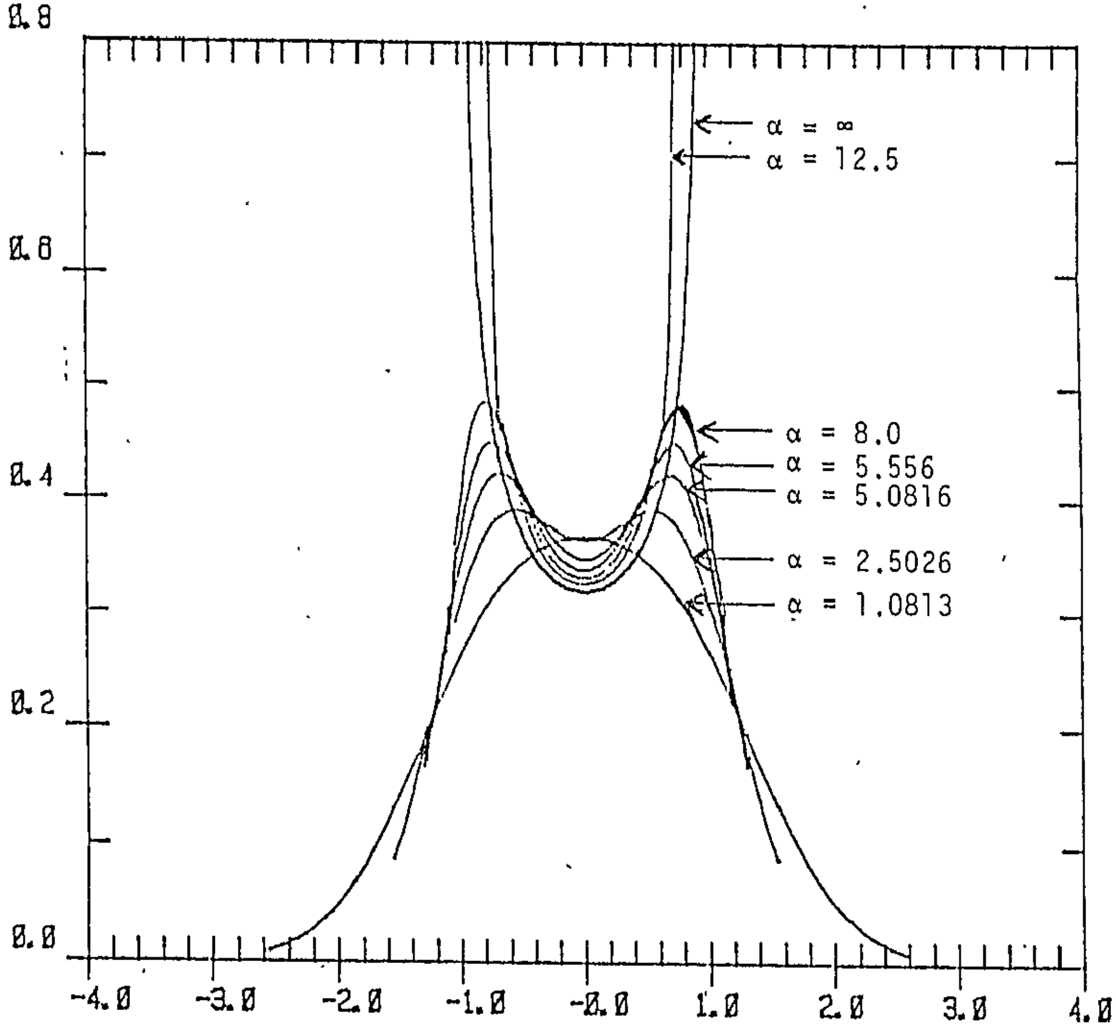

Fig. 1. Density function of ϕ, normalized by B_1.

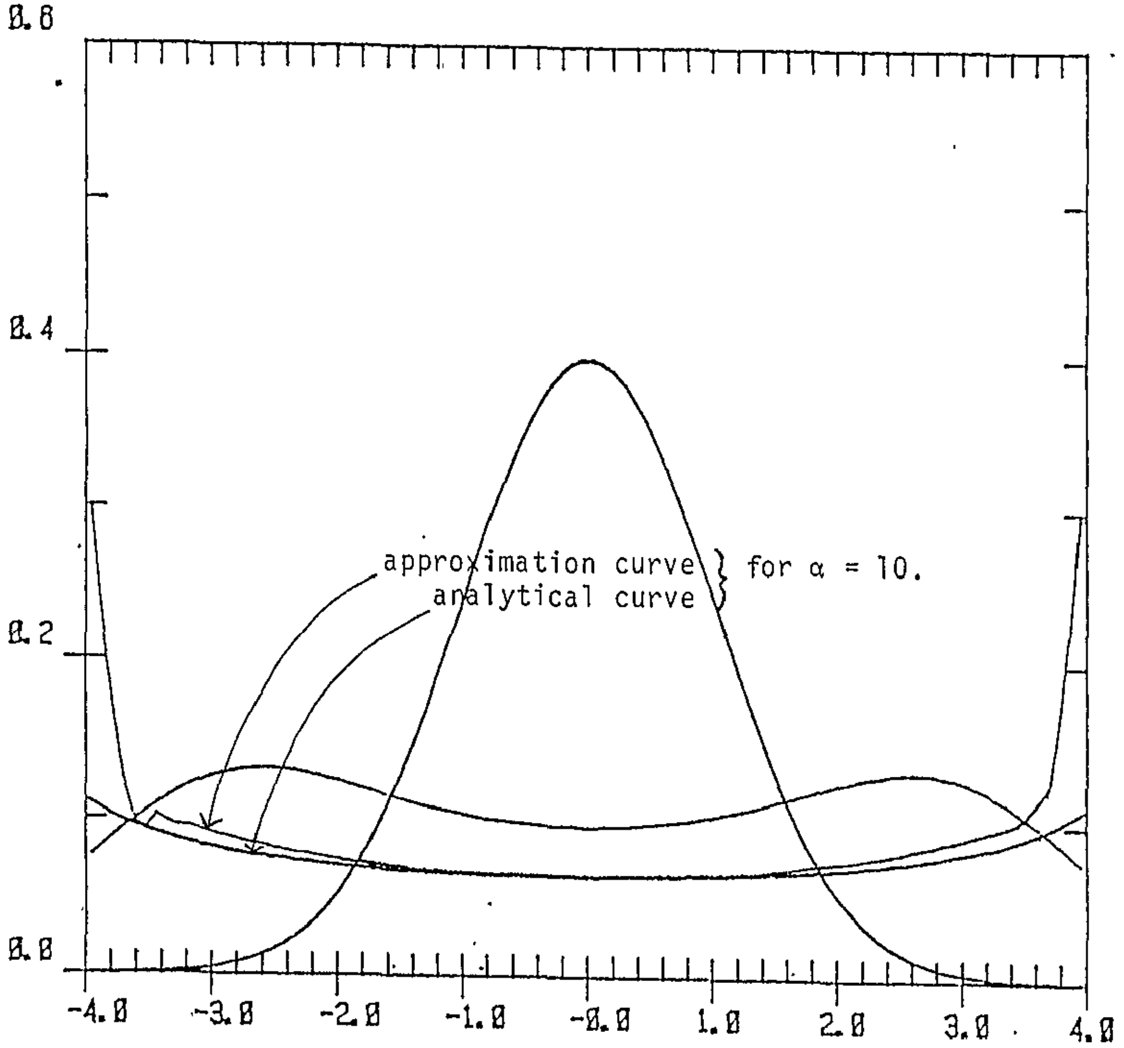

Fig. 2. Comparison of approximation curve and analytic curve for $\alpha = 10$.

Abscissa is normalized by σ.

$$P_e = \int_{-\infty}^{\infty} P_e(\text{error}|\phi)P(\phi)d\phi = \int_{-B_1}^{B} P_e(\text{error}|\phi)P(\phi)d\phi$$

$$= B_1 \int_{-1}^{1} P_e(\text{error}|B_1\theta)P(B_1\theta)d\theta$$

$$\approx B_1 \sum_{i=1}^{N} W_i \, P_e(\text{error}|B_1\theta_i)P(B_1\theta_i)$$

where $\theta = \phi/B_1$

For $.01<\alpha<10$,

$$P_e = \int_{-\infty}^{\infty} P_e(\text{error}|\phi)P(\phi)d\phi = \int_{-\infty}^{\infty} P_e(\text{error}|\phi)P(\phi)\,\frac{e^{-\phi^2/2\sigma^2}}{e^{-\phi^2/2\sigma^2}}d\phi$$

$$= \sqrt{2}\sigma \int_{\infty}^{\infty} P_e(\text{error}|\sqrt{2}\sigma\theta)\,\frac{P(\sqrt{2}\sigma\theta)}{e^{-\theta^2}}\,e^{-\theta^2}d\theta$$

$$\approx \sqrt{2}\sigma \sum_{i=1}^{N} W_i \left[\frac{P(\sqrt{2}\sigma\theta_i)}{e^{-\theta_i^2}}\right] P_e(\text{error}|\sqrt{2}\sigma\theta_i)$$

where $\theta = \dfrac{\phi}{\sqrt{2}.\sigma}$

for $\alpha <.01$.

P_e is computed through the original formulation, which is through Gaussian assumption or Tikhonov density assumption.

Fig 3 shows the density function again with σ being a parameter. The abscissa is $\frac{\phi}{\sigma}$. Where ϕ is total phase error (i.e. PM spur + phase noise) and σ is the standard deviation of phase noise.

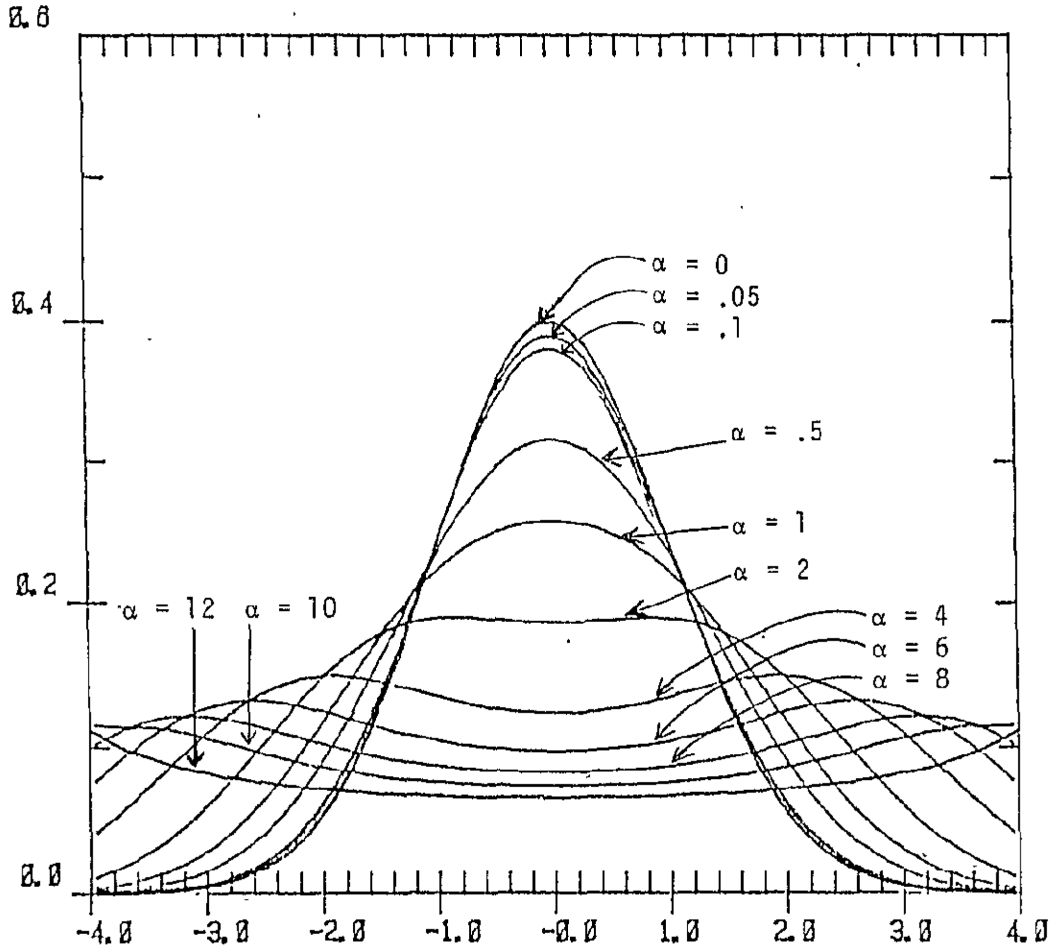

Fig. 3. Density function of ϕ, normalized by σ.

6.3 EFFECT OF INCIDENTAL AMPLITUDE MODULATION ON BER

In this section we present our model for the effect of incidental amplitude modulation (AM) on BER.

The incidental AM is represented by the second term in the following factor to be applied to signal voltage:

$$AM = \left[1 + \sum_{i=1}^{N} M_i \sin(W_i t + \phi_i)\right]$$

The worst case occurs when N=1 and the frequency $\omega_1/2\pi$ is less than the symbol rate and greater than the speed of the receiver AGC. We model the incidental AM as having a period equal to the period of the data stream simulated in LinCsim.

ATTACHMENT 1

LinCom Corporation

INTEROFFICE MEMORANDUM
TM-0682-1080
Date: June 10, 1982

From: W. R. Braun

To: Jack Johnson

Subject: False Lock Problem of Shuttle Payload Signal Processor
cc: B. Batson, S. Novosad, J. Seyl, W. Teasdale

SUMMARY

This memo summarizes LinCom's understanding of the PSP false lock problem based on the meeting at TRW on June 4, 1982 and follow-up discussions. Also included are some preliminary conclusions about the source of the problem and potential solutions.

1. Brief Summary of the Problem

(1) The PSP bit synchronizer uses a first-order loop configuration for acquisition and then switches over to a second-order loop (bit rate tracking).

(2) In its acquisition configuration, the synchronizer tested at ESTL always locked to the correct signal phase.

(3) Removal of the data transitions or the carrier failed to register as a loss of clock sync in the equipment tested at ESTL.

(4) Reapplying the signal or data resulted in a phase lock at either the correct phase or one of three false-lock points.

(5) The equipment under test at TRW showed a different false-lock mode: lock approximately 180 deg out of phase with considerable jitter and no clock sync indication (i.e. supposedly in its first order loop configuration).

2. Discussion

There are three separate problems observed in the equipment of ESTL and TRW.

(1) Lock detector in ESTL equipment is inoperative after initial lock-up.

(2) ESTL equipment has three false-lock phases in second-order (tracking) mode.

(3) TRW equipment has one false-lock phase in first-order (acquisition) mode.

These three observed problems will be discussed in detail below.

2.1 Inoperative Lock Detector

The lock detector is supposed to compare the outputs of two integrators with each other. When locked, these integrators integrate over the center of the symbol and over the transition between symbols, respectively. Supposedly, a loss of lock is declared when the midbit integrator measures less than 6.5 times the value recorded by the transition integrator. Mr. Brett Parrish of NASA/JSC pointed out, however, that the transition integrator has a five times greater gain than the midbit integrator. In the absence of a signal the inputs of both integrators are statistically the same, hence the output of the transition integrator should be five times larger than the midbit integrator output and loss of lock should be declared. The fact that this does not happen suggests that the lock detection algorithm does not operate as described or is not executed at all after lockup (software problem).

2.2 False Lock Phases

Due to an earlier hardware modification, the signal into the PSP is too strong for the A/D converter and the digital integrators. This results in a dead-zone in the bit synchronizer S-curve which seems to be the cause of two of the three false lock points. In other words, a reduction of the input signal strength may result in only one false lock point approximately 180 deg away from the correct lock point. An action item to correct this hardware problem was taken by TRW at the meeting.

The last false lock point is harder to trace to its source. The limited data available to LinCom do not permit a thorough analysis of this problem. However, this problem may not really have to be resolved since a correctly working lock detector will prevent false-lock altogether.

2.3 Problem with TRW Test Setup

The fact that the PSP tested at TRW shows a different type of false lock is quite disturbing. However, the test setup at ESTL and TRW are different, with the one at ESTL simulating the the operational environment more closely. The test equipment itself or a spurious signal may be responsible for the observed behavior. Retesting TRW's PSP at ESTL could give some insight into the source of this problem.

3. Conclusions

(1) An error in the lock detetection algorithm is the most likely source of the faulty lock indication after removal of the signal. Correction of this problem should also remove the false lock problem.

(2) Reduction of the signal strength into the PSP will remove the dead-zone from the Synchronizer S-curve which will result in improved tracking.

(3) The PSP presently at TRW should be retested at ESTL to ensure that it cannot false-lock in the acquisition mode.

ATTACHMENT 2

LinCom Corporation

INTEROFFICE MEMORANDUM

Date: October 14, 1982

From: Teresa McKenzie
Walter Braun

To: Distribution

Subject: Measuring and Reducing RFI Effect on Shuttle and User Spacecraft Dynamics Allowed by Wide Dynamics Demodulator

---

This memo is in response to some of your questions of October 6, 1982. The first topic addressed is the need for measurement data of the RFI effect. The second topic is ways to possibly mitigate the RFI effect. The third topic is the user spacecraft dynamics allowed by the Wide Dynamics Demodulator.

I. Need of Measurement Data of RFI Effect

The first topic discussed relative to the RFI problem was the need for measurement data of the RFI effect to be obtained from Shuttle flights. Measurement data of the RFI effect on a simulated general TDRSS user transponder located in Spain will be taken next year by GSFC. It might be worthwhile for the Shuttle project to coordinate testing with this effort.

II. Mitigating the RFI Effect

The second topic discussed relative to the RFI problem was what could be done in the Shuttle or the ground station to mitigate the RFI effect. Several possibilites were raised.

(1) The first was the inclusion of an interleaver after the convolutional encoder in the Shuttle and a de-interleaver before the Viterbi decoder in the ground station. In a telephone conversation, Aaron Weinberg of

Stanford Telecommunications, Inc., in McLean, Virginia, said that his preliminary results using a Viterbi decoder hardware simulator indicate that for a fairly benign RFI environment, a rate-1/2 code, and ratio of RFI pulse duration to symbol duration as would be obtained with Shuttle mode 1, the lack of an interleaver causes a small increase in EIRP degradation. Similarly, from "RFI Test Study Final Report" dated April 29, 1982, by Harris Corporation, Government Systems Group Communication Systems, it can be seen that for a rate-1/2 code and a ratio of RFI pulse duration to symbol duration equal to that obtained with the longest RFI pulse tested by ESTL and with Shuttle mode 1 symbol rate, degradations of .95 and 4.5 dB with interleaving correspond to about 1.35 and 6 dB without interleaving. For Shuttle mode 2 interleaving is more important, since the Harris results indicate that for the higher data rate, in medium and severe RFI lack of interleaving roughly doubles the number of dB's of degradation. It is expected that for rate-1/3 coding the degradation with interleaving would be less than that for rate-1/2 coding and the effect of no interleaving would not be as bad.

(2) The second possibility raised was to modify the ground station equipment. We do not feel that we know enough about the present equipment to recommend any change. We can only point out one area that could affect performance with RFI while working properly without RFI, and about which we don't know enough to rule it out as a problem source. We suspect that there is a problem in the ground station equipment because our prediction of error rate at the demodulator output with RFI is comfortably pessimistic at low error rates but is quite optimistic at the high error rate of interest. The area of concern is the AGC. Perhaps it is too fast

and reacts to individual RFI pulses or small clusters of pulses.

It needs to be pointed out that if more tests are planned with the RFI test generator, it would be more meaningful to look at the error rate at demodulator output that corresponds to 10^{-4} at the decryptor output, namely about 10^{-1}, rather than at an error rate of 10^{-4}.

(3) The third possibility to minimize the RFI effect was to use both SSA antennas on the TDR satellite. This improves the SNR by a theoretical 3 dB minus about .5 dB loss but also increases the RFI-to-noise ratio by 3 dB, to be pessimistic. From results shown in "TDRSS RFI Test Summary," EE7-82-301, ESTL, May 1982, this would not help in the case of the most severe RFI environment and would help a little in the case of the more benign environments.

(4) The fourth possibility was to optimize TDRS antenna off-pointing. Robert Godfrey of GSFC said that if the Shuttle is shifted out of the center of the main lobe, the power received from Shuttle will decrease more than the RFI power will, so this option is not acceptable.

(5) The fifth possibility was not to encrypt the data. From results in the "TDRSS RFI Test Summary," it can be seen that for the most severe environment one-third of the dB's of EIRP degradation would be saved, while for the more benign environments a smaller proportion would be saved.

(6) A sixth possibility is to use only the higher transmit frequency, thus avoiding the worse of the two environments observed by the TDRS east satellite. Then the EIRP degradation due to RFI is within margin (with rain) for mode 1 and about 4.5 dB over margin for mode 2.

III. User Dynamics Allowed by Wide Dynamics Demodulater

In response to your question about the dynamics allowed by the Wide

Dynamics Demodulator (WDD), maximum values of line-of-sight speed, acceleration, and jerk are given below. They are calculated using an SSA frequency of 2287.5 MHz from "Prime Item Product Function Specification for TDRSS SSAR Wide Dynamics Demodulator," Revised 20 May 1982, Contract No. 76170, Harris Corp. Government Systems Group. The first set of numbers is for tracking a powered user spacecraft. The second set is for reacquisition, which can be accomplished for a powered user spacecraft only if the link is Doppler compensated.

Maximum User Dynamics for Tracking

Mode	Maximum LOS Speed (m/sec)	Maximum LOS Accel. (m/sec^2)	Maximum LOS Jerk (m/sec^3)
Coherent (Modes 1 & 3)	1350	86	4.0
Noncoherent (Mode 2B)	1150	42	2.2

Maximum User Dynamics for Re-Acquisition

Mode	Maximum LOS Speed (m/sec)	Maximum LOS Accel. (m/sec^2)	Maximum LOS Jerk (m/sec^3)
Coherent (Modes 1 & 3)	787	9.2	.41
Noncoherent (Mode 2B)	787	4.6	.20

J. Johnson
S. Novosad
B. Teasdale
B. Batson
J. McLeod
J. Seyl

ATTACHMENT 3

LinCom Corporation

INTEROFFICE MEMORANDUM
TM-0382-1080
Date: March 30, 1982
From: W. R. Braun, T. M. McKenzie

To: Bill Teasdale

Subject: RFI Performance Predictions for Shuttle S-Band Return Link
cc: S. Novosad, J. Seyl, M. Kapell, B. Smith, J. Johnson, R. Godfrey (NASA/Goddard)

The attached table summarizes the LinCsim predictions for the RFI degradations on the Shuttle S-band return link, Modes 1 and 2. The link conditions assumed are summarized below.

- RFI environments as characterized in [1].
- Equivalent thermal noise EIRP 29 dBW in 20 MHz [2].
- RFI pulse duration 5 μsec.
- Baseline SNR (no RFI, BER = 10^{-4}) in 17.5 MHz [3,4]

  Mode 1: -16.16 dB

  Mode 2: -12.87 dB
- Biphase symbols, rate 1/3 convolutional code.
- Nonlinearity consisting of clipper followed by TWT

  Clipper characteristics:

  - 1 dB compression point 6 dB above operating point
  - output power 3 dB below saturation at 1 dB compression point
  - AM/PM distortion 1.2 deg/dB for inputs > 1 dB compression point -.3 dB

  TWT characteristics:

  - 18.5 dB input backoff
  - maximum AM/PM distortion 5.5 deg/dB

Table 1. Predicted CNR Degradation.

Environment/ Off-Pointing		CNR Degradation (dB) Mode 1	Mode 2
EH	0°	1.73	1.73
	1.5°	.47	.46
	4°	.07	.07
EL	0°	2.84	3.58
	1.5°	1.08	1.35
	4°	.35	.41
WH	0°	.38	.37
	1.5°	.03	.03
	4°	0.	0.
WL	0°	.65	.80
	1.5°	.20	.26
	4°	.05	.05

REFERENCES

[1] W. R. Braun, "Programming of RFI Test Generator for Latest Environments," LinCom Technical Report No. TR-0182-1180, January 4, 1982.

[2] J. J. Schwartz, "Simplified Radio Frequency Interference (RFI) for the TDRSS S-band Return Link Evaluation," Memorandum 801/Requirements and Analysis Manager, Network/TDRS Systems Management Office, November 5, 1981.

[3] "Tracking and Data Relay Satellite System.Telecommunication Performance and Interface Document SE-09 (TPID)," TRW DSSG, Redondo Beach, CA, September 12, 1981.

[4] "Space Shuttle.Communications and Tracking Circuit Margin Data Book," NASA/JSC Document E8-6/81/069, August 1981.